KEES VAN HESPEN

THE BRAIN AT RISK

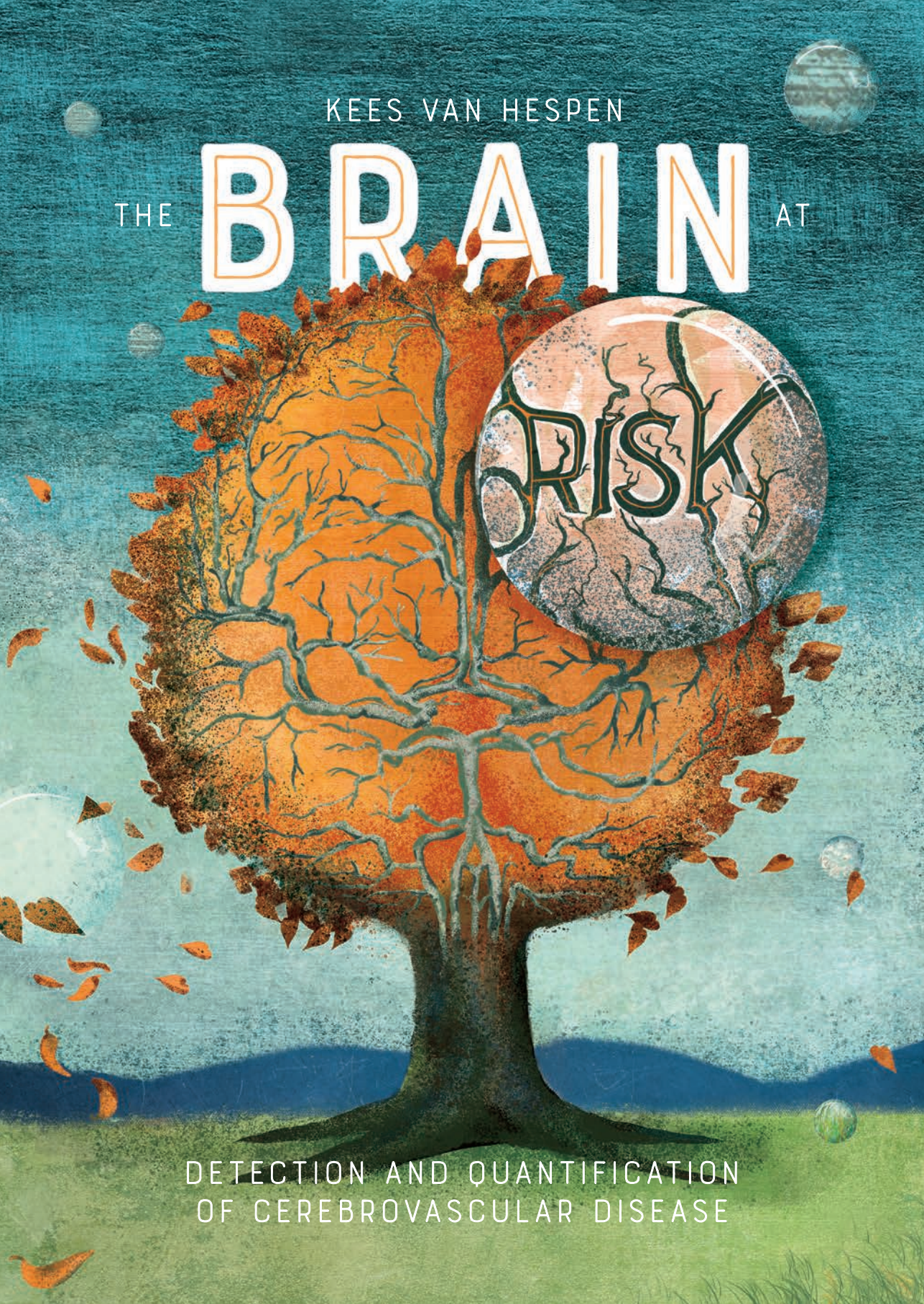

DETECTION AND QUANTIFICATION
OF CEREBROVASCULAR DISEASE

THE BRAIN AT RISK: DETECTION AND QUANTIFICATION OF CEREBROVASCULAR DISEASE

KEES VAN HESPEN

THE BRAIN AT RISK: DETECTION AND QUANTIFICATION OF CEREBROVASCULAR DISEASE

PhD Thesis, Utrecht University, the Netherlands

Cover design	Ilse Schrauwers	isontwerp.nl
Layout	Kees van Hespen
Printed by	Ridderprint	ridderprint.nl
ISBN	978-90-393-7368-2
DOI	10.33540/521

THE BRAIN AT RISK: DETECTION AND QUANTIFICATION OF CEREBROVASCULAR DISEASE

HET KWETSBARE BREIN: DETECTIE EN KWANTIFICATIE VAN CEREBROVASCULAIRE ZIEKTEN

(met een samenvatting in het Nederlands)

PROEFSCHRIFT

ter verkrijging van de graad van doctor aan de Universiteit Utrecht
op gezag van de rector magnificus, prof. dr. H.R.B.M. Kummeling,
ingevolge het besluit van het college voor promoties
in het openbaar te verdedigen
op dinsdag 11 mei 2021 des middags te 2.15 uur

door

KEES MARIJN VAN HESPEN

geboren op 2 februari 1992
te Spijkenisse

Promotoren:	Prof. dr. J. Hendrikse
	Prof. dr. P.R. Luijten
Copromotoren:	Dr. H.J. Kuijf
	Dr. J.J.M. Zwanenburg

The research described in this thesis is part of the NWO-TTW/ Technologiestichting STW and Dutch Heart Foundation partnership program 'Earlier recognition of cardiovascular diseases' (DHF 2015B028).

Financial support by the Dutch Heart Foundation for the publication of this thesis is gratefully acknowledged.

Additional financial support was provided by ChipSoft and Sectra Benelux.

CONTENTS

CHAPTER 1

General introduction

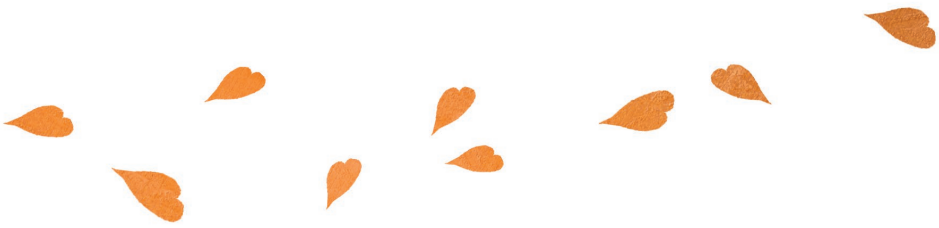

CEREBROVASCULAR DISEASE

One of the most common manifestations of cerebrovascular disease is stroke, in which arteries supplying the brain with oxygenated blood are blocked or ruptured, leading to acute and severe symptoms.[1] Stroke is the second leading cause of death worldwide, with an annual death rate of 5.5 million people.[2] Survivors of stroke are oftentimes confronted with (long-term) disability, and high chance of recurrent strokes.[3] Similarly, patients with extracranial cardiovascular disease also have an elevated risk of strokes.[4] In these groups, early detection of cerebrovascular disease is important to take preventative measures against (recurrent) strokes and to better understand the pathophysiology of disease progression.

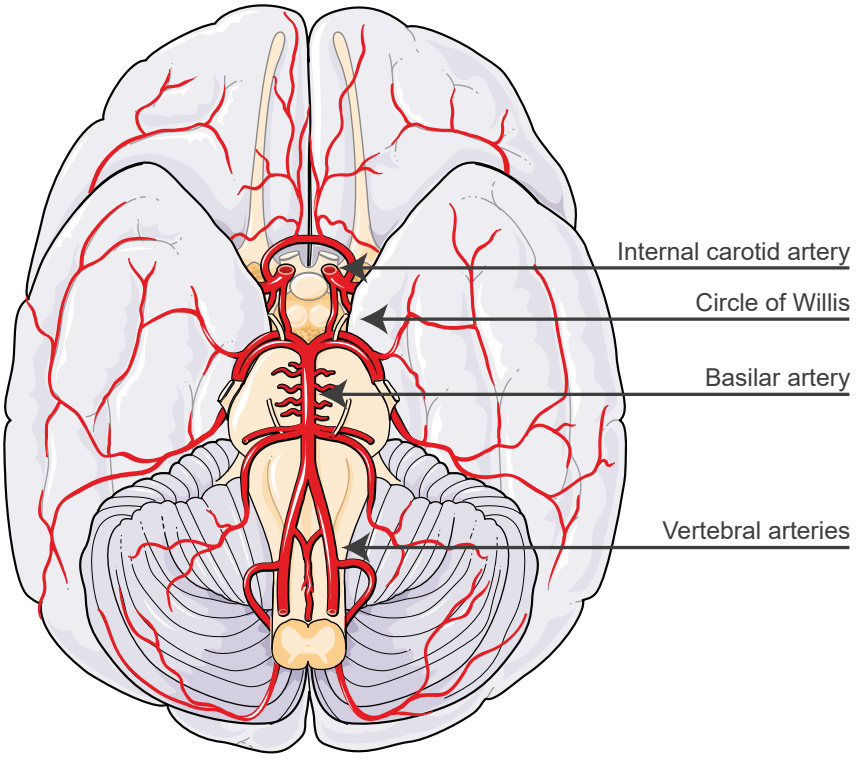

Figure 1. Basal view of the brain and the circle of Willis. The circle of Willis is located around the pons (yellow). Adapted from: "Circle of Willis" by Servier (https://smart.servier.com/smart_image/brain-13/) is licensed under CC BY 3.0 (https://creativecommons.org/licenses/by/3.0/)

Cerebrovascular disease results in morphological and functional changes to the larger (macrovasculature) and smaller (microvasculature) intracranial arteries. The larger intracranial arteries involved in cerebrovascular disease, are the arteries of the circle of Willis (Figure 1). The circle of Willis is a circulatory anastomosis, located at the base of the brain and around the pons. It is connected to the major feeding arteries that supply the brain with oxygenated blood: the internal carotid arteries and the vertebral/basilar arteries.

MACROVASCULATURE: MORPHOLOGICAL CHANGES

These internal carotid arteries and the vertebral/basilar arteries are more predominantly involved in atherosclerosis, compared to other arteries of the circle of Willis.[5] In atherosclerosis, one of the main causes of ischemic stroke,[6] atherosclerotic changes occur in various stages in the vessel wall because of an inflammatory response, resulting in a thickening of the vessel wall (see Figure 2). Eventually, as a result of atherosclerosis, stenotic or occlusive lesions can block the artery. Furthermore, an atherosclerotic plaque can rupture, creating thromboemboli that block more distal arteries.

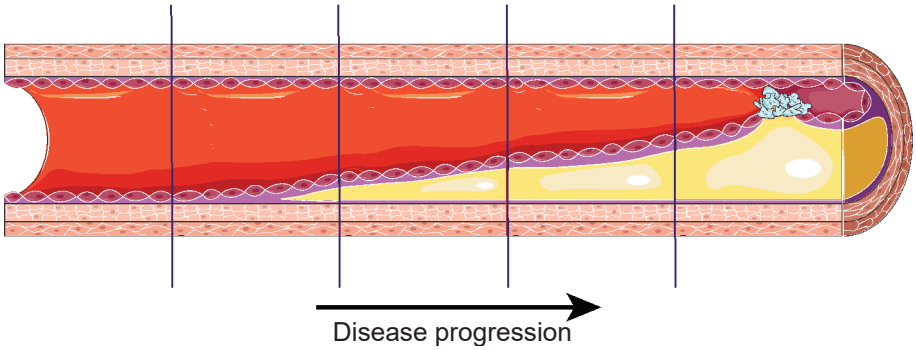

Figure 2. Vessel wall thickening caused by atherosclerotic plaque material buildup in the vessel wall. A normal artery is depicted in the first panel from the left. As atherosclerosis progresses, more and more material builds up in the vessel wall between the intimal and medial layers (second to fourth panel). This built up material can eventually block the artery itself, or rupture, hereby forming a thrombus that blocks an artery further downstream (fifth panel). "From atheroma to thrombus" by Servier (https://smart.servier.com/smart_image/atherosclerosis/) is licensed under CC BY 3.0 (https://creativecommons.org/licenses/by/3.0/)

There are several risk factors involved in stroke of which hypertension is the most important one, next to diabetes, and certain lifestyle choices.[1] Hypertension, which is defined as having an elevated blood pressure over

140/90 mmHg, can also induce morphological changes to the vasculature. Morphological changes caused by hypertension result in, among others, atherosclerotic plaque formation and arterial remodeling.[7–10] In arterial remodeling, a buildup of material and rearrangement of the vessel wall cells occurs to compensate for the increased blood pressure (see Figure 3).[7] The result is an increase in vessel wall thickness, and a (potential) decrease in luminal area, thus causing a stenosis. Stenosis is a poor predictor of early cerebrovascular disease development, because stenosis is only an effect of disease of the vessel wall and remodeling of the arteries can occur without stenosis of the lumen, which is known as positive remodeling or compensatory enlargement.[11,12] Arterial remodeling caused by hypertension in humans has been well described for the extracranial arteries,[13–16] but for the intracranial arteries such comprehensive knowledge is currently lacking.

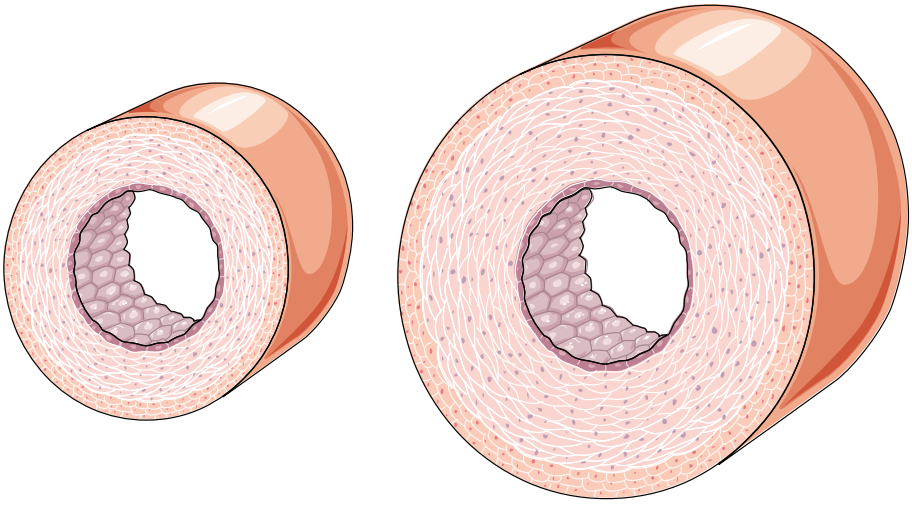

Figure 3. Arterial remodeling with luminal narrowing. On the left, an artery in a normotensive patient. On the right, a hypertensive patient, where a rearrangement of cells results in thickening of the vessel wall. This wall thickening can lead to luminal narrowing, but this is not necessarily present. In outward remodeling, wall thickening occurs, without changes to the vessel lumen. "Arterial hypertrophy" (https://smart.servier.com/smart_image/artery-19/) by Servier is licensed under CC BY 3.0 (https://creativecommons.org/licenses/by/3.0/)

VISUALIZING AND QUANTIFYING MORPHOLOGICAL CHANGES

The intracranial arteries of the circle of Willis are positioned at the base of the brain. Imaging methods such as ultrasound lack the signal-to-noise-ratio to visualize morphological alterations of the intracranial arteries when insonating through the intact skull.[17] Similarly, computed tomography angiography and magnetic resonance (MR) angiography techniques are limited to visualization

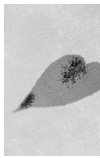

of the lumen of the vessels, whereas vessel wall thickening can occur without a change in luminal diameter.[18,19] In recent years, MR sequences have been developed to visualize the intracranial arteries and the vessel wall itself.[20–22] These image sequences are focused on achieving optimal contrast between the vessel wall and surrounding blood and cerebrospinal fluid, and ideally also between the vessel wall and brain tissue, because the cerebral arteries are oftentimes located close to the brain tissue. Research on quantification and validation of observed vessel wall thickening using these images is limited. In some studies, validation of thickness measurements was possible using ex vivo data, where histological analysis provided reference thickness measurements.[23,24] However, in most clinical studies such validation is not possible.[20,25]

FUNCTIONAL CHANGES

Besides the quantification of biomarkers that are linked to morphological changes of the vessel wall, functional biomarkers can also provide insight in cerebrovascular disease development and progression. Traditionally, such functional biomarkers are measures on changes to the blood flow of the cerebral microvasculature, including perfusion and cerebrovascular reactivity.[26] Nonetheless, quantification of changes in blood flow of the large intracranial arteries are also relevant. For example, blood flow velocity, blood flow rate, and intravascular pressure are prognostic biomarkers of cerebral aneurysm development.[27] Similarly, helicity of secondary flows in the internal carotid has been associated with development of atherosclerosis.[28]

Biomarkers such as arterial distensibility and blood flow pulsatility, that are linked to brain parenchyma damage, including white matter hyperintensities and microbleeds, can also be measured from the blood flow of the large intracranial arteries.[29,30] In a young and healthy population, changes in blood pressure and blood flow velocity (see Figure 4 for an example) over the cardiac cycle can be dampened by flexible and distensible large intracranial arteries, resulting in a steady flow to the small arterioles and capillaries in the brain.[31] In an older group and people with risk factors such as smoking, diabetes, and hypertension, the vessel walls stiffen by deposition of collagen fibers and calcifications.[31,32] In these stiffened arteries, damping of changes in blood pressure and blood flow velocity over the cardiac cycle is less effective. In turn, the resulting pulsatile blood flow may lead to damage to the relatively weak arterioles and capillaries, and thus to brain parenchyma damage.

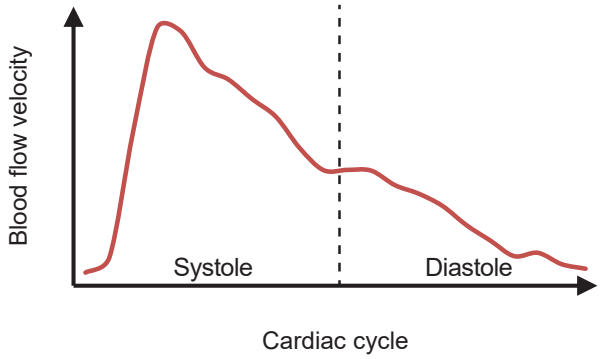

Figure 4. Blood flow velocity as function of the cardiac cycle. At peak systole, the blood flow velocity is maximal, whereas at end-diastole, the blood flow velocity is minimal. When vessel walls stiffen, the blood flow to the arterioles and capillaries become more and more pulsatile.

Phase contrast MR velocity mapping has enabled the visualization of the cerebral blood flow, and allows for in vivo analysis of hemodynamics.[33,34] However, tools that are currently available to perform this in vivo analysis of the intracranial arteries are limited to the analysis of blood flow velocity/pulsatility, and wall shear stress, and are not able to directly measure the arterial distensibility.[35–37] Instead, they assume a static luminal diameter over the cardiac cycle. Quantifying this distensibility can provide insight into the stiffness of the vessel wall, and can likely also be related to cerebrovascular disease development.[38,39]

MICROVASCULATURE: MORPHOLOGICAL CHANGES

Next to cerebrovascular disease of the large intracranial arteries, cerebrovascular disease of the smaller arteries also results in damage to the brain parenchyma, such as white matter hyperintensities, small brain infarcts, lacunes, perivascular spaces, and microbleeds (Figure 5).[1,40] Most of these lesions present without acute symptoms, and can be located all over the brain.

With an annual total of 900.000 MRI scans,[41] of which 25% involve the brain,[42] the work load to analyze these scans on parenchymal damage is high, necessitating automated image analysis. With the quick rise of deep learning methods for image segmentation, classification, and quantification, automated analysis can potentially outperform the radiologist in a lot of tasks.[43] Most supervised methods are trained to extract image features that

are representative of the pathology of interest. These methods rely on large amounts of data to train a model that generalizes well to the problem, which is not available in most cases. Especially when the pathology of interest is heterogeneous in shape, morphology, intensity pattern or location, such methods can fail as they lack enough examples to understand the broad range of visual appearances of the pathology.

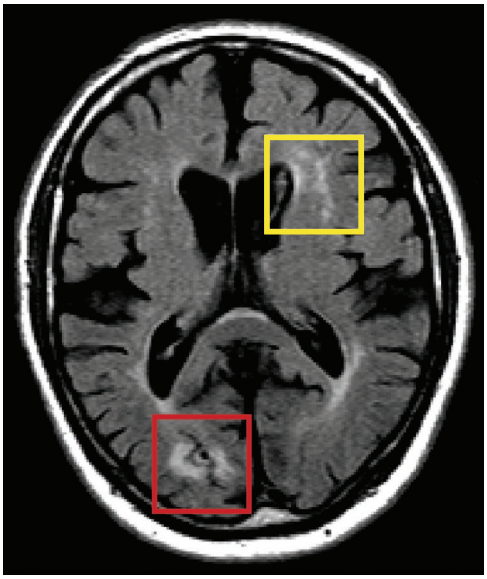

Figure 5. T2-FLAIR transversal MR image of the brain. A white matter hyperintensity can be seen in the yellow box. Within the red box a (small) brain infarct is present.

The damage induced to the brain parenchyma as a result of cerebrovascular disease, including white matter hyperintensities, microbleeds, and small brain infarcts, is heterogeneous in appearance, depending on the used MR sequence. The homogeneous appearance of white matter hyperintensities and microbleeds separately have allowed for dedicated detection/segmentation of these pathologies using deep learning.[44–46] For chronic brain infarcts however, the visual appearance is heterogeneous even between brain infarcts. This limits the implementation and performance of dedicated detection/segmentation methods, like the ones used for white matter hyperintensities and microbleeds.

OUTLINE OF THIS THESIS

The goal of this thesis was to develop quantitative image analysis methods, for the (automated) analysis of brain MR images, in the field of cerebrovascular disease, focusing on vessel walls, blood flow and brain parenchyma.

In **Chapter 2**, an ex vivo study was performed to elucidate the effect of hypertension as risk factor on the arterial remodeling of the nine largest intracranial arteries of the circle of Willis. We used both high-resolution MR image for quantification of arterial remodeling, in conjunction with histopathological analysis to analyze the composition of the arterial walls.

In **Chapter 3**, we explored the limitations of current in vivo vessel wall MR acquisitions, regarding the quantification of vessel wall thickness measurements. Similar to Chapter 2, this study was performed ex vivo as it allowed for validated vessel wall thickness measurements, acquired from high-resolution MR images, against thickness measurements performed on images acquired with an in vivo protocol.

The boundaries of accurate vessel wall thickness measurements unveiled in Chapter 3, were pushed in **Chapter 4**, by applying deep learning technology to improve the accuracy of vessel wall thickness measurements. Hereto we used the same MR image data, as was used in Chapter 2 and 3. As an example, we also evaluated the feasibility of vessel wall thickness measurements on in vivo images of aneurysms of the middle cerebral artery.

In **Chapter 5**, we set out to implement a tool to measure the arterial diameter pulsatility, as measure for the arterial stiffness, and blood flow velocity pulsatility of the larger intracranial arteries. In this study we used both 4D and 2D phase contrast (velocity) MR imaging in volunteers.

We developed an algorithm for the automatic detection of brain pathology in **Chapter 6**, where we evaluated its performance on the detection of chronic brain infarcts.

In **Chapter 7**, the main results of the thesis are summarized and future perspectives are discussed.

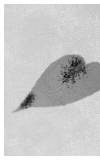

REFERENCES

1. Portegies MLP, Koudstaal PJ, Ikram MA. Cerebrovascular disease. In: Aminoff MJ, Boller F, Swaab DF, eds. Handbook of Clinical Neurology. Vol 138. Amsterdam: Elsevier B.V.; 2016:239-261.

2. Gorelick PB. The global burden of stroke: persistent and disabling. Lancet Neurol. 2019;18:417-418.

3. Burn J, Dennis M, Bamford J, Sandercock P, Wade D, Warlow C. Long-term risk of recurrent stroke after a first-ever stroke. The Oxfordshire Community Stroke Project. Stroke. 1994;25:333-337.

4. Witt BJ, Brown RD, Jacobsen SJ, Weston SA, Yawn BP, Roger VL. A Community-Based Study of Stroke Incidence after Myocardial Infarction. Ann Intern Med. 2005;143:785.

5. Denswil NP, van der Wal AC, Ritz K, et al. Atherosclerosis in the circle of Willis: Spatial differences in composition and in distribution of plaques. Atherosclerosis. 2016;251:78-84.

6. Banerjee C, Chimowitz MI. Stroke Caused by Atherosclerosis of the Major Intracranial Arteries. Circ Res. 2017;120:502-513.

7. Intengan HD, Schiffrin EL. Vascular remodeling in hypertension. Hypertension. 2001;38:581-587.

8. Pires PW, Dams Ramos CM, Matin N, Dorrance AM. The effects of hypertension on the cerebral circulation. Am J Physiol Heart Circ Physiol. 2013;304:H1598-614.

9. Schiffrin EL. Effects of antihypertensive drugs on vascular remodeling: do they predict outcome in response to antihypertensive therapy? Curr Opin Nephrol Hypertens. 2001;10:617-624.

10. Mulvany MJ. Small Artery Remodeling and Significance in the Development of Hypertension. Physiology. 2002;17:105-109.

11. Qiao Y, Anwar Z, Intrapiromkul J, et al. Patterns and Implications of Intracranial Arterial Remodeling in Stroke Patients. Stroke. 2016;47:434-440.

12. Glagov S, Weisenberg E, Zarins CK, Stankunavicius R, Kolettis GJ. Compensatory Enlargement of Human Atherosclerotic Coronary Arteries. N Engl J Med. 1987;316:1371-1375.

13. Litwin M, Niemirska A, Śladowska J, et al. Left ventricular hypertrophy and arterial wall thickening in children with essential hypertension. Pediatr Nephrol. 2006;21:811-819.

14. Park JB, Schiffrin EL. Small artery remodeling is the most prevalent (earliest?) form of target organ damage in mild essential hypertension. J Hypertens. 2001;19:921-930.

15. Suurküla M, Fagerberg B, Wendelhag I, Agewall S, Wikstrand J. Atherosclerotic Disease in the Femoral Artery in Hypertensive Patients at High Cardiovascular Risk. Arterioscler Thromb Vasc Biol. 1996;16:971-977.

16. Chironi G, Gariepy J, Denarie N, et al. Influence of hypertension on early carotid artery remodeling. Arterioscler Thromb Vasc Biol. 2003;23:1460-1464.

17. Hölscher T, Sattin JA, Raman R, et al. Real-Time Cerebral Angiography: Sensitivity of a New Contrast-Specific Ultrasound Technique. Am J Neuroradiol. 2007;28:635-639.

18. van der Kolk AG, Zwanenburg JJM, Brundel M, et al. Intracranial Vessel Wall Imaging at 7.0-T MRI. Stroke. 2011;42:2478-2484.

19. Mandell DM, Mossa-Basha M, Qiao Y, et al. Intracranial vessel wall MRI: Principles and expert consensus recommendations of the American society of neuroradiology. Am J Neuroradiol. 2017;38:218-229.

20. Qiao Y, Steinman DA, Qin Q, et al. Intracranial arterial wall imaging using three-dimensional high isotropic resolution black blood MRI at 3.0 Tesla. J Magn Reson Imaging. 2011;34:22-30.

21. Viessmann O, Li L, Benjamin P, Jezzard P. T2-Weighted intracranial vessel wall imaging at 7 Tesla using a DANTE-prepared variable flip angle turbo spin echo readout (DANTE-SPACE). Magn Reson Med. 2017;77:655-663.

22. Zhang L, Zhang N, Wu J, et al. High resolution three dimensional intracranial arterial wall imaging at 3 T using T1 weighted SPACE. Magn Reson Imaging. 2015;33:1026-1034.

23. Kleinloog R, Korkmaz E, Zwanenburg JJM, et al. Visualization of the aneurysm wall: A 7.0-Tesla magnetic resonance imaging study. Neurosurgery. 2014;75:614-622.

24. Sherif C, Kleinpeter G, Loyoddin M, et al. Aneurysm Wall Thickness Measurements of Experimental Aneurysms: In Vivo High-Field MR Imaging Versus Direct Microscopy. Acta Neurochir Suppl. 2015;120:17-20.

25. Qiao Y, Guallar E, Suri FK, et al. MR Imaging Measures of Intracranial Atherosclerosis in a Population-based Study. Radiology. 2016;280:860-868.

26. Catchlove SJ, Pipingas A, Hughes ME, Macpherson H. Magnetic resonance imaging for assessment of cerebrovascular reactivity and its relationship to cognition: a systematic review. BMC Neurosci. 2018;19:21.

27. MacDonald ME, Dolati P, Mitha AP, Eesa M, Wong JH, Frayne R. Hemodynamic alterations measured with phase-contrast MRI in a giant cerebral aneurysm treated with a flow-diverting stent. Radiol Case Reports. 2015;10:1109.

28. Wang J, Balu N, Canton G, Yuan C. Imaging biomarkers of cardiovascular disease. J Magn Reson Imaging. 2010;32:502-515.

29. Mitchell GF, van Buchem MA, Sigurdsson S, et al. Arterial stiffness, pressure and flow pulsatility and brain structure and function: the Age, Gene/Environment Susceptibility—Reykjavik study. Brain. 2011;134:3398-3407.

30. Zhai F-F, Ye Y-C, Chen S-Y, et al. Arterial Stiffness and Cerebral Small Vessel Disease. Front Neurol. 2018;9:723.

31. van Varik BJ, Rennenberg RJMW, Reutelingsperger CP, Kroon AA, de Leeuw PW, Schurgers LJ. Mechanisms of arterial remodeling: lessons from genetic diseases. Front Genet. 2012;3:290.

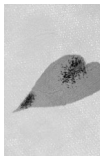

32. Kohn JC, Lampi MC, Reinhart-King CA. Age-related vascular stiffening: causes and consequences. Front Genet. 2015;06:1-17.

33. Wigström L, Sjöqvist L, Wranne B. Temporally resolved 3D phase-contrast imaging. Magn Reson Med. 1996;36:800-803.

34. Markl M, Chan FP, Alley MT, et al. Time-resolved three-dimensional phase-contrast MRI. J Magn Reson Imaging. 2003;17:499-506.

35. Dunås T, Wåhlin A, Zarrinkoob L, Malm J, Eklund A. 4D flow MRI—Automatic assessment of blood flow in cerebral arteries. Biomed Phys Eng Express. 2018;5:015003.

36. Wåhlin A, Ambarki K, Birgander R, et al. Measuring Pulsatile Flow in Cerebral Arteries Using 4D Phase-Contrast MR Imaging. Am J Neuroradiol. 2013;34:1740-1745.

37. Schrauben E, Wåhlin A, Ambarki K, et al. Fast 4D flow MRI intracranial segmentation and quantification in tortuous arteries. J Magn Reson Imaging. 2015;42:1458-1464.

38. Sadekova N, Vallerand D, Guevara E, Lesage F, Girouard H. Carotid calcification in mice: A new model to study the effects of arterial stiffness on the brain. J Am Heart Assoc. 2013;2:1-12.

39. Schnerr RS, Jansen JFAA, Uludag K, et al. Pulsatility of lenticulostriate arteries assessed by 7 Tesla flow MRI-Measurement, reproducibility, and applicability to aging effect. Front Physiol. 2017;8:1-10.

40. Wardlaw JM, Smith EE, Biessels GJ, et al. Neuroimaging standards for research into small vessel disease and its contribution to ageing and neurodegeneration. Lancet Neurol. 2013;12:822-838.

41. Eurostat. Healthcare resource statistics – technical resources and medical technology – Statistics Explained. Available at: https://ec.europa.eu/eurostat/statistics-explained/index.php/Healthcare_resource_statistics_-_technical_resources_and_medical_technology. Accessed October 20, 2020.

42. Smith-Bindman R, Miglioretti DL, Johnson E, et al. Use of Diagnostic Imaging Studies and Associated Radiation Exposure for Patients Enrolled in Large Integrated Health Care Systems, 1996-2010. JAMA. 2012;307:2400-2409.

43. Litjens G, Kooi T, Bejnordi BE, et al. A survey on deep learning in medical image analysis. Med Image Anal. 2017;42:60-88.

44. Morrison MA, Payabvash S, Chen Y, et al. A user-guided tool for semi-automated cerebral microbleed detection and volume segmentation: Evaluating vascular injury and data labelling for machine learning. NeuroImage Clin. 2018;20:498-505.

45. Moeskops P, de Bresser J, Kuijf HJ, et al. Evaluation of a deep learning approach for the segmentation of brain tissues and white matter hyperintensities of presumed vascular origin in MRI. NeuroImage Clin. 2018;17:251-262.

46. Kuijf HJ, Casamitjana A, Collins DL, et al. Standardized Assessment of Automatic Segmentation of White Matter Hyperintensities and Results of the WMH Segmentation Challenge. IEEE Trans Med Imaging. 2019;38:2556-2568.

CHAPTER 2

Arterial remodeling of the intracranial arteries in patients with hypertension and controls

A POST-MORTEM STUDY

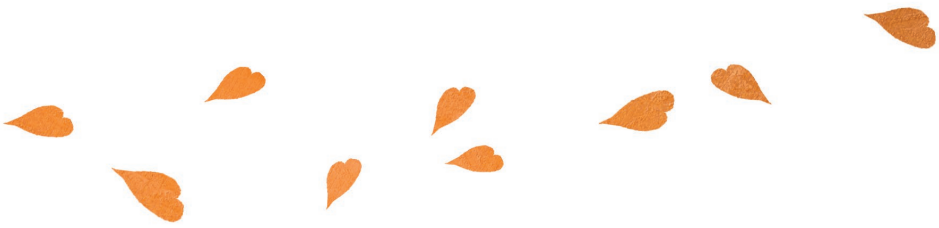

PUBLISHED AS:

HYPERTENSION. 2021;77:135-146.

Kees M. van Hespen, Claire Mackaaij, Ingeborg S.E. Waas, Marloes P. de Bree, Jaco J.M. Zwanenburg, Hugo J. Kuijf, Mat J.A.P. Daemen, Jeroen Hendrikse, Dorien M.A. Hermkens. *Arterial Remodeling of the Intracranial Arteries in Patients With Hypertension and Controls.*

ABSTRACT

PURPOSE

Even though the intracranial arteries play a major role in cerebrovascular disease, arterial remodeling due to hypertension has not been well described in humans. In this study, we aimed to quantify this remodeling for the larger intracranial arteries of the circle of Willis in humans.

MATERIALS AND METHODS

Twenty-four and 25 ex vivo human circle of Willis specimens, selected from individuals with and without a history of hypertension, respectively, were imaged at 7T magnetic resonance imaging (MRI). Subsequently, histological analysis was performed on these specimens.

First, we validated the vessel wall thickness and area measurements from MRI against histology. Second, we investigated potential differences in vessel wall thickness and area between our hypertensive and control groups with both techniques. Third, using histological analysis, we investigated potential differences in arterial wall stiffness, and atherosclerotic plaque severity and load between these groups. All analyses were unadjusted for other factors.

RESULTS

The vessel wall thickness and area measurements were comparable between MRI and histology (mean difference of 0.04 mm (limits of agreement: -0.12–0.19 mm), and 0.43 mm^2 (limits of agreement: -0.97–1.8 mm^2), respectively). We observed no statistically significant differences in vessel wall thickness and area between the hypertensive and control group using either technique. Histological analysis showed early and advanced atherosclerotic plaques for almost all anatomical locations for both groups. The collagen to smooth muscle ratio, as a measure for arterial stiffness, was significantly higher for the internal carotid artery in the hypertensive group.

CONCLUSION

In this study, we have extensively investigated hypertensive arterial remodeling, by morphological measurements and vessel wall composition measurements at multiple vascular locations along the human circle of Willis. Given our vessel wall measurements, our study suggests that the effect of hypertension on arterial remodeling of the larger intracranial arteries is minimal.

INTRODUCTION

Hypertension, defined as a blood pressure above 140 mmHg systolic or 90 mmHg diastolic, is one of the largest risk factors for cardiovascular and cerebrovascular disease.[1,2] Hypertension can induce functional and morphological alterations of the vasculature. Functional alterations of the cerebral vasculature can result in impairment of cerebrovascular autoregulation, endothelial and blood-brain barrier dysfunction, and functional hyperemia.[3] Morphological alterations due to hypertension result in, among others, atherosclerotic plaque formation and arterial remodeling.[4–7] Quantifying these (morphological) alterations in vivo can give an insight in cerebrovascular disease progression and development.

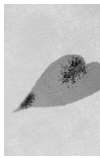

Even though the larger intracranial arteries play a major role in cerebrovascular disease, the effect of arterial remodeling due to hypertension on the major intracranial arteries has mostly been studied in animal models (reviewed in Pires et al.[5]). For example, Izzard et al.[8] observed eutrophic arterial remodeling of the middle cerebral arteries in spontaneous hypertensive rats, compared to a control group without hypertension using histological analysis. Using similar analysis, arterial remodeling was also observed in the posterior cerebral circulation of spontaneous hypertensive rats.[9] For the basilar artery, a histology study on mini-pigs showed an increase in collagen content in the basilar artery of hypertensive animals, which subsequently led to an increased vessel wall thickness.[10]

In humans, research on arterial remodeling of the cerebral vasculature has mostly been done in relation to various other cerebrovascular diseases such as atherosclerosis,[11] vasculitis,[12] and Moyamoya disease,[13–15] whereas the effect of hypertension on arterial remodeling has to our knowledge only been scarcely investigated for the human cerebral vasculature. Only for cerebral arterioles and small resistance arteries such remodeling was observed in hypertensive patients, as compared to normotensive controls, using histological analysis.[16,17] Comprehensive knowledge on arterial remodeling of the larger cerebral arteries in humans due to hypertension is currently lacking.

To comprehensively quantify the effect of hypertension on arterial remodeling, we performed both high-field, high-resolution magnetic resonance imaging (MRI) and histological analysis of post-mortem circle of Willis specimens in patients with and without a history of hypertension. Ex vivo MRI allows for

accurate measurements of the vessel wall, and allows for measurements at multiple locations in the circle of Willis.

The aim of the current study was threefold. First, to validate the relation between MRI vessel wall measurements and histological based vessel wall measurements in an extensive collection of post-mortem samples. Second, to investigate potential differences in vessel wall thickness and area between post-mortem samples from individuals with and without a history of hypertension, for multiple locations in the circle of Willis using both MRI and histological based vessel wall measurements. Third, to investigate differences in the composition of the vessel wall between individuals with and without a history of hypertension using histological analysis. Here, we determined the atherosclerotic plaque load and severity, and we calculated the collagen to smooth muscle ratio as a measure of arterial wall stiffness.

MATERIALS AND METHODS

SPECIMEN DATA

In this retrospective, institutional review board approved study, 49 circle of Willis specimens, stored in buffered formalin (4%), were selected from 136 autopsy cases in the University Medical Center Utrecht performed between 2015 and 2018. In these 136 autopsy cases, brain autopsy was performed for diagnostic purposes and the circle of Willis was stored. Circle of Willis specimens of 24 patients were included in the hypertensive group, who had a reported systolic or diastolic blood pressure above 140 mmHg or 90 mmHg respectively, on at least two separate, consecutive occasions and/or were using antihypertensive drugs, in the last years of their life.[18] Similarly, 25 circle of Willis specimens of patients who were normotensive and were not using antihypertensive medication were included in the control group. Additional inclusion criteria for both groups included the patients age to be over 50 years, and for the circle of Willis to be intact. In each group 15 males and 9 or 10 females were included. The mean age of the controls (mean ± standard deviation: 67.7 ± 9.75 years), was not significantly different from the mean age of the hypertensive group (69.16 ± 8.9 years, $t[47] = -0.544$, $p = 0.59$).

Table 1. Causes of death and their prevalence for hypertensive patients and controls. The 'Other' causes category includes retroperitoneal hemorrhage, and diabetic ketoacidosis for the hypertensive group, and Lewy body dementia for the control group.

		Hypertension	Control
Cardiovascular	Myocardial infarction	5	1
	Cardiomyopathy	0	1
	Heart failure	3	0
	Sinus thrombosis	0	1
	Arrhythmia	1	0
Cerebrovascular	Cerebral emboly	1	0
	Cerebral amyloid angiopathy	0	1
	Brain infarct	4	1
Cancer	Glioblastoma	0	1
	Lymphoma	1	0
	Lung carcinoma	1	1
	Jugular paraganglioma	0	1
	Melanoma	0	1
Trauma		1	2
Respiratory/infectious		4	5
ALS		1	7
Unknown		0	1
Other		2	1
Total		**24**	**25**

The cause of death for both groups is given in Table 1. Leading causes of death for the patients in the hypertensive group include cerebrovascular disease, and cardiovascular disease. The leading cause of death in the control group is amyotrophic lateral sclerosis (ALS). The analyses performed on the circle of Willis specimens were performed similarly regardless of cause of death, age, and sex of the patients.

SPECIMEN PREPARATION

The circle of Willis specimens were embedded in a 2% agarose solution, and positioned according to the anatomic structure. Blood and air were removed from the vessels, according to the method described by van der Kolk et al.[19] Fiducials (cactus spines) were used to mark 21 locations within each specimen

(Figure 1).[20,21] The measurements performed at these locations were averaged per specimen for each of 9 anatomical locations, including the vertebral artery (VA), basilar artery (BA), internal carotid artery (ICA), middle cerebral artery (MCA), anterior cerebral artery (ACA), posterior communicating artery (PCoA), posterior cerebral artery (PCA), superior cerebellar artery (SCA), and anterior inferior cerebellar artery (AICA).

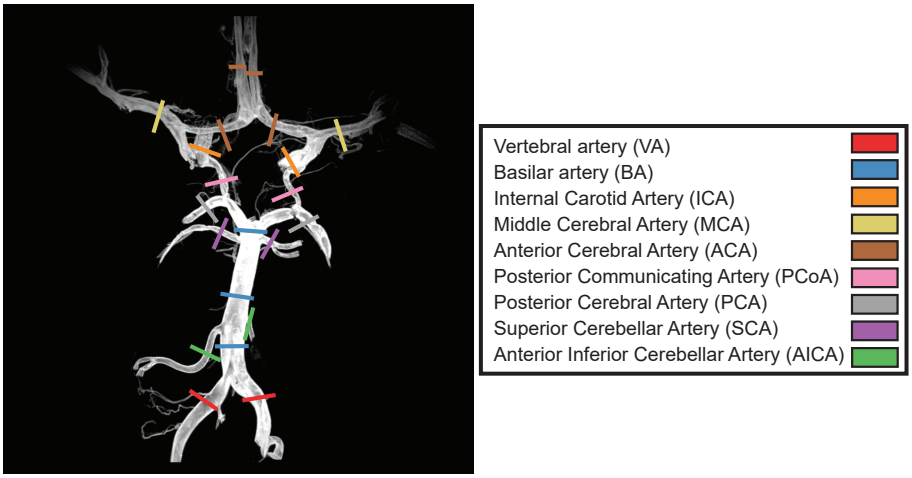

Figure 1. Circle of Willis and the locations where measurements were performed given in color. Measurements were performed at 21 locations in the circle of Willis. Locations with an identical color were grouped under the same anatomical location, as given in the legend. For each anatomical location, the abbreviation is given between brackets.

MRI

MRI of the embedded specimens was performed using a 3D gradient echo sequence (isotropic acquired voxel size: 0.11 mm; repetition time/echo time: 55/6.2 ms; flip angle: 28 degrees; number of signal averages: 1; acquisition time: 5h46m),[20] acquired on a 7T MR scanner (Philips, Best, the Netherlands). A volume transmit coil (Nova Medical, Wilmington, MA, USA) and a custom-made high-density receive coil (16 channels per 70 cm^2, MR Coils, Zaltbommel, the Netherlands) were used.

VESSEL WALL MEASUREMENTS

For each specimen, the vessel wall thickness and area were measured at the locations of the fiducials using a processing pipeline created in MeVisLab 2.8 (Fraunhofer Mevis, Germany[22]). The rater (K.M. van Hespen) was blinded to the hypertensive status. In this processing pipeline, the center line of the lumen was automatically traced from manually selected start- and endpoints,

equating to roughly 1 to 2 mm per measurement location, which was visually inspected on accuracy. A multiplanar reconstruction (MPR) was performed along this center line. Image slices in the MPR stack that did not correctly follow the center line were removed from further analysis.

Next, for each slice in the MPR stack an isocontour was computed at the inner and outer boundary of the vessel wall, at the full-width-at-half-maximum (FWHM) intensity value. Example contours for a single slice are given in Figure 2A and 2B. Subtracting the area of the outer contour from the area of the inner contour yields the vessel wall area (shaded green area). The vessel wall area was averaged over all used slices in the MPR stack.

A nearest neighbor search was employed for all points on the inner contour, to find the distance to the closest point on the outer contour, and vice versa (given by the red lines in Figure 2). The vessel wall thickness was defined as the median contour-contour distance between the inner and outer contours, over all used slices in the MPR stack.

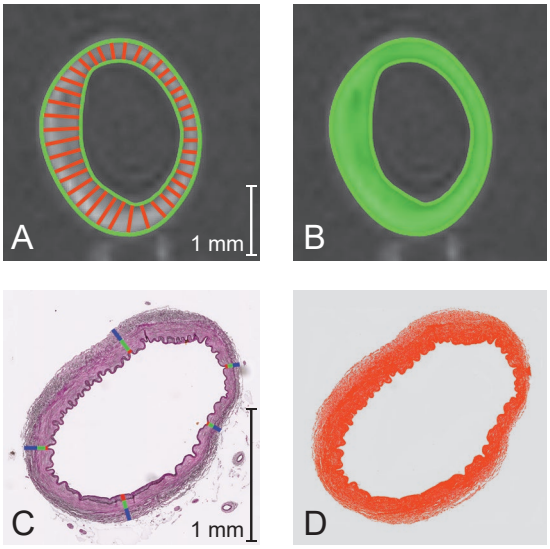

Figure 2. Vessel wall thickness and area measurement method for MR- and histological images. MRI: Automatically drawn isocontours for one slice of an MPR stack given by the green lines. (A) Average vessel wall thickness was measured as the median distance from the inner to outer contour, measured from a large number of positions along the vessel wall, as illustrated by the red lines. (B) The average vessel wall area was calculated as the area enclosed by the outer and inner contour. Histology: (C) Manual measurement of the vessel wall thickness at five equidistant locations along the vessel circumference, given as the sum of the blue (adventitia) - green (media) - red (intima) lines. (D) Automatically measured vessel wall area by thresholding.

HISTOLOGICAL ANALYSIS

After MRI, parts of the circle of Willis, at the locations of the fiducials, were embedded in paraffin and cut into 5 μm sections. The sections were mounted on coated glass slides and dewaxed with xylene and rehydrated through graded ethanol solutions to water. The sections were stained with Elastic von Gieson (EvG) staining for the vessel wall thickness and area measurements, and with hematoxylin-eosin (HE) staining for the plaque classification.

Immunohistochemistry was performed to visualize smooth muscle cells and collagen consecutively. Hereto, endogenous peroxidase was blocked by incubating the slides in 0.3% H_2O_2 in methanol for 20 minutes at room temperature. Antigen retrieval was performed at 98 ˚C for 10 minutes in a Lab Vision PT-module (ThermoFisher, Waltham, MA, USA) with Tris-EDTA (TA-250-PM4x, ThermoFisher; pH = 9). The tissue was incubated with Super Block (ScyTek Laboratories, Logan, UT, USA) for 10 minutes at room temperature. Next, the slides were incubated with Mouse Anti-Human Smooth Muscle Actin (clone 1A4, M085101 Agilent, Santa Clara, CA, USA) for 60 minutes at room temperature, washed in TBS and incubated with BrightVision+ Poly-HRP-Anti Mouse Ig (VWRKS/DPVM-HRP, VWR, Amsterdam, the Netherlands) for 30 minutes at room temperature. After the slides were incubated with VECTOR® NovaRED® Peroxidase (HRP) Substrate Kit (SK-4800, Vector Laboratories, Burlingame, CA, USA), they were covered with Glycerol/glycerin and subsequently with coverslips. Representative images of this first staining were taken with a Philips IntelliSite Ultra-Fast Scanner (Philips, Best, the Netherlands). To remove the first staining, the coverslips were detached and the slides were incubated in stripping buffer (0.06M Tris HCL pH7.5, 2% SDS and 0.17% beta-mercaptoethanol) for 30 minutes on 50°C and then incubated in Picrosirius red solution for 30 minutes at room temperature and differentiated in 0.01 N HCL for 2 minutes.

All slides were dehydrated in ethanol (70%, 96% and 100%) and eventually in xylene and covered with coverslips and Pertex mounting medium (HistoLab 00801-EX). Images were taken with the Philips IntelliSite Ultra-Fast Scanner.

VESSEL WALL MEASUREMENTS

The average vessel wall thickness (sum of intima, media and adventitia) was measured manually using Digipath (DigiPath solutions, LCC, Spring, Texas, USA) from 5 equally distributed positions around the vessel wall (Figure 2C). The total vessel wall area was measured using ImagePro Premier (version 9.3,

Media Cybernetics, Rockville, Maryland, USA), see Figure 2D. Similarly, the area of both smooth muscle cell and collagen staining was measured using ImagePro Premier.

The presence of atherosclerotic plaques was scored according to the American Heart Association classification system[23]: no anomaly (no morphological changes); early plaques, including intimal thickening, fatty streak, and pathological intimal thickening, and advanced plaques, including fibrous plaque, fibrolipid plaque, and calcified plaque. Histological measurements were performed by a different rater than the MRI measurements (D.M.A. Hermkens). Both were blinded to the hypertensive status.

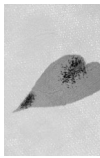

KIDNEY TISSUE

Kidney tissue can reflect the degree of systemic hypertension, where the severity of hypertension is positively correlated with damage in the kidney tissue.[24,25] Here we used histological analysis of corresponding kidney tissue to analyze the variability in severity of hypertension in our studied population in more detail. Kidney tissue embedded in paraffin was available for 16 controls and 20 hypertensive patients. Histological slides were prepared as mentioned above and stained with a Von Gieson stain for the vessel wall thickness and a periodic acid-Schiff-diastase stain for polysaccharides depositions. For the periodic acid-Schiff-diastase stain, slides were incubated in 0.25% diastase for 30 minutes at room temperature. After that, they were washed in water and incubated in 1% periodic acid for 10 minutes. The washing was repeated and the slides were incubated for 15 minutes in Schiff-reagent and subsequently for 5 minutes in Hematoxylin. Finally, the slides were dehydrated in ethanol (70%, 96% and 100%), xylene and covered with Pertex mounting medium (HistoLab 00801-EX).

Fifteen arterioles equally distributed throughout the section were analyzed by an experienced pathologist (J.J.T.H. Roelofs) for polysaccharide depositions. When 7 or more of these arterioles were positive for polysaccharides deposition the patient was marked as having kidney abnormalities. We compared the vessel wall thickness and area of patients with and without kidney abnormalities within the hypertensive group, to determine whether there is an effect of the severity of hypertension on the vessel wall thickness and area.

STATISTICAL ANALYSIS

Bland-Altman assessment for agreement was used to compare MRI vessel wall measurements and histological based vessel wall measurements. Additionally, we report the correlation coefficient between MRI and histology measurements for the vessel wall thickness and area.

A Mann-Whitney U test was used to test for significant differences in vessel wall thickness, and area between the hypertensive and control groups. A similar test was used to test for statistically significant differences in vessel wall thickness and area between male hypertensive and control groups, as well as female hypertensive and control groups. For testing of statistically significant differences in atherosclerotic plaque presence, we compared the percentage of advanced plaques against the percentage of early plaques and no anomalies using a Chi-square test per anatomical location. A Mann-Whitney U test was used to assess significant differences in collagen to smooth muscle ratio between hypertensive and control groups, per anatomical location. All tests were unadjusted for other factors, and a level of significance of $p < 0.05$ was used.

RESULTS

MRI VS HISTOLOGY

Over 9 anatomical locations and 49 specimens, 326 vessel wall thickness and area measurements were performed on both MR images and histological images. The measurements between both modalities were relatively comparable, yielding correlation coefficients of 0.76 and 0.87 for the thickness and area measurements respectively (Figure 3). On average, the vessel wall area measured from the MR images was overestimated by 0.43 mm^2 with limits of agreement (LoA) at -0.97 and 1.8 mm^2. Vessel wall thickness measurements were also overestimated when measured from MRI by on average 0.04 mm, with LoA at -0.12 and 0.19 mm.

For the SCA and AICA we observed a measured thickness from histology around or below the MR voxel size. Due to severe overestimation of the vessel wall thickness from the MR images for these locations, given the theoretical limit, we omitted the vessel wall thickness and area measurements for the SCA and AICA from further analyses.[26,27]

Because of anatomical heterogeneity of the circle of Willis in humans, and because of technical difficulties in complete dissection of the entire circle of Willis from the brain, not all anatomical locations could be measured in all specimens.[28–30] The PCoA was present in 20/49 specimens, followed by the VA (39/49), PCA (43/49), and BA (44/49). For the MCA, measurements were possible in all specimens; and for the ACA measurements were possible in 48 specimens.

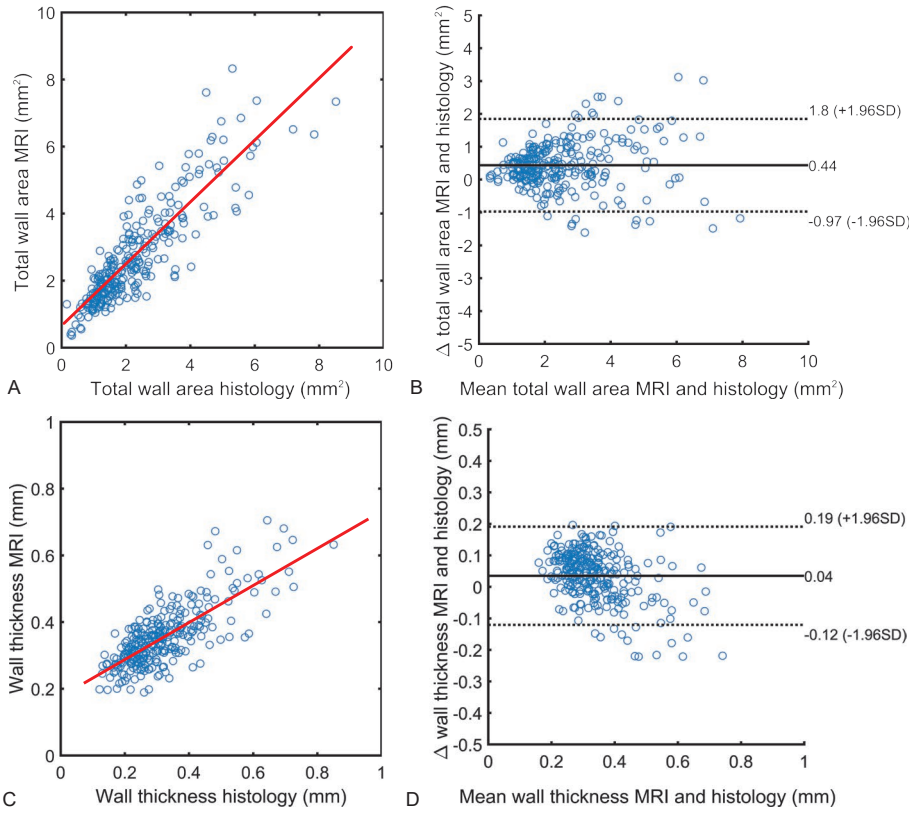

Figure 3. Comparison of vessel wall thickness and area measurements between MRI and histology. Scatter plot and Bland-Altman plot of the total vessel wall area (A, B) and mean vessel wall thickness (C, D) measured on histological sections against measurements on MR images. The line of best fit for the vessel wall area and thickness measurements is given by the red lines in (A) and (C), respectively. The equation for these fits is given as $y = 0.92x + 0.54$, and $y = 0.56x + 0.17$, with y the vessel wall area and thickness measured from MRI, and x the vessel wall area and thickness measured from histology, respectively.

HYPERTENSIVE VS CONTROL GROUPS

VESSEL WALL THICKNESS AND AREA

No statistically significant differences were found in vessel wall thickness between the hypertensive and control groups for both the MRI (U = 9307, p = 0.26) and histology measurements (U = 9824, p = 0.71, Figure 4). Also, the vessel wall area did not show any significant difference between the hypertensive and control groups (U = 9773, p = 0.81, and U = 9840, p = 0.88, respectively, Figure 4). Numerical values on the median vessel wall thickness and area measurements can be found in Tables 2 and 3. Similarly, for males and females separately, no statistically significant differences were observed in vessel wall thickness and area between hypertensive and control groups. However, the group size in this set was relatively small with 15 males and 9 females in the hypertensive group and 15 males and 10 females in the control group (data not shown).

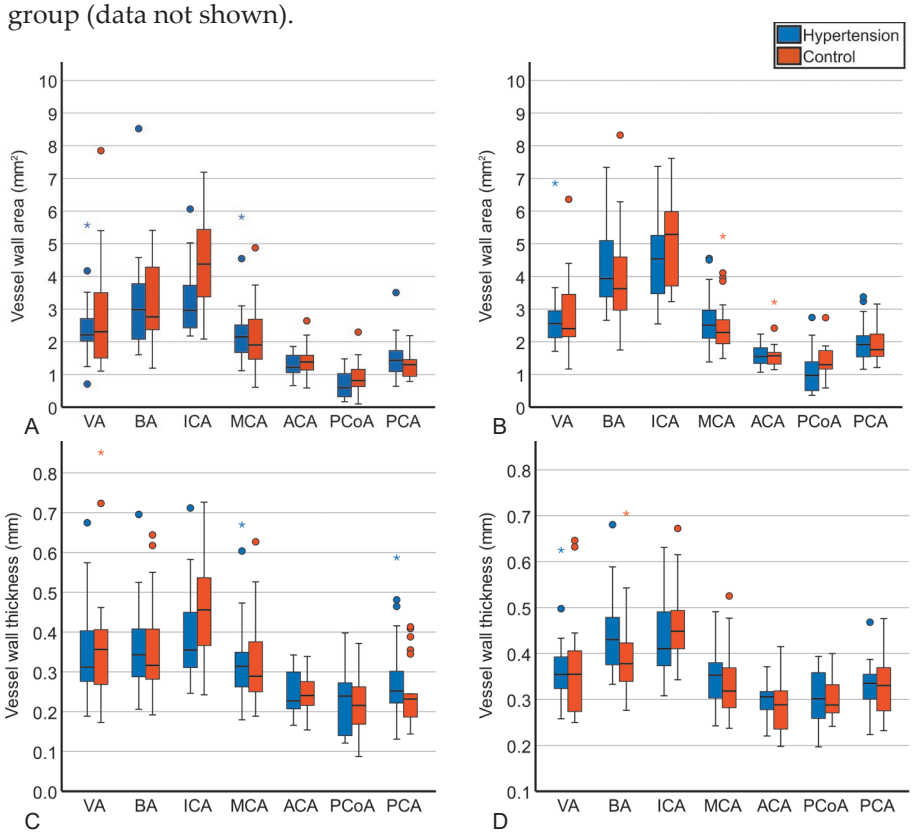

Figure 4. Box plots of the vessel wall thickness and area for the histology (A, C) and MRI (B, D) measurements. Measurements for the hypertensive group are given in blue, the control group in orange. Outliers that are more than 1.5 and 3 times the interquartile range away from the median are given by circles and stars, respectively.

Table 2. Vessel wall thickness measurements. Measurements are given for both MRI and histology as median (interquartile range), per anatomical location and for both the hypertension and control groups.

	MRI		Histology	
	Hypertension	**Control**	**Hypertension**	**Control**
VA	0.354 (0.072)	0.355 (0.136)	0.312 (0.141)	0.356 (0.149)
BA	0.430 (0.105)	0.378 (0.091)	0.343 (0.128)	0.316 (0.133)
ICA	0.410 (0.129)	0.448 (0.092)	0.355 (0.142)	0.456 (0.174)
MCA	0.353 (0.081)	0.318 (0.090)	0.315 (0.090)	0.289 (0.144)
ACA	0.305 (0.041)	0.288 (0.087)	0.227 (0.096)	0.240 (0.061)
PCoA	0.301 (0.115)	0.288 (0.079)	0.240 (0.147)	0.216 (0.095)
PCA	0.335 (0.071)	0.330 (0.097)	0.252 (0.082)	0.232 (0.087)

Table 3. Vessel wall area measurements. Measurements are given for both MRI and histology as median (interquartile range), per anatomical location and for both the hypertension and control groups.

	MRI		Histology	
	Hypertension	**Control**	**Hypertension**	**Control**
VA	2.555 (0.96)	2.403 (1.48)	2.212 (0.72)	2.310 (2.03)
BA	3.936 (1.76)	3.624 (1.69)	2.982 (1.75)	2.763 (2.01)
ICA	4.535 (2.05)	5.284 (2.36)	2.964 (1.34)	4.270 (2.18)
MCA	2.509 (0.91)	2.286 (0.77)	2.152 (0.92)	1.903 (1.35)
ACA	1.550 (0.50)	1.572 (0.36)	1.219 (0.58)	1.381 (0.46)
PCoA	0.970 (1.01)	1.30 (0.63)	0.593 (0.73)	0.812 (0.88)
PCA	1.918 (0.85)	1.76 (0.77)	1.435 (0.69)	1.300 (0.56)

ARTERIAL WALL COMPOSITION

From histological atherosclerotic plaque analysis, we observed that early plaques were present in both groups and in all analyzed arteries of the circle of Willis. Advanced plaques were present in almost all arteries of the circle of Willis, except for the AICA, that did not show any advanced plaques in both groups, and for the SCA, for which no advanced plaques were present in the control group (Figure 5A). For all locations, no statistically significant differences were found between the percentage of advanced plaques and percentage of early plaques together with no anomalies (VA: $\chi(1) = 1.405$, $p = 0.24$, BA: $\chi(1) = 2.400$, $p = 0.12$, ICA: $\chi(1) = 2.450$, $p = 0.12$, MCA: $\chi(1) = 3.365$,

p = 0.07, ACA: $\chi(1) = 0.740$, p = 0.39, ICA: $\chi(1) = 2.450$, p = 0.12, PCoA: $\chi(1) = 0.479$, p = 0.49, PCA: $\chi(1) = 0.040$, p = 0.84, SCA: $\chi(1) = 5.218$, p = 0.06, AICA: NA).

The collagen to smooth muscle ratio was calculated for all locations as a measure of arterial wall stiffness from histological analysis. In the hypertensive group, the ICA had a significantly increased collagen to smooth muscle ratio, as compared to the control group. When omitting the outlier measurement in the hypertensive group of the ICA (collagen to smooth muscle ratio of 37.3), significant differences between both groups remained (U = 177, p = 0.035). For the other locations, no significant difference was seen between the hypertensive and control groups (Figure 5B).

KIDNEY TISSUE

The kidney is well known to reflect systemic hypertension, because a significant percentage of systemic hypertension patients develop chronic kidney disease. The degree of hypertension is one of the determinants of the severity in renal dysfunction. Furthermore, the development of renal dysfunction is strongly correlated with poor cardiovascular outcome of these patients.[24,25] Here we analyzed the corresponding kidney tissue to get insight in the severity of hypertension of the patients in the hypertensive and control groups. Seven hypertensive patients (out of 20) showed kidney abnormalities, whereas 0 (out of 16) control patients showed kidney abnormalities. Analysis of the vessel wall thickness and area between the 7 hypertensive patients positive for kidney abnormalities and the 13 hypertensive patients negative for kidney abnormalities, showed no significant differences in vessel wall thickness (MRI: U = 1960, p = 0.873; histology: U = 1872, p = 0.574) and in vessel wall area (MRI: U = 1831, p = 0.454; histology: U = 1946, p = 0.823, data not shown).

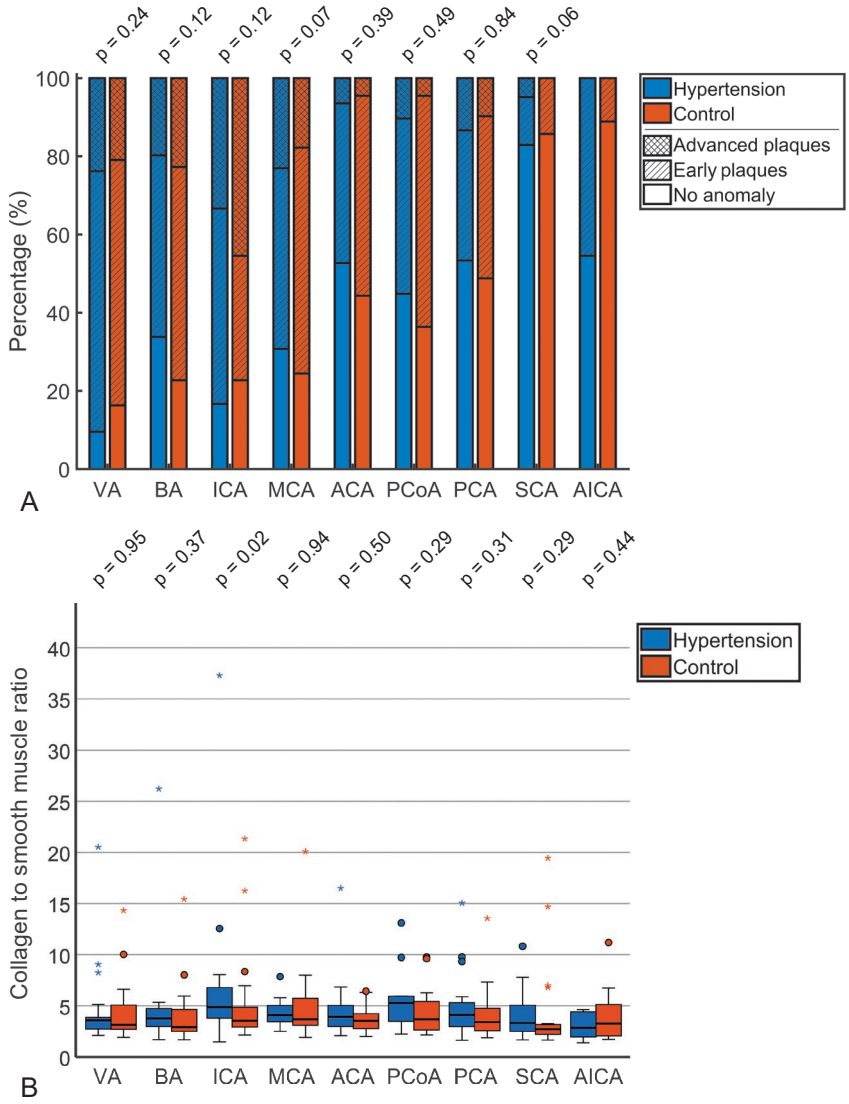

Figure 5. Analysis of vessel wall composition. (A) Plaque classification for hypertensive and control groups. Classifications for the hypertensive group are given in blue, the control group in orange. A Chi-square test was performed to assess statistically significant differences for each vascular location between the hypertensive and control groups. No significant difference was observed when comparing the percentage of advanced plaques with the percentage of no anomaly together with the early plaques. (B) Box plots for collagen to smooth muscle ratios for all locations. Measurements for the hypertensive group are given in blue, the control group in orange. Outliers that are more than 1.5 interquartile ranges away from the median are given by circles. Outlier more than 3 interquartile ranges away from the median are given by stars.

DISCUSSION

In this article, we aimed to investigate the potential differences in vessel wall thickness, area and vessel wall composition between hypertensive patients and controls. Forty-nine post-mortem circle of Willis specimens were included in this study, which originated from individuals with and without a history of hypertension. We extensively measured the aforementioned parameters at 21 locations along the circle of Willis, which were grouped into 9 anatomical locations.

MRI VS HISTOLOGY

We compared the vessel wall thickness and area measurements between MRI and histology, yielding comparable measurements, with a mean difference of 0.43 mm^2 (LoA: -0.97–1.8 mm^2) and 0.04 mm (LoA: -0.12–0.19 mm), respectively. This is in accordance to the values reported by Harteveld et al.[20]

VESSEL WALL THICKNESS AND AREA

Between hypertensive and control groups, no statistically significant differences were found in vessel wall thickness and area using either technique. Similarly, for males and females separately, no statistically significant differences were observed in vessel wall thickness and area between the hypertensive and control groups. This, in contrast to studies performed on extracranial arteries,[31–34] and several studies in the intracranial arteries of animal models[8,10,35] in which the vessel wall area and thickness were larger in hypertensive patients/animals than in normotensive patients/animals.

The vessel wall thickness measured for all anatomical locations ranged between 0.1 and 0.6 mm. For the smallest arteries, the AICA and SCA, with a thickness around or below 0.1 mm, the acquired resolution of our ex vivo MRI acquisition (0.11 mm isotropic) was not sufficient for accurate thickness measurements. Antiga et al.[27] and van Hespen et al.[26] have shown that for accurate vessel wall thickness measurements from MRI, the vessel wall thickness needs to be at least twice the acquired voxel size. This requirement is not met for the AICA and SCA. For this reason, we have removed the AICA and SCA from further vessel wall thickness and area analyses. In an in vivo setting, this inaccuracy problem will also play a major role for the other anatomical locations, because commonly used in vivo MRI acquisitions have acquired voxel sizes between 0.5 and 0.8 mm isotropic. However, research

focused on subvoxel thickness measurements using deep learning has shown that accurate measurements for vessel walls thinner than the voxel size are possible.[36] With the use of such new analysis methods, quantification of vascular remodeling of the intracranial arteries in an in vivo setting—if any is even present—would be possible. However, such methods would still benefit from an increased acquired image resolution. By imaging at even higher field strengths or by implementing acceleration techniques such as compressed sensing, an increase in acquired image resolution can be achieved with adequate signal to noise ratio and in clinically feasible scan times.[37]

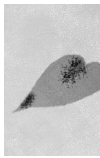

ARTERIAL WALL COMPOSITION

Histological analysis has shown that only for the ICA, the collagen to smooth muscle ratio, as a measure of arterial stiffness, was significantly higher in the hypertensive group compared to the control group. In contrast, Neumann et al.[38] reported no increase in arterial stiffness, measured from phase contrast (velocity) MR images (PC-MRI) using the pulse wave velocity, in the ICA compared to the aorta of hypertensive patients. The authors suggested that this could be a result of adaptation of the ICA to protect the brain against elevated blood pressure or that this result was biased by technical limitations of measuring the pulse wave velocity in the ICA. Our study is, to the best of our knowledge, the first study comparing arterial stiffness in the individual arteries of the circle of Willis.

In the future, the use of in vivo PC-MRI to measure the vessel wall stiffness of all (other) large arteries of the circle of Willis should be explored. Complementary to stiffness measurements,[39] PC-MRI has enabled the measurement of the wall shear stress, an important biomarker for vessel wall thickening and endothelial cell rearrangement.[40]

For the composition of the vessel wall, histological analysis has shown the presence of early and advanced plaques for almost all locations for both the hypertensive as well as the control group. A similar distribution of plaque severity across the larger arteries of the circle of Willis was observed by Denswil et al.,[21] where circle of Willis specimens from randomly chosen hospital patients were investigated. In a hypertensive animal model, Hollander et al.[41] observed that hypertension is important factor in atherosclerotic plaque severity. However, in this study no antihypertensive medication was administered to the animals. Potentially, in our population a significant effect was not observable, because most hypertensive patients were treated

with antihypertensive drugs, slowing down potential severe atherosclerotic plaque development.

Our results suggest a less detrimental or different effect of hypertension on the vessel wall in the human intracranial arteries compared to the extracranial arteries studied in above-mentioned literature, making the intracranial arteries less prone to vessel wall changes induced by hypertension. Moreover, the circle of Willis is thought to function as a pressure dissipation system, which may make the individual arteries of the circle of Willis less prone to blood pressure changes such as those caused by hypertension, which may result in no or only minor changes in vessel wall characteristics.[42,43] Furthermore, autoregulation in the brain microcirculation and arteries of the circle of Willis, can diminish the effect of hemodynamic disturbances to a certain extent.[44–46] Moreover, an increase in blood pressure can result in an increase in cerebrovascular resistance that is accomplished by an increase in vascular smooth muscle cell tone. In our study we observed an increase in collagen to smooth muscle ratio in the ICA of the hypertensive group compared to the control group, which was not seen for the other locations. This suggests that the ICA, being the direct derivative of the common carotid artery, could change its vessel wall composition rather than its total thickness and area, playing an important role in stabilizing blood flow changes and thereby in the autoregulation upon high blood pressure.[44–46]

KIDNEY TISSUE

Thirteen out of 20 patients with a medical history of elevated blood pressure and/or usage of antihypertensive drugs showed none or few abnormalities in kidney tissue, suggesting variability in severity and duration of hypertension between the patients. This is in accordance to earlier mentioned literature in which renal damage was positively related to hypertension severity.[24,25] In our study, comparing hypertensive patients with and without kidney tissue abnormalities did not change our results of vessel wall thickness and area, suggesting that the obtained results are not biased by the severity of hypertension.

LIMITATIONS

Several factors could have influenced our findings. The main limitation of our study is the difference in the distribution of cause of death between the hypertensive and control groups. In the control group 8 patients suffered from

ALS, whereas only 1 ALS-patient was included in the hypertensive group. However, no significant changes were observed for the overall thickness and area measurements between the 8 ALS-patients and the 17 non-ALS patients within the control group (data not shown). Additionally, specimens were selected from autopsy cases with available ex vivo circle of Willis material. The cause of death in these cases (Table 1), for which autopsy was required, is likely different than for the general population.

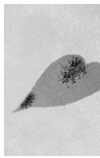

Observable differences in vessel wall thickness and area measurements between the hypertensive and control groups were potentially influenced by the possibility of anatomical variations of multiple vascular locations in the circle of Willis, as is known for the VA and the PCA.[28–30] Such anatomical variation increases the variability in vessel wall thickness and area measurements. However, due to the large number of included specimens and measurements, as well as averaging over multiple measurement locations in vessels of the same anatomical locations, the effect of this variability is potentially low. Furthermore, for the smaller vascular locations, measurements were sometimes not possible due to missing vessels after post-mortem extraction, or due to the presence of blood or air, which complicated accurate MRI measurements. In such cases, measurements were omitted from the statistical analyses. In addition, dissection of the circle of Willis from the brain could potentially damage the adventitia of the vessel wall resulting in an underestimation of the vessel wall thickness and area, for both MRI and histology since both analyses were performed after dissection of the circle of Willis from the brain. However, visual inspection did not show complete absence of the adventitia. At most, a (small) part of the adventitia was dissected during post-mortem extraction.

The observed difference between histology and MRI measurements is likely due to differences in measurement methods. From histology, the average vessel wall thickness was calculated as the average of five equidistant positions along the vessel cross section.[47] Literature has shown that such measurements are potentially biased and slightly less precise than the MRI-based thickness method, that uses more measurements locations along the vessel wall. Additionally, measurements were performed next to fiducials placed in the agarose solution. Because both raters performed measurements independently of each other, the measurement locations could be slightly different. However, variation in vessel wall thickness and area along the vessel is assumed to be small over short distances.[20] For similar reasons, if

we would have chosen different measurement locations for each anatomical location, the results would be largely the same.

We were also limited by the retrospective design of this study. Variance in duration of hypertensive status, and duration and compliance of treatment, were not known, and could have an effect on the observed findings. Nonetheless, even in the case of a long duration of antihypertensive treatment, we would still expect to observe changes to the vessel wall, that were induced prior to the treatment. Similarly, we did not adjust for common risk factors that are associated with changes to the vessel wall in our analyses. These risk factors were not always known from the patient history. We also did not adjust for age, a major predictor for hypertension, in our analyses. We reduced the effect of age on our results by balancing the age in both the hypertensive and control groups, which was not significantly different.

In conclusion, we showed with MRI and histology, that in our studied population when unadjusted for other factors, no differences in vessel wall thickness and area were observed between the hypertensive and control group, and that using histological analysis, the arterial stiffness of the ICA was significantly increased in hypertensive patients.

Even though the large intracranial arteries play a major role in cerebrovascular disease progression, only few studies have looked at the effect of hypertension on arterial remodeling of these arteries. In this study, we have extensively investigated hypertensive arterial remodeling, by morphological measurements and vessel wall composition measurements at multiple vascular locations along the human circle of Willis. Given our vessel wall measurements, our study suggests that the effect of hypertension on arterial remodeling of the larger intracranial arteries is minimal and will likely not be measurable from in vivo MR acquisitions. An extensive ex vivo study with an even more narrow hypertension criteria or a gradation in hypertension severity would possibly be very informative in elucidating the effect of hypertension severity on the vessel wall composition.

ACKNOWLEDGMENTS

We would like to thank the Dr. W. van Hecke of the UMC Utrecht pathology department for supplying the human specimens. Additionally, we would like to thank L. M. Foppen, BSc for his help with the histopathological analysis and J.J.T.H. Roelofs MD, PhD for his help with the analysis of kidney tissue.

REFERENCES

1. Weber MA, Schiffrin EL, White WB, et al. Clinical Practice Guidelines for the Management of Hypertension in the Community. J Clin Hypertens. 2014;16:14-26.

2. Forouzanfar MH, Alexander L, Bachman VF, et al. Global, regional, and national comparative risk assessment of 79 behavioural, environmental and occupational, and metabolic risks or clusters of risks in 188 countries, 1990-2013: A systematic analysis for the Global Burden of Disease Study 2013. Lancet. 2015;386:2287-2323.

3. Iadecola C, Davisson RL. Hypertension and Cerebrovascular Dysfunction. Cell Metab. 2008;7:476-484.

4. Intengan HD, Schiffrin EL. Vascular remodeling in hypertension. Hypertension. 2001;38:581-587.

5. Pires PW, Dams Ramos CM, Matin N, Dorrance AM. The effects of hypertension on the cerebral circulation. Am J Physiol Heart Circ Physiol. 2013;304:H1598-614.

6. Schiffrin EL. Effects of antihypertensive drugs on vascular remodeling: do they predict outcome in response to antihypertensive therapy? Curr Opin Nephrol Hypertens. 2001;10:617-624.

7. Mulvany MJ. Small Artery Remodeling and Significance in the Development of Hypertension. Physiology. 2002;17:105-109.

8. Izzard AS, Horton S, Heerkens EH, Shaw L, Heagerty AM. Middle cerebral artery structure and distensibility during developing and established phases of hypertension in the spontaneously hypertensive rat. J Hypertens. 2006;24:875-880.

9. Hajdu MA, Baumbach GL. Mechanics of large and small cerebral arteries in chronic hypertension. Am J Physiol Circ Physiol. 1994;266:H1027-H1033.

10. Hu J-J, Fossum TW, Miller MW, Xu H, Liu J-C, Humphrey JD. Biomechanics of the Porcine Basilar Artery in Hypertension. Ann Biomed Eng. 2006;35:19-29.

11. Qiao Y, Guallar E, Suri FK, et al. MR Imaging Measures of Intracranial Atherosclerosis in a Population-based Study. Radiology. 2016;280:860-868.

12. Küker W, Gaertner S, Nägele T, et al. Vessel wall contrast enhancement: A diagnostic sign of cerebral vasculitis. Cerebrovasc Dis. 2008;26:23-29.

13. Kathuveetil A, Sylaja PN, Senthilvelan S, Chandrasekharan K, Banerjee M, Jayanand Sudhir B. Vessel Wall Thickening and Enhancement in High-Resolution Intracranial Vessel Wall Imaging: A Predictor of Future Ischemic Events in Moyamoya Disease. Am J Neuroradiol. 2020;41:100-105.

14. Cogswell PM, Lants SK, Davis LT, Donahue MJ. Vessel wall and lumen characteristics with age in healthy participants using 3T intracranial vessel wall magnetic resonance imaging. J Magn Reson Imaging. 2019;50:1452-1460.

15. Mossa-Basha M, de Havenon A, Becker KJ, et al. Added Value of Vessel Wall Magnetic Resonance Imaging in the Differentiation of Moyamoya Vasculopathies in a Non-Asian Cohort. Stroke. 2016;47:1782-1788.

16. De Ciuceis C, Cornali C, Porteri E, et al. Cerebral small-resistance artery structure and cerebral blood flow in normotensive subjects and hypertensive patients. Neuroradiology. 2014;56:1103-1111.

17. Rizzoni D, De Ciuceis C, Porteri E, et al. Altered structure of small cerebral arteries in patients with essential hypertension. J Hypertens. 2009;27:838-845.

18. Chobanian A V. The Seventh Report of the Joint National Committee on Prevention, Detection, Evaluation, and Treatment of High Blood Pressure. JAMA. 2003;289:2560.

19. van der Kolk AG, Zwanenburg JJM, Denswil NP, et al. Imaging the Intracranial Atherosclerotic Vessel Wall Using 7T MRI: Initial Comparison with Histopathology. Am J Neuroradiol. 2015;36:694-701.

20. Harteveld AA, Denswil NP, Van Hecke W, et al. Ex vivo vessel wall thickness measurements of the human circle of Willis using 7T MRI. Atherosclerosis. 2018;273:106-114.

21. Denswil NP, van der Wal AC, Ritz K, et al. Atherosclerosis in the circle of Willis: Spatial differences in composition and in distribution of plaques. Atherosclerosis. 2016;251:78-84.

22. Ritter F, Boskamp T, Homeyer A, et al. Medical Image Analysis. IEEE Pulse. 2011;2:60-70.

23. Virmani R, Kolodgie FD, Burke AP, Farb A, Schwartz SM. Lessons From Sudden Coronary Death. Arterioscler Thromb Vasc Biol. 2000;20:1262-1275.

24. Segura J, Campo C, Gil P, et al. Development of chronic kidney disease and cardiovascular prognosis in essential hypertensive patients. J Am Soc Nephrol. 2004;15:1616-1622.

25. Mennuni S, Rubattu S, Pierelli G, Tocci G, Fofi C, Volpe M. Hypertension and kidneys: Unraveling complex molecular mechanisms underlying hypertensive renal damage. J Hum Hypertens. 2014;28:74-79.

26. van Hespen KM, Zwanenburg JJM, Harteveld AA, Luijten PR, Hendrikse J, Kuijf HJ. Intracranial Vessel Wall Magnetic Resonance Imaging Does Not Allow for Accurate and Precise Wall Thickness Measurements. Stroke. 2019;50.

27. Antiga L, Wasserman BA, Steinman DA. On the overestimation of early wall thickening at the carotid bulb by black blood MRI, with implications for coronary and vulnerable plaque imaging. Magn Reson Med. 2008;60:1020-1028.

28. Thierfelder KM, Baumann AB, Sommer WH, et al. Vertebral artery hypoplasia: frequency and effect on cerebellar blood flow characteristics. Stroke. 2014;45:1363-1368.

29. Park JH, Kim JM, Roh JK. Hypoplastic vertebral artery: Frequency and associations with ischaemic stroke territory. J Neurol Neurosurg Psychiatry. 2007;78:954-958.

30. Iqbal S. A comprehensive study of the anatomical variations of the circle of willis in adult human brains. J Clin Diagn Res. 2013;7:2423-2427.

31. Litwin M, Niemirska A, Śladowska J, et al. Left ventricular hypertrophy and arterial wall thickening in children with essential hypertension. Pediatr Nephrol. 2006;21:811-819.

32. Park JB, Schiffrin EL. Small artery remodeling is the most prevalent (earliest?) form of target organ damage in mild essential hypertension. J Hypertens. 2001;19:921-930.

33. Suurküla M, Fagerberg B, Wendelhag I, Agewall S, Wikstrand J. Atherosclerotic Disease in the Femoral Artery in Hypertensive Patients at High Cardiovascular Risk. Arterioscler Thromb Vasc Biol. 1996;16:971-977.

34. Chironi G, Gariepy J, Denarie N, et al. Influence of hypertension on early carotid artery remodeling. Arterioscler Thromb Vasc Biol. 2003;23:1460-1464.

35. Baumbach GL, Dobrin PB, Hart MN, Heistad DD. Mechanics of cerebral arterioles in hypertensive rats. Circ Res. 1988;62:56-64.

36. van Hespen KM, Zwanenburg JJM, Hendrikse J, Kuijf HJ. Subvoxel vessel wall thickness measurements of the intracranial arteries using a convolutional neural network. Med Image Anal. 2021;67:101818.

37. Donoho DL. Compressed sensing. IEEE Trans Inf Theory. 2006;52:1289-1306.

38. Neumann S, Sophocleous F, Kobetic MD, et al. Wave intensity analysis in the internal carotid artery of hypertensive subjects using phase-contrast MR angiography and preliminary assessment of the effect of vessel morphology on wave dynamics. Physiol Meas. 2018;39:104003.

39. Coolen BF, Calcagno C, van Ooij P, Fayad ZA, Strijkers GJ, Nederveen AJ. Vessel wall characterization using quantitative MRI: what's in a number? Magn Reson Mater Physics, Biol Med. 2018;31:201-222.

40. Peper ES, Gottwald LM, Zhang Q, et al. Highly accelerated 4D flow cardiovascular magnetic resonance using a pseudo-spiral Cartesian acquisition and compressed sensing reconstruction for carotid flow and wall shear stress. J Cardiovasc Magn Reson. 2020;22:7.

41. Hollander W, Prusty S, Kemper T, Rosene DL, Moss MB. The effects of hypertension on cerebral atherosclerosis in the cynomolgus monkey. Stroke. 1993;24:1218-1226.

42. Hermkens DMA, Stam OCG, De Wit NM, et al. Profiling the unique protective properties of intracranial arterial endothelial cells. Acta Neuropathol Commun. 2019;7:151.

43. Vrselja Z, Brkic H, Mrdenovic S, Radic R, Curic G. Function of Circle of Willis. J Cereb Blood Flow Metab. 2014;34:578-584.

44. Kennedy McConnell FA, Payne SJ. The Dual Role of Cerebral Autoregulation and Collateral Flow in the Circle of Willis After Major Vessel Occlusion. IEEE Trans Biomed Eng. 2017;64:1793-1802.

45. Kennedy McConnell FA, Payne SJ. Autoregulating Cerebral Tissue Selfishly Exploits Collateral Flow Routes Through the Circle of Willis. In: Heldt T, ed. Acta Neurochirurgica, Supplementum. Cham: Springer; 2018:275-279.

46. Warnert EAH, Hart EC, Hall JE, Murphy K, Wise RG. The major cerebral arteries proximal to the Circle of Willis contribute to cerebrovascular resistance in humans. J Cereb Blood Flow Metab. 2016;36:1384-1395.

47. Rosero EB, Peshock RM, Khera A, Clagett GP, Lo H, Timaran C. Agreement between methods of measurement of mean aortic wall thickness by MRI. J Magn Reson Imaging. 2009;29:576-582.

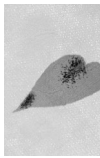

CHAPTER 3

Intracranial vessel wall MRI does not allow for accurate and precise wall thickness measurements

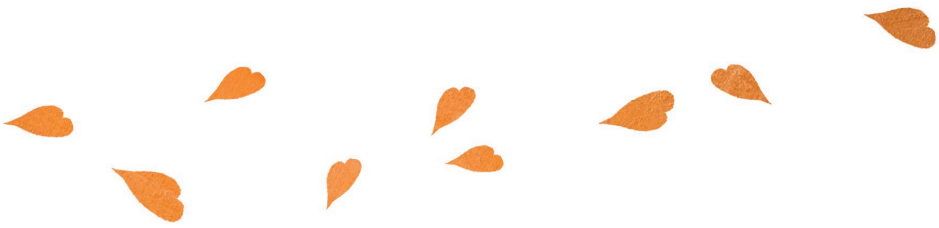

PUBLISHED AS:

STROKE. 2019;50.

Kees M. van Hespen, Jaco J.M. Zwanenburg, Anita A. Harteveld, Peter R. Luijten, Jeroen Hendrikse, Hugo J. Kuijf.

Intracranial Vessel Wall Magnetic Resonance Imaging Does Not Allow for Accurate and Precise Wall Thickness Measurements.

ABSTRACT

PURPOSE

In this study, we aimed to determine the accuracy and precision of vessel wall thickness measurements performed on vessel wall magnetic resonance (MR) images.

MATERIALS AND METHODS

MR imaging of 12 human circle of Willis specimens was performed, using an ultra-high-resolution sequence (3D gradient echo, isotropic acquired voxel size: 0.11 mm) and a clinically-used low-resolution sequence (3D MPIR-TSE, isotropic acquired voxel size: 0.8 mm). Hereafter, an automatic algorithm was employed to measure the vessel wall thickness of the middle cerebral artery, M1 segment. The reference thickness, measured from ultra-high-resolution images, was compared with measurements from the low-resolution images.

RESULTS

The reference thickness showed excellent agreement with previously validated manual measurements on histology (median difference: 0.04 mm, interquartile range: 0.08 mm). Vessel walls thinner than 1 mm were measured inaccurately from the low-resolution images. Vessel walls within this submillimeter range were measured at a similar thickness, given the measurements from the low-resolution images. For thicker vessel walls, e.g. advanced plaques, the vessel wall thickness could be accurately measured from the low-resolution images.

CONCLUSION

Vessel wall thickness measurements from low-resolution images acquired with an in vivo MR protocol are prone to bias and inaccuracy when the true thickness is around or below the voxel size. Accurate thickness measurements require an isotropic voxel size of 0.2 mm or smaller.

INTRODUCTION

In recent years, magnetic resonance imaging (MRI) sequences have been developed that enabled the visualization of the intracranial vessel walls.[1,2] These vessel wall MRI sequences are for example used in the detection of vasculitis, based on post-contrast enhancement of segments of the intracranial arterial vessel wall, and in the detection of subtle lesions, including larger and smaller intracranial atherosclerotic plaques.[3,4] Vessel wall MRI is, similar to the extracranial vasculature,[5,6] also used for the quantification of vessel wall thickening in the intracranial arterial arteries.[2,7–11]

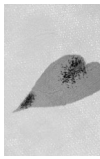

Unfortunately, the spatial resolution of the used vessel wall MR acquisitions thwarts reliable thickness measurements, because for reliable measurements vessel walls need to span at least two image voxels.[12] This is not feasible as acquisition schemes commonly have voxel sizes between 0.5 and 0.8 mm, while vessel wall thicknesses of the larger arteries of the circle of Willis range between 0.3 and 0.5 mm. This results in an overestimation of the true vessel wall thickness, as demonstrated in a simulation study by Antiga et al.[12] However, research on the overestimation of the vessel wall thickness on actual vessel wall MR images is lacking.

In this study, we aimed to quantify the accuracy and precision of vessel wall thickness measurements on MR images of circle of Willis specimens scanned with a clinical-used vessel wall MR sequence, and an ultra-high-resolution sequence.

MATERIALS AND METHODS

SPECIMEN DATA

In this retrospective, institutional review board (TCBio: 15-068) approved study, data from previously published work was used.[13] This data consisted of 15 post-mortem human specimens of the circle of Willis, collected between 2008 and 2015. Thickness measurements were performed on the M1 segment of the middle cerebral artery (MCA), because the MCA is one of the most common locations of atherosclerosis and should therefore provide a large range of possible thickness values within the intracranial vasculature.[14,15] Out of the 15 specimens, one was excluded because of missing both MCAs, and two due to MCA collapse, where no lumen existed between two sides of the vessel wall, yielding poor delineation of the vessel wall in the images.

The twelve remaining specimens belonged to patients with a mean age of 76 years (range: 66–84 years), of which seven belonged to symptomatic stroke patients.

MRI ACQUISITION

Imaging was performed at room temperature on a 7T human platform (Philips, Best, The Netherlands). A custom-made high-density receive coil (16 channels per 70 cm^2) was used. For transmission, a volume transmit coil was used. The specimens, embedded on a petri dish in 2% agarose solution, were imaged two at a time. The receive coils were placed above and below the two stacked specimens. All specimens were imaged using an ultra-high-resolution sequence and a clinically feasible sequence (further referred to as low-resolution sequence), obtained in the same imaging session (Figure 1). The ultra-high-resolution images were performed with a 3D gradient echo sequence (field of view (FOV): 95x130x35 mm^3; acquired resolution: 0.11x0.11x0.11 mm^3; repetition time/echo time: 55/6.2 ms; flip angle: 28 degrees; number of signal averages (NSA): 1; acquisition time: 5h46m). For the low-resolution images a clinically-used 3D magnetization preparation inversion recovery gradient echo (3D MPIR-TSE[3,16]) scan protocol was used (FOV: 150x150x40 mm^3; acquired resolution: 0.8x0.8x0.8 mm^3; repetition time/ echo time : 1700/33 ms; inversion time: 650 ms; flip angle: 90 degrees; NSA: 2; acquisition time: 8m35s).

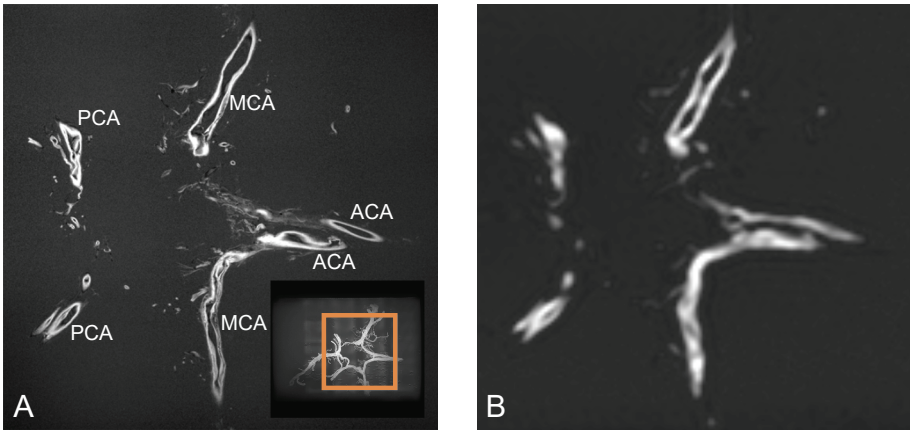

Figure 1. (A) Ultra-high-resolution and (B) low-resolution acquisition of a circle of Willis specimen. In the shown cross section, the middle cerebral arteries (MCA), anterior cerebral arteries (ACA), and posterior cerebral arteries (PCA) can be appreciated. Inset in (A): Maximum intensity projection of the ultra-high-resolution image with the bounding box in orange marking the region shown for both subpanels.

IMAGE PROCESSING

After acquisition, N4 bias field correction was applied to all images.[17] A mask of the vessel walls was acquired by thresholding the ultra-high-resolution images using Otsu's method.[18] By eroding the vessel wall mask, a skeleton was acquired (Figure 2). Thickness measurements were performed on the ultra-high- and low-resolution images at the locations of the skeleton points.

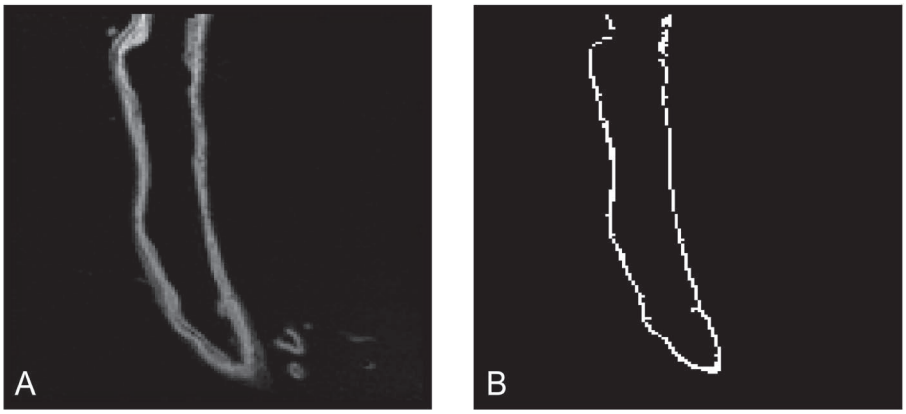

Figure 2. Skeletonization. (A) Cross section of an ultra-high-resolution scan, (B) Skeletonization result corresponding to the image in (A).

THICKNESS MEASUREMENT

For each point on the skeleton, an intensity profile of 5 mm in length was acquired along the surface normal, the line perpendicular to the vessel wall surface (Figure 3). The orientation of the surface normal was computed as the direction of the image gradient vector at the location of the skeleton point. The image gradient vector was composed of the directional image gradient in the x, y, and z directions.

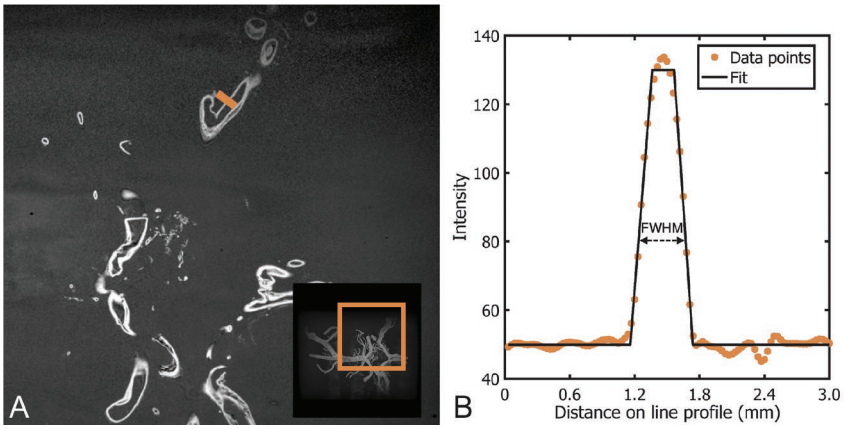

Figure 3. Method measuring the vessel wall thickness. (A) Slice through a vessel wall magnetic resonance image (0.11 mm isotropic resolution) of a specimen. In orange, a line perpendicular to the vessel wall surface is given. The intensity values of the image along this line are used to calculate the corresponding vessel wall thickness at the location of the orange line. (B) Intensity profile corresponding to the perpendicular line in (A) (orange). The black line represents the fitted piecewise linear function. The full-width-at-half-maximum (FWHM) of this fit is given by the dashed black line.

To estimate the vessel wall thickness from the intensity profile, two subsequent mathematical functions were fit to the intensity profile. Initially, a piecewise linear fit was performed, where the piecewise linear function is given by:

$$I_{est}(x) = \begin{cases} B & x < x_1, \\ B + \dfrac{I - B}{x_2 - x_1} \cdot (x - x_1) & x_1 < x < x_2, \\ I & x_2 < x < x_3, \\ I + \dfrac{B - I}{x_4 - x_3} \cdot (x - x_3) & x_3 < x < x_4, \\ B & x > x_4 \end{cases}$$

Where I_{est} is the estimated intensity along x, the location along the intensity profile. B is the background intensity and I is the vessel wall intensity, and x_1, x_2, x_3, x_4 are the knots that determine the position of the slopes along the profile. In several instances, the intensity profile also (partially) included the vessel wall on the other side of the vessel, giving spurious results from our piecewise linear fit. In that case, a bimodal Gaussian fit was performed. For the bimodal Gaussian fit, the mode closest to the center of the intensity profile was taken as fit for the current vessel wall. Finally, the vessel wall thickness was measured as the full-width-at-half-maximum of the piecewise linear- or Gaussian-fit.

EXPERIMENTAL SETUP

VALIDATION WITH MANUAL THICKNESS MEASUREMENTS

The vessel wall thickness measured using our automatic algorithm was compared to manual measurements by Harteveld et al.[13] at the same anatomical locations. In their study, the vessel wall thickness was measured on the ultra-high-resolution images from manually drawn inner and outer vessel wall contours. The contours were drawn on multi planar reconstructions (MPR) of the image, along a center line through the vessel lumen. They reported the average vessel wall thickness per MPR slice. In our study, an MPR of the skeleton image was created along the same center line. The vessel wall thickness of the skeleton points that were reconstructed to the same MPR slices were averaged.

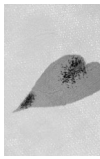

ULTRA-HIGH- AND LOW-RESOLUTION COMPARISON

The main goal of this study was to determine the relationship between the vessel wall thickness measured from the ultra-high-resolution and the low-resolution images. To this end, we compared the vessel wall thickness measured in both images using our algorithm. A one to one comparison between the thickness measurements was made at the same skeleton point locations. In total, skeleton points were generated for 24.000 voxels over all included specimens, on which the thickness measurements were performed in both images.

RESULTS

VALIDATION WITH MANUAL THICKNESS MEASUREMENTS

In the first analysis the automatic thickness measurements were compared with the histologically validated manual measurements by Harteveld et al.[13] The vessel wall thickness obtained with the automatic algorithm was very similar to the manual measurements. On average, the median difference between the thickness measured using our automatic algorithm and the manual measurements was -0.04 mm, with an interquartile range of 0.08 mm.

ULTRA-HIGH- AND LOW-RESOLUTION COMPARISON

Vessel walls thinner than 1 mm were measured inaccurately on the low-resolution images (Figure 4). Vessel walls in the sub millimeter range appear to have the same thickness given our measurements. For thicker vessel walls, e.g. advanced plaques, the vessel wall thickness can be accurately measured.

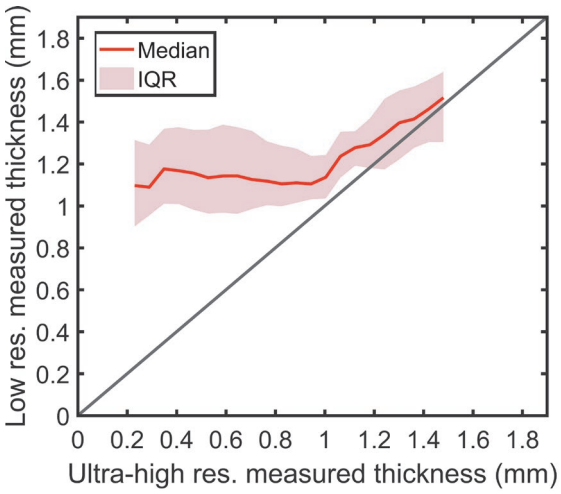

Figure 4. Ultra-high-resolution vs low-resolution thickness measurements. The median measured vessel wall thickness (red), calculated from the low-resolution images given against the vessel wall thickness measured from the ultra-high-resolution images. The shaded area indicates the interquartile range (IQR) of the measurements. The $y = x$ line is given in dark gray. For walls thinner than 1 mm, the thickness cannot be accurately measured from the low-resolution images.

DISCUSSION

Our results show that normal or slightly thickened vessel walls cannot be measured reliably. The measured vessel wall thickness deviates considerably from the reference thickness for vessel walls thinner than 1.0 mm. For vessel walls with a thickness between 0.2 and 1.0 mm, measurements on the low-resolution images were indistinguishable from each other (median thickness = 1.1 mm; interquartile range = 0.3 mm), confirming the simulations of Antiga et al.[12] with real imaging data. The relatively poor precision, given by the interquartile range, prevents potential post-hoc corrections of the measured vessel wall thickness. Only vessel walls thicker than 1 mm, e.g. advanced plaques, could be measured accurately from the low-resolution images.

The clinical application of the vessel wall thickness as a biomarker seems unfeasible given these results, as early vessel wall thickening remains undetected. This will likely hold for other acquisitions with different voxel sizes, although the limit of detection might shift slightly. Although the ex vivo nature of this study might not directly translate to clinical in vivo measurements, the accuracy and precision of vessel wall thickness measurements was assessed in a best-case scenario.

In vivo acquisitions are challenged by motion artifacts and blood flow pulsation, which will have an added detrimental effect on thickness measurements. Additionally, vessel wall MR acquisitions are dependent on the suppression of cerebrospinal fluid signal, and slow flowing blood signal. In case of insufficient suppression of slow flowing blood, the apparent vessel wall thickness increases.[19,20] Next to that, the point spread function of the used MR acquisition has a negative effect on the overall image resolution and thickness measurements as well.[21]

Our results, in accordance to the measurements by Antiga et al.,[12] pose a significant challenge to the MR community to further improve measurement accuracy. Currently, the signal-to-noise ratio and acquisition duration are major limitations for high-resolution acquisitions. Ongoing technological developments, including higher field strengths and compressed sensing may allow for higher spatial resolutions in the future.[22] Nonetheless, accurate measurements of the thinnest vessel walls theoretically require a resolution of 0.15 mm isotropic. This resolution will likely remain unfeasible for a long period of time as the voxel volume and signal-to-noise ratio are an order of magnitude smaller than the currently highest resolution acquisitions. Alternatively, the use of image processing methods such as deep learning, that can learn relevant image features related to the vessel wall thickness, can be explored.

In conclusion, the use of the vessel wall thickness as a biomarker for disease progression should be avoided for vessel walls thinner than 1 mm, given current image resolutions. This ex vivo study confirms the severe overestimation of thickness measurements around and below the acquired voxel size. Additionally, we show that poor precision prohibits post-hoc corrections and prevents distinction between healthy vessel walls and early vessel wall thickening owing to disease.

ACKNOWLEDGMENTS

We thank Anja van der Kolk, MD, PhD, from the Department of Radiology, University Medical Center Utrecht, for valuable comments on the article.

REFERENCES

1. Dieleman N, van der Kolk AG, Zwanenburg JJM, et al. Imaging Intracranial Vessel Wall Pathology With Magnetic Resonance Imaging. Circulation. 2014;130:192-201.

2. Mandell DM, Mossa-Basha M, Qiao Y, et al. Intracranial vessel wall MRI: Principles and expert consensus recommendations of the American society of neuroradiology. Am J Neuroradiol. 2017;38:218-229.

3. van der Kolk AG, Zwanenburg JJM, Brundel M, et al. Intracranial Vessel Wall Imaging at 7.0-T MRI. Stroke. 2011;42:2478-2484.

4. Obusez EC, Hui F, Hajj-ali RA, et al. High-Resolution MRI Vessel Wall Imaging: Spatial and Temporal Patterns of Reversible Cerebral Vasoconstriction Syndrome and Central Nervous System Vasculitis. Am J Neuroradiol. 2014;35:1527-1532.

5. Bots ML, Evans GW, Tegeler CH, Meijer R. Carotid Intima-media Thickness Measurements. Chin Med J (Engl). 2016;129:215-226.

6. Uthoff H, Staub D, Meyerhans A, et al. Intima-Media Thickness and Carotid Resistive Index: Progression Over 6 Years and Predictive Value for Cardiovascular Events. Ultraschall der Medizin - Eur J Ultrasound. 2008;29:604-610.

7. Qiao Y, Guallar E, Suri FK, et al. MR Imaging Measures of Intracranial Atherosclerosis in a Population-based Study. Radiology. 2016;280:860-868.

8. Suri MFK, Qiao Y, Ma X, et al. Prevalence of Intracranial Atherosclerotic Stenosis Using High-Resolution Magnetic Resonance Angiography in the General Population: The Atherosclerosis Risk in Communities Study. Stroke. 2016;47:1187-1193.

9. Park JK, Lee S, Sim KB, Huh JS, Park JC. Imaging of the walls of saccular cerebral aneurysms with double inversion recovery black-blood sequence. J Magn Reson Imaging. 2009;30:1179-1183.

10. Yuan M, Liu Z, Wang Z, Li B, Xu L, Xiao X. High-resolution MR imaging of the arterial wall in moyamoya disease. Neurosci Lett. 2015;584:77-82.

11. Underhill HR, Kerwin WS, Hatsukami TS, Yuan C. Automated measurement of mean wall thickness in the common carotid artery by MRI: A comparison to intima-media thickness by B-mode ultrasound. J Magn Reson Imaging. 2006;24:379-387.

12. Antiga L, Wasserman BA, Steinman DA. On the overestimation of early wall thickening at the carotid bulb by black blood MRI, with implications for coronary and vulnerable plaque imaging. Magn Reson Med. 2008;60:1020-1028.

13. Harteveld AA, Denswil NP, Van Hecke W, et al. Ex vivo vessel wall thickness measurements of the human circle of Willis using 7T MRI. Atherosclerosis. 2018;273:106-114.

14. Khan M, Naqvi I, Bansari A, Kamal AK. Intracranial atherosclerotic disease. Stroke Res Treat. 2011;2011:282845.

15. Choi YJ, Jung SC, Lee DH. Vessel Wall Imaging of the Intracranial and Cervical Carotid Arteries. J Stroke. 2015;17:238-255.

16. van der Kolk AG, Zwanenburg JJM, Denswil NP, et al. Imaging the Intracranial Atherosclerotic Vessel Wall Using 7T MRI: Initial Comparison with Histopathology. Am J Neuroradiol. 2015;36:694-701.

17. Tustison NJ, Avants BB, Cook PA, et al. N4ITK: Improved N3 Bias Correction. IEEE Trans Med Imaging. 2010;29:1310-1320.

18. Otsu N. A Threshold Selection Method from Gray-Level Histograms. IEEE Trans Syst Man Cybern. 1979;9:62-66.

19. Botnar RM, Stuber M, Kissinger K V., Kim WY, Spuentrup E, Manning WJ. Noninvasive Coronary Vessel Wall and Plaque Imaging With Magnetic Resonance Imaging. Circulation. 2000;102:2582-2587.

20. Lindenholz A, van der Kolk AG, Zwanenburg JJM, Hendrikse J. The Use and Pitfalls of Intracranial Vessel Wall Imaging: How We Do It. Radiology. 2018;286:12-28.

21. Coolen BF, Calcagno C, van Ooij P, Fayad ZA, Strijkers GJ, Nederveen AJ. Vessel wall characterization using quantitative MRI: what's in a number? Magn Reson Mater Physics, Biol Med. 2018;31:201-222.

22. Donoho DL. Compressed sensing. IEEE Trans Inf Theory. 2006;52:1289-1306.

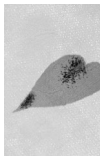

CHAPTER 4

Subvoxel vessel wall thickness measurements of the intracranial arteries using a convolutional neural network

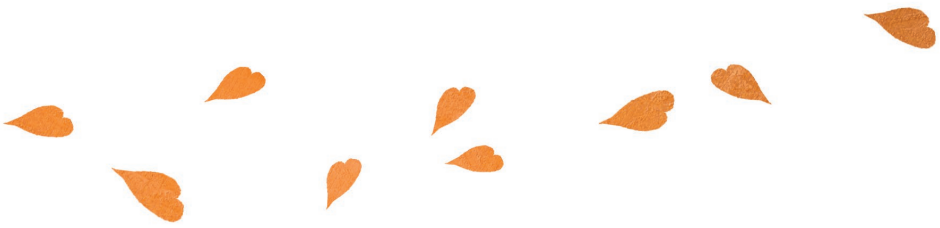

PUBLISHED AS:

MEDICAL IMAGE ANALYSIS. 2021;67:101818.

Kees M. van Hespen, Jaco J.M. Zwanenburg, Jeroen Hendrikse, Hugo J. Kuijf.

Subvoxel vessel wall thickness measurements of the intracranial arteries using a convolutional neural network.

ABSTRACT

PURPOSE

In this study we aimed to accurately estimate the subvoxel vessel walls thickness of the intracranial arteries from vessel wall magnetic resonance (MR) images using a convolutional neural network. Additionally, we test the robustness of our convolutional neural network by applying Monte Carlo dropout and test time augmentation. Lastly, we explore the feasibility of our network on three in vivo images of intracranial aneurysms.

MATERIALS AND METHODS

MR imaging of 34 circle of Willis specimens was performed using a 3D gradient echo (3D T1 TFE) protocol (isotropic acquired voxel size: 0.11 mm) and a clinically-used 3D magnetization preparation inversion recovery turbo spin echo (MPIR-TSE) protocol (isotropic acquired voxel size: 0.8 mm). The true vessel wall thickness was measured from the 3D T1 TFE images for each point on the vessel wall. Image patches were sampled from the MPIR-TSE images, centered around the locations where thickness measurements were performed on the 3D T1 TFE images. These image patches were fed to a convolutional neural network which was trained to estimate the true vessel wall thickness.

RESULTS

The thickness of walls thinner than the voxel size could be accurately estimated by the convolutional neural network. On average the difference between the estimated and true vessel wall thickness was -50 μm with an interquartile range of 120 μm. Our network is relatively robust to changes to the input and the model, given the comparable mean squared errors between the original network and the test time augmentation and test time dropout networks (0.016 vs 0.013 vs 0.023). Measurements on the in vivo images of an aneurysm showed realistic wall thicknesses, ranging from 0.3 mm for thin areas, to 1.2 mm for a focal thickening in two patients.

CONCLUSION

Our trained convolutional neural network has shown resolvability of different vessel wall thicknesses, well below the acquired voxel size. The methods described may facilitate quantitative measurements on MRI data for a wider range of clinical applications.

INTRODUCTION

Intracranial vessel wall thickening is commonly seen as biomarker for cerebrovascular disease and atherosclerotic plaque formation.[1–4] In several recent studies, vessel wall magnetic resonance imaging (MRI) has been used to quantify the intracranial vessel wall thickness.[5–11] However, for accurate thickness measurements using conventional measurement methods, vessel walls need to be at least 1.5 to 2 voxels wide.[12,13] Current acquisitions do not abide this rule, as clinically feasible MR voxel sizes (0.5–0.8 mm),[10,14] are still considerably larger than the average vessel wall thickness (0.25–0.45 mm).[15] Further increasing the acquired spatial resolution has considerable detrimental effects on accurate thickness measurements, because of an increase in scan time and reduction of signal-to-noise ratio (SNR). These changes would cause higher noise levels and possibly additional motion artifacts, nullifying the resolving power gained by the increased spatial resolution.

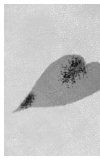

Several image processing strategies have been employed to compensate for this lack of resolving power. In computed tomography (CT) acquisitions, thickness measurements of the airways were corrected by geometric modeling and modeling of the airway wall intensity distribution.[16–18] Kok et al.[19] employed a modeling strategy for necrotic core cap thickness measurements in the carotid arteries. Furthermore, a study by Kleinloog et al.[20] showed that the aneurysm vessel wall thickness correlates with vessel wall image intensity, which was used in a later study to obtain semi-quantitative vessel wall thickness measurements.[21] Clearly, intensity distribution, shape, and orientation hold information that can contribute to more accurate measurements, even for walls with a thickness smaller than the voxel size.

Convolutional neural networks have proven to learn these image features for solving various image processing tasks, oftentimes outperforming classical machine learning algorithms, trained on handcrafted image features.[22] We hypothesize that a convolutional neural network can also be applied to vessel wall MR images, where it can learn relevant image features that can contribute to accurate vessel wall thickness measurements.

The goal of this study was to improve the accuracy of subvoxel vessel wall thickness measurements from vessel wall MR images, by implementing a convolutional neural network algorithm that is trained on acquisitions of ex vivo specimen data featuring validated ground truth thickness measurements. In addition, we demonstrate the feasibility of a convolutional neural network in vivo in three subjects with an intracranial aneurysm.

MATERIALS AND METHODS

SPECIMEN DATA

In this retrospective, institutional review board approved study, 34 post-mortem human circle of Willis specimens were used.[23] The specimens were collected between 2008 and 2017, and originated from patients with a mean age of 69 years (range: 53–87 years). All specimens were stored in buffered formalin (4%) before being embedded on a petri dish in 2% agarose solution.

MR ACQUISITION

Imaging was performed at room temperature on a 7T human platform (Philips, Best, The Netherlands). A volume transmit coil was used (Nova Medical, Wilmington, MA, USA), and for receiving, a custom-made high-density coil (16 channels per 70 cm^2, MR Coils, Zaltbommel, The Netherlands) was used. The specimens were imaged two at a time, with the receive coils placed above and below the specimens.

Two MR acquisitions were performed. First, an ultra-high-resolution image was acquired using a 3D turbo field echo (3D T1 TFE) sequence (acquired resolution: 0.11x0.11x0.11 mm^3), see Table 1. Second, a clinically-used 3D magnetization preparation inversion recovery turbo spin echo (MPIR-TSE[14,24]) was used (acquired resolution: 0.8x0.8x0.8 mm^3) to acquire 'clinical-resolution' images. Example images for both acquisitions are given in Figure 1.

Table 1. MR acquisition parameters.

	3D T1 TFE	MPIR-TSE
Acquisition duration, h:min:s	5:45:47	0:08:35
Repetition time, ms	55	1700
Echo time, ms	6.1	37
Inversion time, ms	-	650
Acquisition matrix	864 x 1182	188 x 186
Field of view, mm	95 x 130 x 35	150 x 150 x 40
No. averages	1	2
Acq. voxel size, mm^3	0.11 x 0.11 x 0.11	0.8 x 0.8 x 0.8
Rec. voxel size, mm^3	0.11 x 0.11 x 0.11	0.47 x 0.47 x 0.4

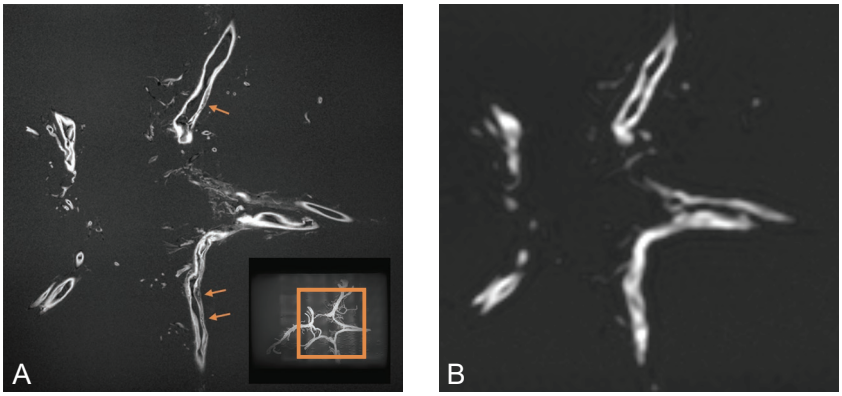

Figure 1. MR images of a circle of Willis specimen. Images were acquired with the (A) Ultra-high-resolution and (B) clinically-used scan protocol. The inset in A shows a maximum intensity projection to provide an overview of the circle of Willis specimen. The orange arrows denote locations of wall thickening.

IMAGE PREPROCESSING

After acquisition, N4 bias field correction was applied to all images.[25] The vessel walls and background were segmented using thresholding based on Otsu's method.[26] Hereafter, all images were normalized, where the 95th percentile intensity of the vessel wall and median background intensities were scaled to 1 and 0, respectively.

GROUND TRUTH THICKNESS MEASUREMENTS

Ground truth thickness measurements were performed on the ultra-high-resolution images. These ground truth thickness measurements were used as target measurements for the convolutional neural network to train towards. For these measurements a processing pipeline was created in MeVisLab 3.1 (Fraunhofer Mevis, Germany[27]), consisting of several steps. First, the center line of the vessel lumen was tracked using the Euclidean distance transform for the largest arteries of the circle of Willis (Figure 2A). Second, a multi planar reconstruction (MPR) was created along the vessel lumen center line. For each image slice in the MPR, an isocontour was automatically drawn at the inner and outer wall boundary at the full-width-at-half-maximum intensity value (Figure 2B). Isocontours were manually inspected on accuracy, and manually corrected where needed. Third, a skeleton of the vessel wall was calculated using the 2D distance transform (Figure 2B, given in red). For each skeleton point, the ground truth thickness was measured as the shortest distance between the inner and outer contour through the skeleton point.

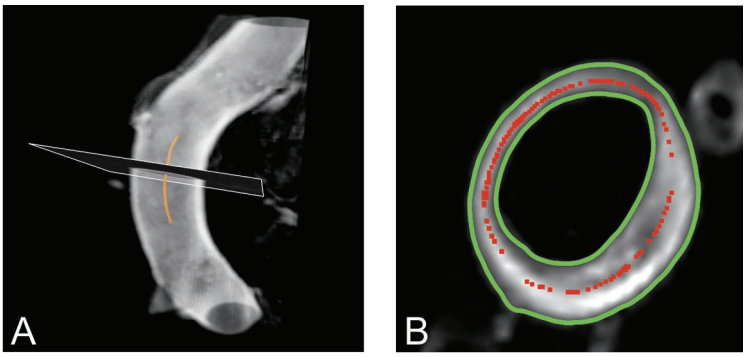

Figure 2. Tracked center line and isocontour generation. (A) 3D rendered vessel wall, with tracked center line given in orange. The location of the MPR slice in (B) is indicated by the white plane in (A). (B) MPR slice, with automatically generated inner and outer wall contours shown in green. Generated skeleton points are given in red. For each skeleton point, the local thickness is calculated as the shortest distance between inner and outer contour.

SPECIMEN ASSIGNMENT

Because of the small number of specimens, three data folds were created. Assignment of the specimens to these folds was done purposive, since the number of specimens with walls thicker than 0.8 mm were scarce. The specimens were ranked on the number of measurement locations with a ground truth thickness larger than 0.8 mm. For the first fold, each third specimen was assigned to the test set, starting from the first specimen. For the other two folds, starting from the second and third specimen, each third specimen was assigned to the test set. The remaining specimens per fold were used for training and validation. In total, 11 or 12 specimens per specimen assignment fold were assigned to the test set. The assignment of the remaining specimens to the training and validation sets was performed randomly and was kept at a ratio of 2:1.

PATCH SAMPLING

The neural network was trained to estimate the ground truth thickness from image patches sampled from the clinical-resolution images. These image patches were sampled with a size of 19x19x19 voxels (isotropic sampled voxel grid size: 0.4 mm), centered around the locations of the ground truth thickness measurements. For the training set, image patches were sampled uniformly across the range of ground truth thickness values (0.25–1.4 mm). For data augmentation, image patches were sampled at random orientations to the original image voxel grid. For the validation and test set, all measured

locations were sampled parallel to the original image voxel grid. A total of 300.000 image patches were created for the training set. The number of patches for the validation and test set were roughly in the order of 10.000–30.000, depending on the specimen assignment fold and network instance. Example patches are given in Figure 3B, along with the corresponding ultra-high-resolution locations in Figure 3B.

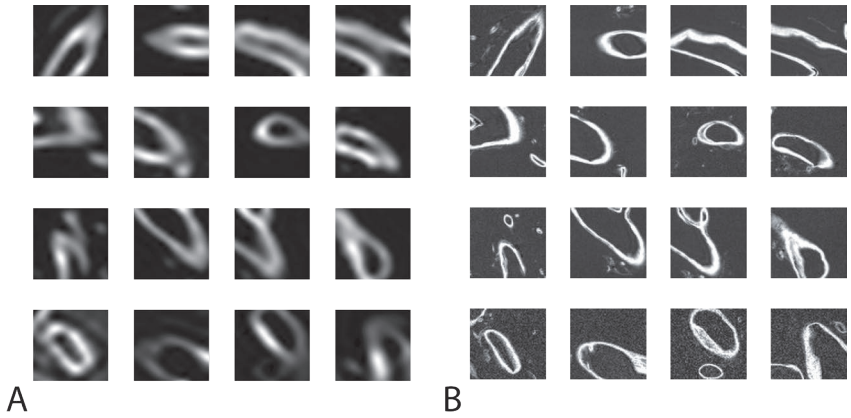

Figure 3. Example patches fed to the neural network. (A) Middle slice of 16 example patches (of 19x19x19 voxels). (B) Corresponding locations in the ultra-high-resolution images.

NETWORK TRAINING

In total, ten instances of the neural network were trained per fold on the GPU of a standard workstation (Intel Xeon E5-1620v3, 32gb RAM, Nvidia Titan Xp). For training of the neural network, a learning rate of 1E-5 was used. In each instance, the assignment of the specimens to the training and validation sets was randomly changed, but was kept at a ratio of 2:1. Training of each network instance was ceased if the validation error did not decrease over 80 epochs. The network instance with the lowest validation error was applied to the test set per fold.

ARCHITECTURE

Our convolutional neural network architecture, implemented in Lasagne 0.2dev128 and Theano,[29] is given in Figure 4. The image patches were fed to the network in minibatches of size 16 to two parallel paths, each consisting of five convolutional layers and a fully connected layer. Each path featured different kernel sizes and kernel count, allowing for varying receptive field sizes (see color coding in Figure 4). The fully connected layers of both pathways were concatenated, and were followed by an additional fully connected layer.

This layer fed into the linearly activated output layer. All other layers were activated by a parametric rectified linear unit (pReLu).

For regularization purposes, all but the last fully connected layer featured dropout (p = 0.5). Each convolutional layer was followed by pReLu activation and batch normalization. The mean squared error between estimated and ground truth thickness was used as error metric, and Adam was used as optimizer.[30]

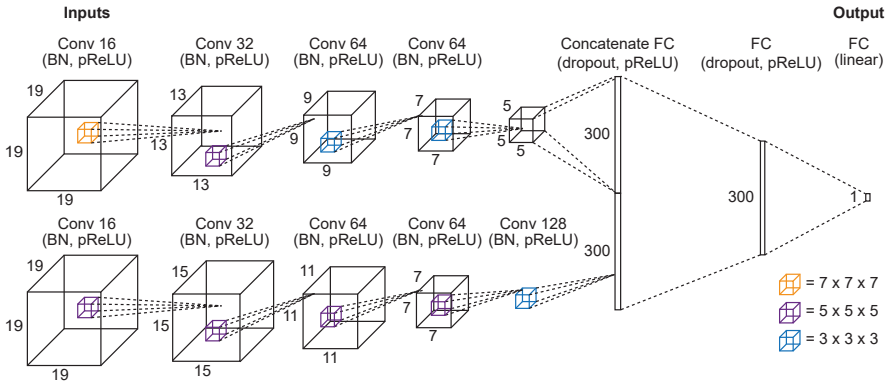

Figure 4. Convolutional neural network architecture, with two input paths. Each convolutional (conv) layer is followed by batch normalization (BN) and activation using the parametric Rectified Linear unit (pReLu). The convolutional kernel size per layer is given by the color-coded squares in the legend. Each path is followed by a fully connected (FC) layer, which is concatenated. An additional FC layer feeds into the linearly activated output layer. P = 0.5 is used for the dropout layers.

EXPERIMENTS

LOW-TECH THICKNESS MEASUREMENTS

A low-tech approach as measure for the vessel wall thickness is to use the image intensity as a proxy. We investigated the limitations of such an approach, and investigated the direct relationship between the ground truth thickness measurements, and the image intensity at the locations of the skeleton points in the clinical-resolution images.

SPECIMEN DATA

The network performance on unseen data, was evaluated using the test set. The output of the network was compared to the ground truth thickness, per image patch. The median and interquartile range of the estimated vessel wall thickness was calculated and reported, for twenty bins across the entire range of ground truth thickness values (0.25–1.4 mm). Additionally, we inspected

the kernels trained in the first layer of the network, to gain understanding of the image features that are extracted in this layer.

IMAGE NORMALIZATION

We investigated the effect of the image threshold, which was used for the normalization of the images, on the estimated vessel wall thickness. Hereto, we changed the Otsu's threshold intensity values of the test set images of fold 1 by -10%, -5%, 5%, and 10% of the original threshold intensity values. After image normalization using the new threshold values, image patches were sampled, which were subsequently evaluated by the network. We reported the mean change in estimated thickness and its standard deviation, compared to the vessel wall thickness estimated from the original normalized test set images.

UNCERTAINTY ESTIMATION

To predict the aleatoric and epistemic uncertainty of the neural network on the estimated vessel wall thickness, we respectively applied test time augmentation[31] and Monte Carlo dropout.[32–34] For test time augmentation, the test set of fold 1 was augmented by sampling at random grid orientations, similar to the training set. Hundred passes of the augmented test set through the trained network were performed. For each pass, the sampling grid was randomly oriented. For Monte Carlo dropout, dropout was applied while evaluating the test set of fold 1, as was the case for the training set. In this experiment, the test set was passed a hundred times through the trained network. For both the test time augmentation and the Monte Carlo dropout experiment, we evaluated the performance of the network, by taking the mean estimated thickness per measurement location. The standard deviation of the measurements, per location, were taken as the aleatoric and epistemic uncertainties of the model.

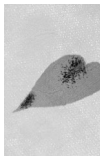

HUMAN SUBJECTS

We also explored the performance of the trained neural network output in an in vivo setting. Hereto, the trained network with the lowest validation error on fold 1, was applied to estimate the vessel wall thickness of aneurysms of the middle cerebral artery of three patients, who were scanned as part of a previous study.[20] After bias field correction, the brain tissue surrounding the aneurysm wall was manually stripped. Image patches were sampled centered around manually selected locations where the vessel wall was not touching the surrounding brain tissue.

RESULTS

LOW-TECH THICKNESS MEASUREMENTS

As a low-tech thickness measurement, we investigated how the image intensity in clinical-resolution image is related to the ground truth thickness measurement. The image intensity is roughly linearly related to the ground truth thickness (Figure 5), up to around the voxel size. Image intensities for walls above the voxel size are similar, yielding no distinguishability between vessel walls in this thickness range.

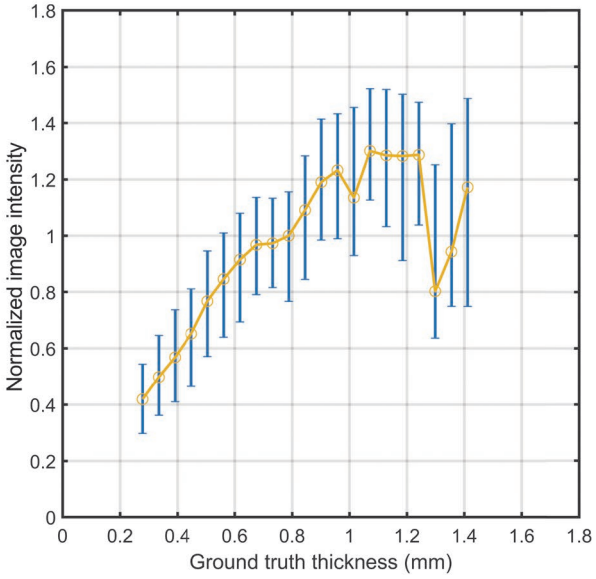

Figure 5. Ground truth thickness against the normalized image intensity in the clinical-resolution images. Yellow circles denote the median intensity, with the blue bars representing the interquartile range.

SPECIMEN DATA

The convolutional neural network was trained for roughly 16 hours per network instance before the early stopping criterion was met. The trained kernels of the first layer in both paths of the network were inspected (Figure 6). This figure shows that some of the kernels of the first layer were trained to highlight edges, and enhance the foreground/background. Hereafter, the trained network was applied to the test set image patches, of which in 97%, 98%, and 98% of the patches, the ground truth thickness was smaller than the acquired voxel size for fold 1, 2, and 3, respectively (purple lines in Figure 7).

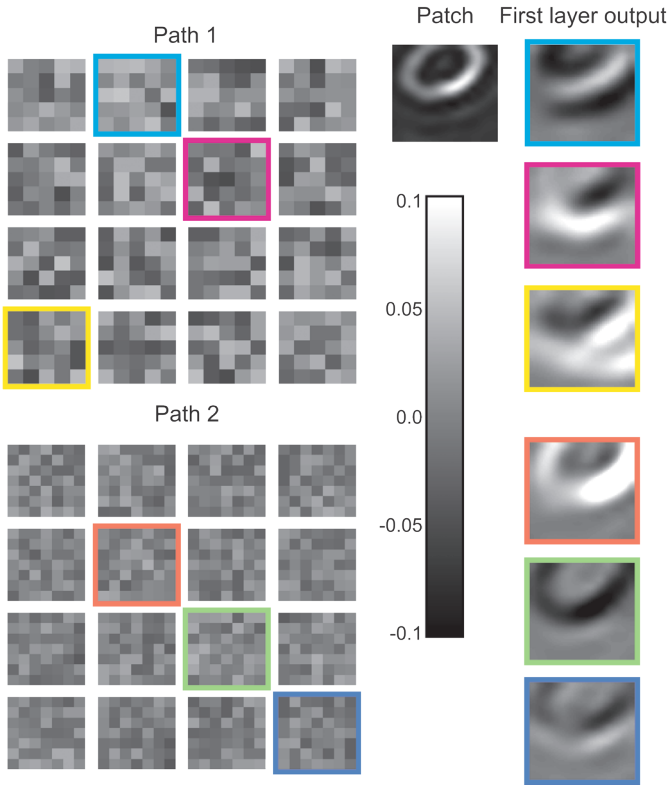

Figure 6. Middle slice of the 3D kernels in the first layer of the network, for both paths. The colorbar belongs to the kernels. As an example, the highlighted kernels were applied to the patch. The kernels of the first path, seem to focus on edge enhancement. The kernels of the second path seem to focus on intensity inversion and enhancement of the wall.

Vessel walls with a thickness in the subvoxel range could be accurately estimated by the trained convolutional neural network (Figure 7). In this subvoxel range, the vessel wall thickness was on average slightly underestimated by the trained convolutional neural network for fold 1 (median difference: -50 μm, interquartile range: 120 μm) and overestimated for folds 2 and 3 (fold 2: median difference: 39 μm, interquartile range: 97 μm. fold 3: median difference: 57 μm, interquartile range: 99 μm). Above the voxel size, the number of measurements were scarce, as can be observed from the purple lines in Figure 7. The locations with a vessel wall thickness above 0.8 mm were on average underestimated, with a median difference of -140 μm and interquartile range of 170 μm for fold 1, and with a median difference of -139 μm and -85 μm and interquartile range of 176 μm and 303 μm for folds 2 and 3, respectively.

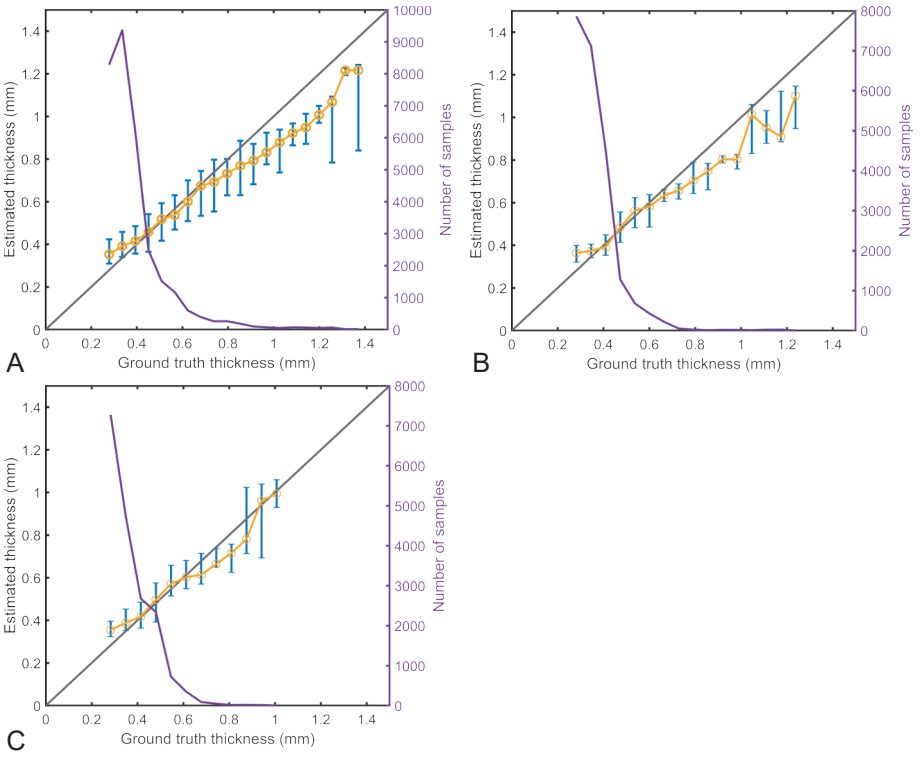

Figure 7. Ground truth thickness against thickness estimated by the neural network for all three specimen assignment folds. (A) fold 1, (B) fold 2, and (C) fold 3. Yellow circles denote the median estimated thickness, with the blue bars representing the interquartile range. Ideally the estimated thickness lies along the $y = x$ line given in gray. The number of samples per ground truth thickness is given by the purple line. The number of samples in the test set where the ground truth thickness is smaller than 0.6 mm, is larger than the number of samples with a thickness above.

IMAGE NORMALIZATION

When changing the image threshold that was used to normalize the vessel wall images, a small change in estimated vessel wall thickness was observed. On average, the change in estimated thickness was 1.08 ± 1.04%, 0.52 ± 0.50%, -0.49 ± 0.51%, and -0.94 ± 0.89%, when changing the threshold used to normalize the vessel wall images by -10%, -5%, 5%, and 10%, respectively.

UNCERTAINTY ESTIMATION

Taking the median of the output of 100 test time augmentation passes over the entire test set of fold 1 yielded comparable results to the originally trained convolutional neural network (Figure 8A). Moreover, a decrease in mean squared error was observed (0.013 vs 0.016). On average, the model uncertainty for each measurement location was 45 μm (Figure 8B).

Monte Carlo dropout resulted in slightly more inaccurate measurements, given the larger interquartile ranges (Figure 9A), and increase in the mean squared error compared to the originally trained convolutional neural network (0.023 vs 0.016). However, the median estimated thickness of the 100 Monte Carlo dropout passes was closer to the line, than in the original and test time augmentation experiments. The average uncertainty for each measurement was 52 μm.

Vessel walls where the thickness was largely overestimated/underestimated had a large estimated uncertainty. Walls where the thickness was more accurately measured also had a lower estimated uncertainty.

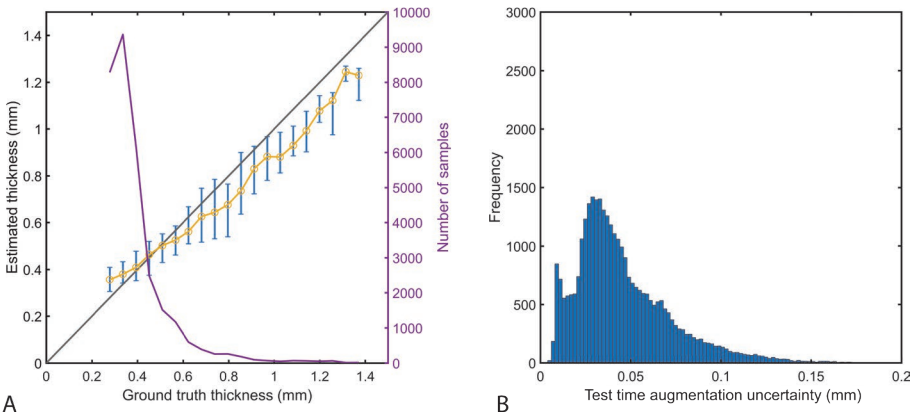

Figure 8. Test time augmentation results. (A) Ground truth thickness against the mean vessel wall thickness computed for 100 test set passes using test time augmentation. Yellow circles denote the median estimated thickness, with the blue bars representing the interquartile range. (B), the distribution of the standard deviation for all test patches.

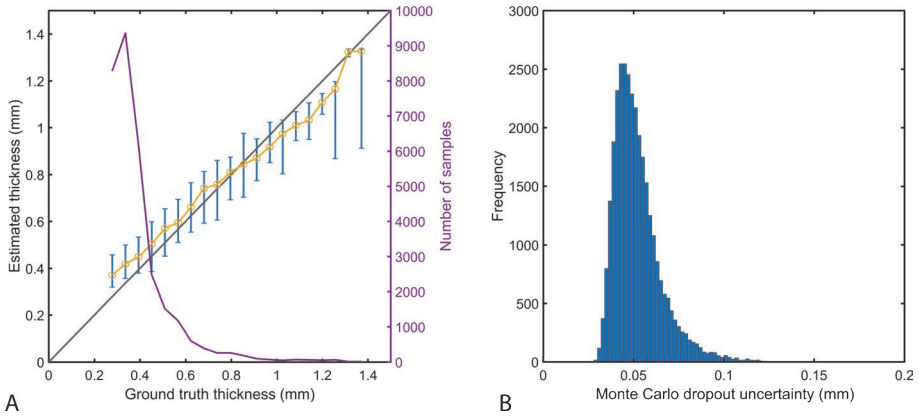

Figure 9. Monte Carlo dropout results. (A) Ground truth thickness against the mean vessel wall thickness computed from 100 test set passes using Monte Carlo dropout. Yellow circles denote the median estimated thickness, with the blue bars representing the interquartile range. B), the distribution of the standard deviation for all test patches.

HUMAN SUBJECTS

The convolutional neural network, trained on the specimen data of fold 1, was applied to in vivo vessel wall MR images of intracranial aneurysms. The intracranial aneurysms observed in Figure 10B and 10D showed a focal thickening where the vessel wall thickness was estimated at around 1.2 mm. The thinner parts of the aneurysm wall and the aneurysm wall in Figure 10F were estimated at a thickness of 0.3 mm. We could not perform measurements across the entire aneurysm wall, since at several locations the wall was visually indistinguishable from the surrounding brain tissue.

DISCUSSION

In this paper, we aimed to improve the accuracy of vessel wall thickness measurements using a convolutional neural network implementation. Using our implementation, walls thinner than the voxel size could be accurately measured. On average the difference between the estimated and ground truth thickness was -50, 39, and 57 μm with an interquartile range of 120, 97, and 99 μm, for each of three specimen assignment folds, respectively. We also observed that the normalization of the vessel wall images, performed during image preprocessing, had a minimal effect up to on average 1% in the estimated vessel wall thickness. Additional to the training and testing on specimen data, we tested the feasibility of our method on three in vivo

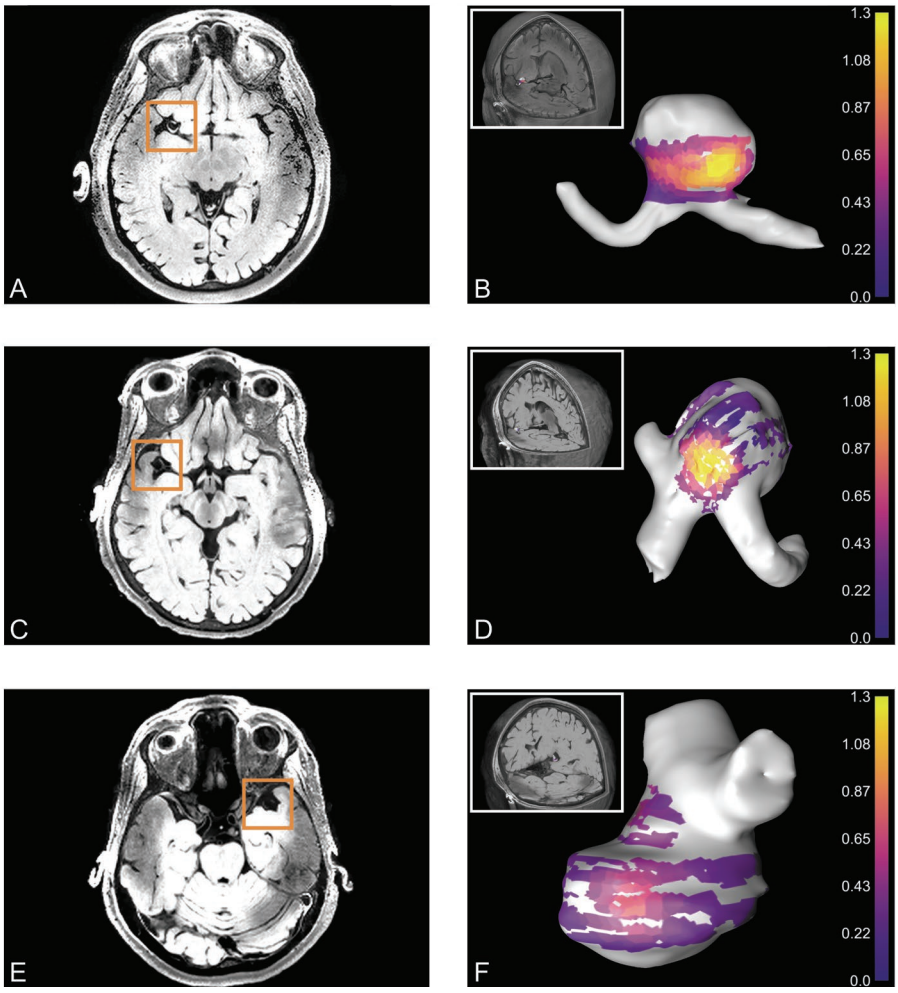

Figure 10. Thickness measurements on in vivo aneurysms of the middle cerebral artery of three patients. (A, C, and E) Transversal slice of vessel wall image, with the aneurysm located in the orange box. (B, D, and F) Inset: Posterior view of the brain, with an intracranial aneurysm of the middle cerebral artery. 3D rendering of the estimated thickness is given over the surface of the aneurysm. The thickness is given in millimeters.

acquisitions of intracranial aneurysms. The estimated vessel wall thickness values for the aneurysm were similar to the thickness values reported by Kleinloog et al.[20]

The resolution of currently available vessel wall MR acquisitions (0.5–0.8 mm isotropic) limits the accuracy of measurements on the intracranial vessel wall thickness.[12] Pushing the spatial resolution of these acquisitions

upwards strains the total scan time. For perfectly accurate measurements of the thinnest walls, the theoretically required voxel size would be 0.125 mm isotropic.[35] This decrease in voxel volume corresponds to an increase in scan time by a factor of 16 to 41, relative to the scan time of acquisitions with voxel sizes of 0.5 to 0.8 mm, respectively. Simultaneously, the SNR would decrease by similar factors. Scanning at higher field strengths may increase SNR and techniques such as compressed sensing could be used to decrease scan time. However, the required gains in SNR and scan time will likely not be feasible in the foreseeable future.

A proxy for the vessel wall thickness is the image intensity of the vessel wall. Our results have shown that for vessel walls with a thickness up to the voxel size, the image intensity increased relatively linearly (Figure 5). However, a major downside of such a low-tech solution is that measurements are not quantitative. Without validated measurements, it is unknown beforehand how the image intensities directly relate to the vessel wall thickness. Only for the visualization of relative differences in vessel wall thicknesses, such a low-tech method may suffice. Our proposed method does not suffer from this downside, because it uses more image features than solely the image intensity, and its output is quantitative by design.

Our method shows similarities to super-resolution, where the goal is also to resolve objects that are smaller than the acquired voxel size.[36,37] In super-resolution, neural networks are employed to reconstruct high-resolution images from lower-resolution images. This method could also be used for vessel wall thickness measurements. Reconstructing higher resolution image patches, and subsequently performing thickness measurements on these reconstructions can possibly yield similar results to our method. However, our implementation allowed for direct inference of the vessel wall thickness from clinical-resolution patches, without additional post-processing steps. The method may facilitate quantitative measurements on medical imaging data for a wider range of clinical applications. Using a transfer learning approach, the model could potentially be retrained on estimating the vessel wall thickness of the bronchi from CT images.[38]

In comparison to conventional thickness measurement methods, our approach has the advantage that it was trained on validated ground truth thickness measurements. Conventional measurement methods are often times not validated, and therefore have unknown measurement accuracy. Moreover,

our method uses three-dimensional spatial information to estimate the local vessel wall thickness. Only a few conventional methods use 3D spatial information, whereas most methods use 2D spatial information to delineate the lumen and outer wall contours.[7,9,39–41]

This study has shown that image resolution is not necessarily a limiting factor in resolving subvoxel vessel wall thicknesses. Additional image features can be used to achieve accurate thickness measurements. However, training the model on images acquired with a higher spatial resolution, will likely yield more accurate and precise measurements, as more information is retained in these images. As more recent vessel wall acquisitions have acquired voxel sizes as low as 0.5 mm, the performance of our model can potentially be increased even more.[42]

In previous work,[23] we have shown that also from downsampled high-resolution images the vessel wall thickness can be accurately estimated by the neural network, albeit with a lower performance and different neural network architecture. This suggests that the acquisition parameters used to acquire the MR images are learned to a certain degree by the network. The remaining discrepancy between the ground truth thickness measurements and the estimation by the neural network is likely caused by the availability of thick vessel walls. Increasing the amount of data in this higher thickness range will likely improve the proportionality between the ground truth thickness measurements and estimations by the neural network.

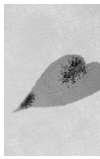

Our method has shown to be relatively robust to changes to the input and the model. Firstly, the output was robust to rotational variation of the input. When rotations were applied to the input image patch, the standard deviation on thickness measurements was on average 45 μm. This rotational invariance of the model was likely learned during the training phase, where augmented data was already presented. Secondly, using dropout on the fully connected layers, has shown that the thickness can be accurately estimated even though half of the connections were dropped (average standard deviation measurement: [52] μm). This indicates that the model can generalize well to the problem. The dropped connections do not have a large impact on the estimated thickness, but only help fine-tune the estimated thickness. Measurement locations that show a large uncertainty in the estimated thickness can potentially be further analyzed, or they can be excluded from the output thickness map, since their estimated is likely to be more severely over/underestimated.

In future work, other network architectures can be explored, that may achieve even better results. Our network featured a double entry parallel path, with the hypothesis that this may facilitate different initial receptive field sizes for larger and smaller vessels. The use of dilated convolutional kernels with a single downward path could potentially achieve similar results. Additionally, the translation to in vivo applications should be further explored. In a larger study where, in vivo and ex vivo data is available, the effects of for example patient motion can be examined and compensated for. Additional verification can be performed in animal models, where both in vivo and ex vivo imaging is possible, or in humans where both in vivo MR image data as well as obduction material is available. Furthermore, automated sampling strategies can be designed for in vivo images, where for example time of flight magnetic resonance angiograms are used for the detection of the vessel wall.

This study has several limitations. Firstly, the network was trained on ex vivo data, which does not directly translate to in vivo acquisitions. However, this approach allowed performing validated ground truth thickness measurements. Furthermore, our in vivo example showed that it is likely that our method performs well on in vivo acquisitions. Secondly, the model was trained on image patches where the wall was separate from adjacent structures. In an in vivo setting, the vessel wall may be touching the surrounding brain tissue. This could have an impact on the estimated thickness. Only walls that do not clearly touch the surrounding tissue should be fed to the neural network. This is for example the case for the basilar artery, where the ventral part of the artery is not touching brain parenchymal tissue and is one of the most prevalent locations of atherosclerotic plaque growth.[43] Additionally, since MR acquisitions and scanner hardware are ever improving in image resolution, and CSF and blood suppression, application of our method on these vascular regions will be feasible. Thirdly, we are limited by our selection of specimens. Not all of the specimens contained very thick walls, since the cause of death for each patient was not always related to cerebrovascular disease. Inclusion of specimens from patients who suffered from cerebrovascular disease would likely yield more thickened walls. Due to the imbalance in available thick walls, the validation and test set results are likely more heavily influenced by the thinner walls. However, for accurate measurements on early wall thickening this is the most important range. Fourthly, the clinical application of this method is likely limited in vessel walls with severe calcification deposits. The hypointense signal of calcifications will likely lead to an underestimation of the vessel wall thickness, because the hypointense plaque

could be accounted to the lumen as opposed to the vessel wall. However, for the vessel walls in our dataset which featured (early) atherosclerotic plaque formation, accurate vessel wall thickness measurements were still possible using our proposed method. Future studies should include vessel wall data with severe calcifications to investigate this effect.

To conclude, our convolutional neural network implementation has shown that accurate vessel wall thickness measurements are possible for walls with a thickness well below the acquired voxel size.

ACKNOWLEDGMENTS

We acknowledge Prof. G.J.E. Rinkel for providing the vessel wall MR images of the three patients with an intracranial aneurysm.

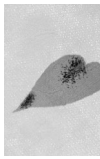

REFERENCES

1. de Groot E. Measurement of Arterial Wall Thickness as a Surrogate Marker for Atherosclerosis. Circulation. 2004;109:III-33-III-38.

2. Burke GL, Evans GW, Riley WA, et al. Arterial Wall Thickness Is Associated With Prevalent Cardiovascular Disease in Middle-Aged Adults. Stroke. 1995;26:386-391.

3. Nakashima Y, Wight TN, Sueishi K. Early atherosclerosis in humans: Role of diffuse intimal thickening and extracellular matrix proteoglycans. Cardiovasc Res. 2008;79:14-23.

4. Kolodgie FD, Burke AP, Nakazawa G, Virmani R. Is pathologic intimal thickening the key to understanding early plaque progression in human atherosclerotic disease? Arterioscler Thromb Vasc Biol. 2007;27:986-989.

5. Sherif C, Kleinpeter G, Mach G, et al. Evaluation of cerebral aneurysm wall thickness in experimental aneurysms: Comparison of 3T-MR imaging with direct microscopic measurements. Acta Neurochir (Wien). 2014;156:27-34.

6. Zhang N, Zhang F, Deng Z, et al. 3D whole-brain vessel wall cardiovascular magnetic resonance imaging : a study on the reliability in the quantification of intracranial vessel dimensions. J Cardiovasc Magn Reson. 2018;20:39.

7. Park JK, Lee S, Sim KB, Huh JS, Park JC. Imaging of the walls of saccular cerebral aneurysms with double inversion recovery black-blood sequence. J Magn Reson Imaging. 2009;30:1179-1183.

8. Ryu CW, Jahng GH, Kim EJ, Choi WS, Yang DM. High resolution wall and lumen MRI of the middle cerebral arteries at 3 tesla. Cerebrovasc Dis. 2009;27:433-442.

9. Underhill HR, Kerwin WS, Hatsukami TS, Yuan C. Automated measurement of mean wall thickness in the common carotid artery by MRI: A comparison to intima-media thickness by B-mode ultrasound. J Magn Reson Imaging. 2006;24:379-387.

10. Qiao Y, Guallar E, Suri FK, et al. MR Imaging Measures of Intracranial Atherosclerosis in a Population-based Study. Radiology. 2016;280:860-868.

11. Qiao Y, Steinman DA, Qin Q, et al. Intracranial arterial wall imaging using three-dimensional high isotropic resolution black blood MRI at 3.0 Tesla. J Magn Reson Imaging. 2011;34:22-30.

12. Antiga L, Wasserman BA, Steinman DA. On the overestimation of early wall thickening at the carotid bulb by black blood MRI, with implications for coronary and vulnerable plaque imaging. Magn Reson Med. 2008;60:1020-1028.

13. van Hespen KM, Zwanenburg JJM, Harteveld AA, Luijten PR, Hendrikse J, Kuijf HJ. Intracranial Vessel Wall Magnetic Resonance Imaging Does Not Allow for Accurate and Precise Wall Thickness Measurements. Stroke. 2019;50.

14. van der Kolk AG, Zwanenburg JJM, Brundel M, et al. Intracranial Vessel Wall Imaging at 7.0-T MRI. Stroke. 2011;42:2478-2484.

15. Harteveld AA, Denswil NP, Van Hecke W, et al. Ex vivo vessel wall thickness measurements of the human circle of Willis using 7T MRI. Atherosclerosis. 2018;273:106-114.

16. Estépar RSJ, Washko GG, Silverman EK, Reilly JJ, Kikinis R, Westin C-F. Accurate Airway Wall Estimation Using Phase Congruency. In: Larsen R, Nielsen M, Sporring J, eds. Medical Image Computing and Computer-Assisted Intervention – MICCAI 2006. Vol 4191. Berlin, Heidelberg: Springer; 2006:125-134.

17. Cho YH, Seo JB, Kim N, et al. Comparison of a new integral-based half-band method for CT measurement of peripheral airways in COPD with a conventional full-width half-maximum method using both phantom and clinical CT images. J Comput Assist Tomogr. 2015;39:428-436.

18. Saba OI, Hoffman EA, Reinhardt JM. Maximizing quantitative accuracy of lung airway lumen and wall measures obtained from X-ray CT imaging. J Appl Physiol. 2003;95:1063-1075.

19. Kok AM, van der Lugt A, Verhagen HJM, van der Steen AFW, Wentzel JJ, Gijsen FJH. Model-based cap thickness and peak cap stress prediction for carotid MRI. J Biomech. 2017;60:175-180.

20. Kleinloog R, Korkmaz E, Zwanenburg JJM, et al. Visualization of the aneurysm wall: A 7.0-Tesla magnetic resonance imaging study. Neurosurgery. 2014;75:614-622.

21. Blankena R, Kleinloog R, Verweij BH, et al. Thinner Regions of Intracranial Aneurysm Wall Correlate with Regions of Higher Wall Shear Stress: A 7T MRI Study. Am J Neuroradiol. 2016;37:1310-1317.

22. Litjens G, Kooi T, Bejnordi BE, et al. A survey on deep learning in medical image analysis. Med Image Anal. 2017;42:60-88.

23. van Hespen KM, Zwanenburg JJM, Hendrikse J, Kuijf HJ. Subvoxel vessel wall thickness measurements from vessel wall MR images. In: Angelini ED, Landman BA, eds. Medical Imaging 2019: Image Processing. Vol 10949-69. SPIE; 2019:69.

24. van der Kolk AG, Hendrikse J, Brundel M, et al. Multi-sequence whole-brain intracranial vessel wall imaging at 7.0 tesla. Eur Radiol. 2013;23:2996-3004.

25. Tustison NJ, Avants BB, Cook PA, et al. N4ITK: Improved N3 Bias Correction. IEEE Trans Med Imaging. 2010;29:1310-1320.

26. Otsu N. A Threshold Selection Method from Gray-Level Histograms. IEEE Trans Syst Man Cybern. 1979;9:62-66.

27. Ritter F, Boskamp T, Homeyer A, et al. Medical Image Analysis. IEEE Pulse. 2011;2:60-70.

28. Dieleman S, Schlüter J, Raffel C, et al. Lasagne: First release. August 2015. Available at: https://zenodo.org/record/27878. Accessed May 13, 2020.

29. The Theano Development Team, Al-Rfou R, Alain G, et al. Theano: A Python Framework for Fast Computation of Mathematical Expressions.; 2016. Available at: http://arxiv.org/abs/1605.02688. Accessed May 13, 2020.

30. Kingma DP, Ba J. Adam: A Method for Stochastic Optimization. In: Lehman J, Stanley KO, eds. Proceedings of the 12th Annual Conference on Genetic and Evolutionary Computation. New York: ACM Press; 2014:103-110.

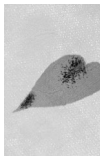

31. Wang G, Li W, Ourselin S, Vercauteren T. Automatic Brain Tumor Segmentation Using Convolutional Neural Networks with Test-Time Augmentation. In: Crimi A, Bakas S, Kuijf H, Keyvan F, Reyes M, van Walsum T, eds. Brainlesion: Glioma, Multiple Sclerosis, Stroke and Traumatic Brain Injuries. Springer, Cham; 2019:61-72.

32. Gal Y, Ghahramani Z. Dropout as a Bayesian Approximation: Representing Model Uncertainty in Deep Learning.; 2015. Available at: http://arxiv.org/abs/1506.02142. Accessed April 2, 2019.

33. Kendall A, Cipolla R. Modelling Uncertainty in Deep Learning for Camera Relocalization.; 2015. Available at: http://arxiv.org/abs/1509.05909v2. Accessed April 4, 2019.

34. Wang G, Li W, Aertsen M, Deprest J, Ourselin S, Vercauteren T. Aleatoric uncertainty estimation with test-time augmentation for medical image segmentation with convolutional neural networks. Neurocomputing. 2019;338:34-45.

35. Nyquist H. Certain Topics in Telegraph Transmission Theory. Trans Am Inst Electr Eng. 1928;47:617-644.

36. Chaudhari AS, Fang Z, Kogan F, et al. Super-resolution musculoskeletal MRI using deep learning. Magn Reson Med. 2018;80:2139-2154.

37. Van Reeth E, Tham IWK, Tan CH, Poh CL. Super-resolution in magnetic resonance imaging: A review. Concepts Magn Reson Part A. 2012;40A:306-325.

38. Zhou Z, Shin J, Feng R, Hurst RT, Kendall CB, Liang J. Integrating Active Learning and Transfer Learning for Carotid Intima-Media Thickness Video Interpretation. J Digit Imaging. 2019;32:290-299.

39. Yuan M, Liu Z, Wang Z, Li B, Xu L, Xiao X. High-resolution MR imaging of the arterial wall in moyamoya disease. Neurosci Lett. 2015;584:77-82.

40. Suinesiaputra A, de Koning PJH, Zudilova-Seinstra E, Reiber JHC, van der Geest RJ. Automated quantification of carotid artery stenosis on contrast-enhanced MRA data using a deformable vascular tube model. Int J Cardiovasc Imaging. 2012;28:1513-1524.

41. Cogswell PM, Lants SK, Davis LT, Donahue MJ. Vessel wall and lumen characteristics with age in healthy participants using 3T intracranial vessel wall magnetic resonance imaging. J Magn Reson Imaging. 2019;50:1452-1460.

42. de Havenon A, Chung L, Park M, Mossa-Basha M. Intracranial vessel wall MRI: a review of current indications and future applications. Neurovascular Imaging. 2016;2:10.

43. Mandell DM, Mossa-Basha M, Qiao Y, et al. Intracranial vessel wall MRI: Principles and expert consensus recommendations of the American society of neuroradiology. Am J Neuroradiol. 2017;38:218-229.

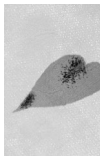

CHAPTER 5

Blood flow velocity pulsatility and arterial diameter pulsatility measurements of the intracranial arteries

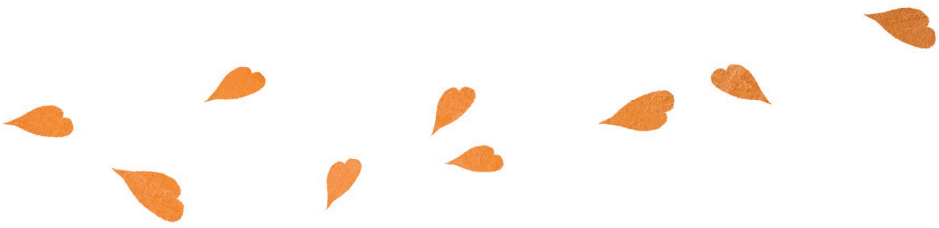

SUBMITTED FOR PUBLICATION:

Kees M. van Hespen, Hugo J. Kuijf, Jeroen Hendrikse, Peter R. Luijten, Jaco J.M. Zwanenburg.
Blood flow velocity pulsatility and arterial diameter pulsatility measurements of the intracranial arteries.

ABSTRACT

PURPOSE

4D phase contrast magnetic resonance imaging (PC-MRI) allows for the visualization and quantification of the cerebral blood flow. A drawback of software that is used to quantify the cerebral blood flow is that it oftentimes assumes a static arterial luminal area over the cardiac cycle. Quantifying the lumen area pulsatility index (aPI), i.e. the change in lumen area due to an increase in distending pressure over the cardiac cycle, can provide insight in the stiffness of the arteries. Arterial stiffness has received increased attention as a predictor in the development of cerebrovascular disease. In this study, we introduce software that allows for measurement of the aPI as well as the blood flow velocity pulsatility index (vPI) from 4D PC-MRI.

MATERIALS AND METHODS

The internal carotid arteries of seven volunteers were imaged using 7T MRI. The aPI and vPI measured from 4D PC-MRI using our software were validated against measurements from 2D PC-MRI at two levels of the internal carotid arteries (C3 and C7). Additionally, we investigated the consistency in blood flow rate between both segments.

RESULTS

The aPI and vPI computed from 4D PC-MRI were comparable to those measured from 2D PC-MRI (aPI: mean difference: 0.03 (limits of agreement: -0.14–0.23); vPI: 0.03 (-0.17–0.23)). The measured blood flow rate for the C3 and C7 segments was relatively similar, indicating that our proposed software correctly captures the variation in arterial lumen area and blood flow velocity that exists along the distal end of the carotid artery.

CONCLUSION

Our software may potentially aid in identifying changes in arterial stiffness of the intracranial arteries caused by pathological changes to the vessel wall.

INTRODUCTION

Arterial stiffness has received increased attention as a predictor in the development of cerebrovascular disease,[1,2] and is linked to pathological conditions such as hypertension,[3] diabetes,[4] and end-stage renal disease.[5] Increased arterial stiffness results in a more pulsatile flow to the smaller arteries,[6–9] where the excessive pulsatility could induce damage to the microcirculation,[10] leading to observable damage such as microbleeds,[11] lacunar infarcts,[12] and white matter hyperintensities.[13] In addition, an increase in arterial stiffness and blood flow velocity pulsatility have been linked to cognitive impairment.[6,14]

Traditionally, quantitative measurements on the blood flow are performed using transcranial Doppler ultrasound and 2D phase contrast (velocity) magnetic resonance imaging (PC-MRI).[15–17] Doppler ultrasound, although cheap and widely available, has several drawbacks including operator dependence and limited penetration of the ultrasound signal in the skull.[15] Similarly, 2D PC-MRI is dependent on operator skill, and is limited to measurements at a single position along an artery. In contrast, 4D PC-MRI sequences do not suffer from the disadvantages of transcranial Doppler ultrasound and 2D PC-MRI, and allow for 3D blood flow quantification of all vessels within a 3D volume. Although 4D PC-MRI is very time-consuming, ongoing developments in MRI, including parallel imaging[18] and compressed sensing[19,20] have enabled implementations with practically feasible scan times.

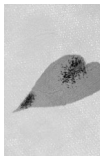

Several image processing tools have been proposed to interpret and analyze 4D PC-MRI data. Most tools are optimized for cardiac blood flow analysis.[21,22] Few methods focus on blood flow analysis in the intracranial arteries. Schrauben et al.[23] have proposed a center line tracking and segmentation method for 4D PC-MRI data of the intracranial arteries. Their segmentation method has later been implemented for patients with intracranial stenosis,[24] where center line tracking as well as lumen segmentation was performed. One drawback of these image processing tools for blood flow analysis of the intracranial arteries is that they assume a static luminal area across the cardiac cycle. The change in luminal area due to a rise in distending pressure over the cardiac cycle, can however provide insight in the arterial stiffness and provide—in combination with estimations of the pulse pressure—commonly used indices such as arterial distensibility or arterial compliance.[7,25]

In this study, we present software for measuring the intracranial blood flow velocity pulsatility as well as the lumen area pulsatility, as measure for the arterial stiffness, from 4D PC-MRI images. Additionally, we validated our blood flow velocity pulsatility and lumen area pulsatility measurements with measurements from 2D PC-MRI.

MATERIALS AND METHODS

For the quantification of the blood flow velocity pulsatility and lumen area pulsatility, image processing software was written in MeVisLab 3.1.1 (Fraunhofer Mevis, Germany[26]) for analysis of the 4D PC-MRI images. The image processing tool, available from https://bitbucket.org/KeesvanHespen/damping/, ran on a standard workstation (Intel Xeon E-1650v3, 32gb RAM). Measurements on the 4D PC-MRI images were validated against measurements performed on 2D PC-MRI images.

4D PC-MRI IMAGE PROCESSING

To extract the blood flow velocity pulsatility and lumen area pulsatility measures, several preprocessing steps were performed. Initially, a bias field correction was performed by fitting a first-degree polynomial surface through the time average of stationary voxels in the 4D PC-MRI phase images.[27] Additionally, phase unwrapping was applied to the 4D PC-MRI phase images. The 4D PC-MRI images were registered to the T1-weighted images, to compensate for subject displacement between scans. A center line of the intracranial arteries was acquired by applying a vesselness filter to the 3D T1w images, and subsequently performing a distance transform skeletonization of the filtered image (Figure 1B).[28] Manual start- and end positions were chosen on the skeleton, to select the vessel segment on which to evaluate the blood flow velocity pulsatility and lumen area pulsatility (Figure 1C).

Along the selected segment a multi-planar reconstruction (MPR) was created of the 4D PC-MRI magnitude and phase images in a region of 10x10 mm^2 around the center line (Figure 1D). The three directional velocity encoded phase images were combined to compute the blood flow velocity component perpendicular through each slice of the MPR.

For each MPR slice and cardiac phase, an isocontour was automatically drawn at the arterial lumen-background boundary at the full-width-at-half-maximum (FWHM) intensity value on the PC-MRI magnitude image,

computed per cardiac phase image (Figure 1E). The FWHM intensity value was calculated from a masked image using Otsu's method, separating the arterial lumen from the background.[29] The isocontour seed was initialized at the estimated radius of the vessel computed from a rough tubular tracking method applied on the MPR image stack.

The blood flow velocity pulsatility index was computed for each MPR slice as:

$$vPI = \frac{\max(v_{mean}) - \min(v_{mean})}{\text{mean}(v_{mean})},$$

where v_{mean} is the mean velocity computed within the drawn isocontour for each cardiac phase. The lumen area pulsatility index was measured in a similar way as:

$$aPI = \frac{\max(A) - \min(A)}{\min(A)},$$

with A, the cross-sectional luminal area over the cardiac cycle.

2D PC-MRI IMAGE PROCESSING

The processing and analysis of the 2D PC-MRI images was performed relatively similar to that of the 4D PC-MRI images. A manual seed point was generated in the center of the vessel lumen on the 2D PC-MRI magnitude image. Hereafter, isocontours were drawn automatically at the FWHM intensity value between arterial lumen and background for all cardiac phases. Otsu's thresholding was performed in a region of 10x10 mm^2 surrounding the seed point, to separate the arterial lumen from the background, and to subsequently calculate the FWHM intensity value. The blood flow velocity pulsatility was calculated within the isocontours from the 2D PC-MRI phase images, and the lumen area pulsatility was calculated from the cross-sectional luminal area.

STUDY PARTICIPANTS

For validation of our software, MR image data was acquired from seven healthy volunteers (age range: 23–28 years, 3 males), which were included in this study after obtaining written informed consent. Data acquisition was approved by the local institutional review board.

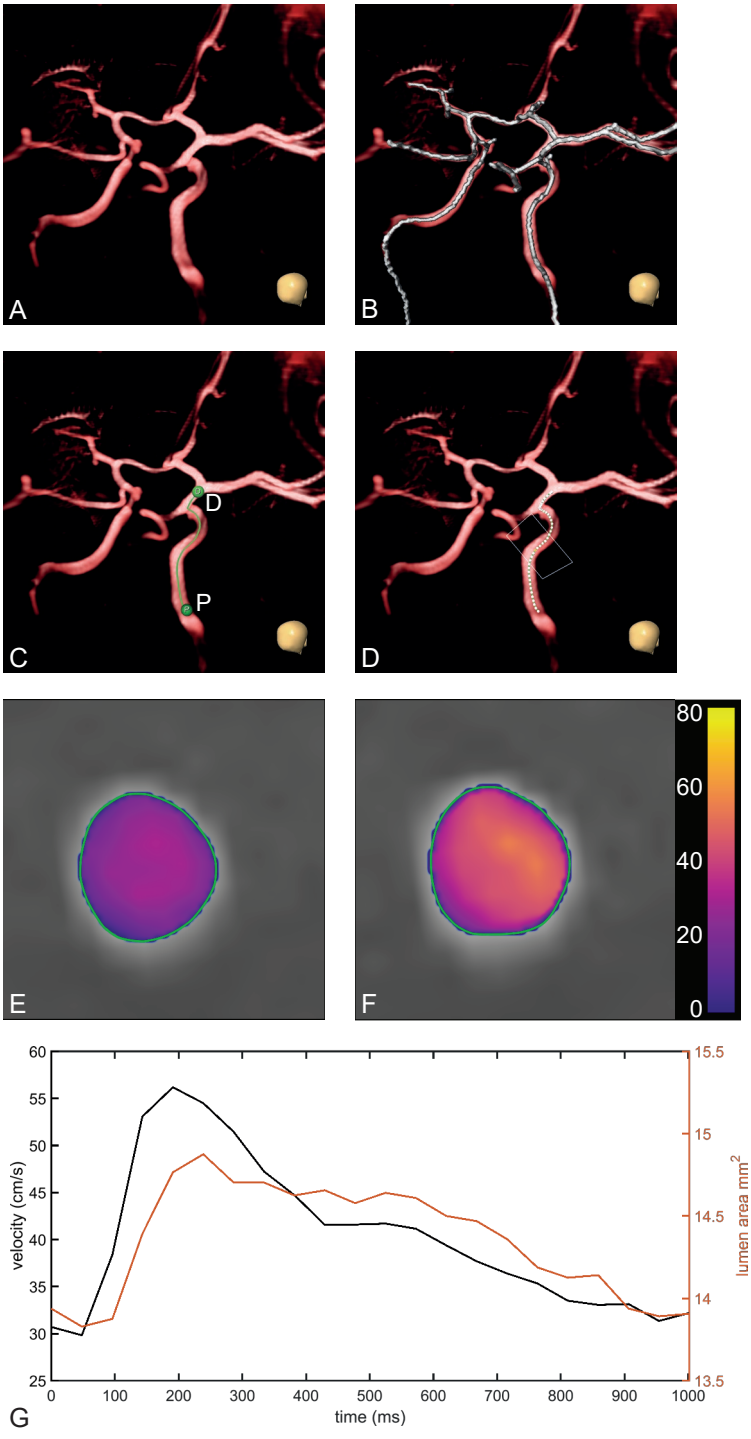
A
B
C
D
P
D
E
F
80
60
40
20
0
G
velocity (cm/s)
lumen area mm2
time (ms)
60
55
50
45
40
35
30
25
15.5
15
14.5
14
13.5
0
100
200
300
400
500
600
700
800
900
1000

Figure 1. Blood flow velocity pulsatility and lumen area pulsatility measurement pipeline. (A) 3D rendering of T1-weighted image, thresholded to show the circle of Willis arteries. Skull inset in the bottom right corner shows the orientation (coronal view of the circle of Willis in anterior direction). (B) Projected center line skeleton. Note that the skeleton extends in the extracranial carotids and the basilar artery, that are not rendered from the T1-weighted image. (C) Selected start- and end locations as 'P' (proximal), and 'D' (distal). The center line is generated between these points from the skeleton. (D) Measurement locations, given by the white dots along the center line. The white rectangle corresponds to the multi-planar reconstruction (MPR) slice given in (E) and (F), which is located at the end of the C3 segment. The detected luminal area for this MPR slice and timepoint is given by the green outline, with the velocity in cm/s projected in color for the end-diastolic (E) and systolic (F) cardiac phases. Mean velocities and lumen areas over the cardiac cycle for this MPR slice are given in (G).

MRI ACQUISITION

MR examinations were performed on a 7T MRI scanner (Philips, Best, the Netherlands), using an 8-channel transmit coil and a 32-channel receive head coil (Nova Medical, Inc., Wilmington, MA, USA). A 3D T1-weighted gradient echo image was acquired for anatomical reference. A retrospectively-gated 4D PC-MRI acquisition (acquired voxel size: 0.78x0.78x0.8 mm^3, field of view: 250x250x24.8 mm^3, reconstructed cardiac phases: 22, flip angle: 15 degrees, repetition time (TR) = 4.51 ms; echo time (TE) = 2.3 ms, SENSE: 3, velocity encoding (v_{enc}): 100 cm/s) was angulated to include the intracranial parts of the carotid arteries. The 4D PC-MRI scan was acquired for RL, AP and FH velocity encoding separately. The associated scan duration was three times 5 minutes and 10 seconds for a heart rate of 60 bpm. For validation purposes, two retrospectively-gated 2D PC-MRI acquisitions were performed (acquired voxel size: 0.19x0.19x3 mm^3, field of view: 250x250x3 mm^3, reconstructed cardiac phases: 25, flip angle: 50 degrees, repetition time (TR) = 17 ms; echo time (TE) = 4.2 ms, SENSE: 2, v_{enc}: 120 cm/s), where one was angulated at the C3 level and one at the C7 level of the internal carotid artery, given the classification by Bouthillier.[30] The C3 and C7 locations were chosen, as recent work has shown considerable difference in both area and velocity pulsations between these two segments.[31] The scan duration for the 2D PC-MRI acquisition was 2 minutes and 6 seconds for a heart rate of 60 bpm.

EXPERIMENTAL SETUP

We validated the blood flow velocity pulsatility and lumen area pulsatility measured from the 4D PC-MRI images, against measurements performed on 2D PC-MRI images at the same anatomical locations. Additionally, we measured the preservation of blood flow rate between the C3 and C7 segments, given the mean blood velocity and arterial lumen area. Additionally, we compared the blood flow rate measured from 4D PC-MRI with measurements from 2D PC-MRI.

As an example, we also show the blood flow velocity pulsatility and lumen area pulsatility indices for one volunteer for a large part of the circle of Willis, including the internal carotid arteries, anterior cerebral arteries, middle cerebral arteries, posterior communicating arteries/posterior cerebral arteries.

RESULTS

The velocity pulsatility index and lumen area pulsatility index for both the C3 and C7 segment are shown in Figure 2. The blood flow velocity pulsatility indices computed from 4D PC-MRI images were comparable to those measured from 2D PC-MRI images. On average, the difference in blood flow velocity pulsatility between 2D and 4D measurements was 0.03 (limits of agreement: -0.17–0.23). Similarly, on average, the difference in lumen area pulsatility between 2D and 4D measurements was 0.05 (limits of agreement: -0.16–0.26).

Both 2D and 4D measurements, on average, show an increase in lumen area pulsatility between the C3 and C7 segments (Figure 3). The average lumen area pulsatility is 0.08 and 0.21, and 0.10 and 0.24 for the C3 and C7 segments, given the 2D and 4D measurements, respectively. Similarly, a decrease is observed in the blood flow velocity pulsatility between the C3 and C7 segments. On average, the blood flow velocity pulsatility is 0.74 and 0.60, and 0.75 and 0.65 for the 2D and 4D measurements, respectively.

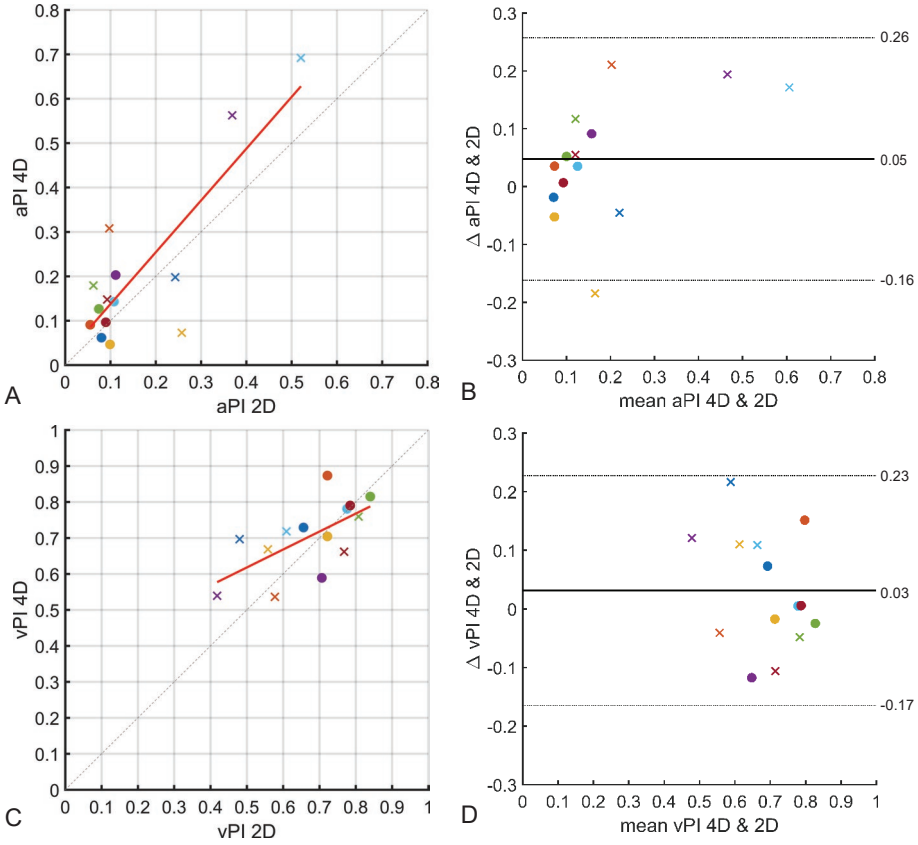

Figure 2. Comparison between 2D and 4D area lumen pulsatility (aPI) and blood flow velocity pulsatility (vPI) measurements. (A) and (C) show the relation between 2D and 4D measurements on the x and y axes, respectively. The $y = x$ line is given by the dashed gray line, and the red line is the line of best fit ($vPI_{4D} = 0.50\ vPI_{2D} + 0.37$ and $vAI_{4D} = 1.17\ vAI_{2D} + 0.02$). Bland-Altman plots are given in (B) and (D). Measurements at C3 and C7 level are given by circles and crosses, respectively. The colors of the crosses and circles correspond to individual volunteers and correspond to the color coding used in Figure 3.

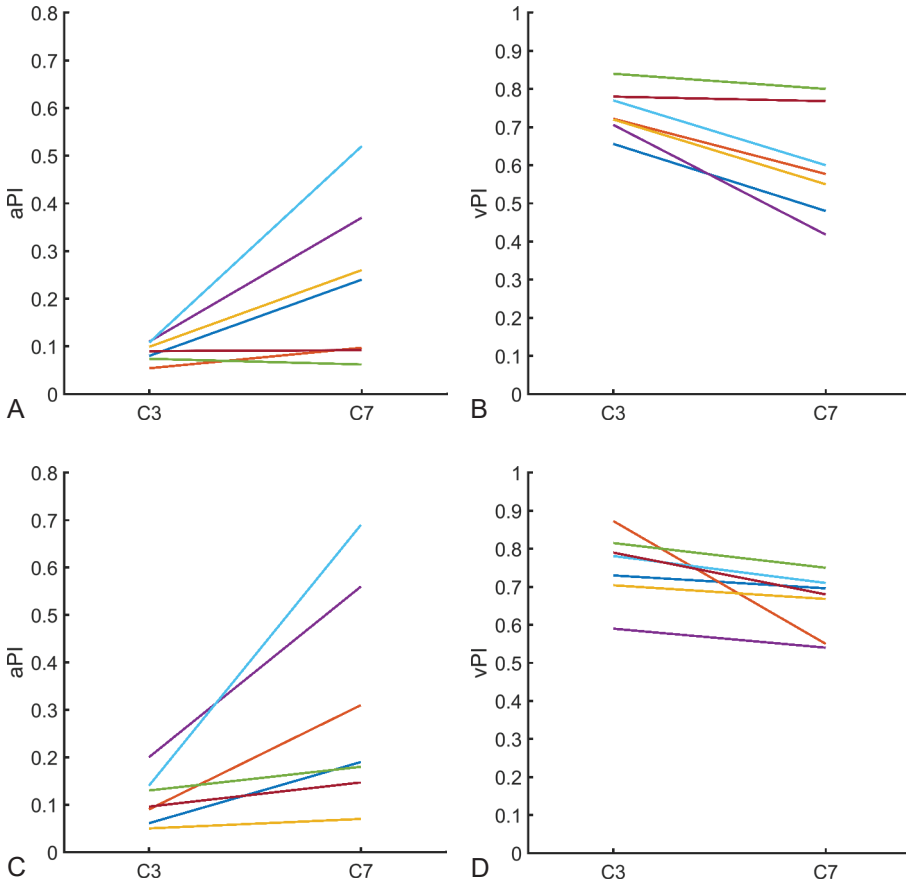

Figure 3. Comparison between the C3 and C7 segments. In (A) and (B), the 2D measurements are given, and (C) and (D), show the 4D measurements. The colors correspond to the individual participants to facilitate direct comparison between individual measurements, and are similar to those used in Figure 2. On average, an increase and decrease can be observed between C3 and C7 in lumen area pulsatility (aPI) and blood flow velocity pulsatility (vPI), respectively.

For both 2D and 4D measurements, the blood flow rate was largely preserved between the C3 and C7 segment. In Table 1, the blood flow rate in ml/s is given for all volunteers. On average, the difference in blood flow rate between C3 and C7 was -0.03 ± 0.24 ml/s, and -0.07 ± 0.21 ml/s given the 2D and 4D measurements, respectively. Even though the blood flow rate was preserved between the C3 and C7 segments, the blood flow rate calculated from 2D was in all cases 20% to 46% higher than the blood flow rate calculated from 4D images.

Table 1. Blood flow rate preservation between C3 and C7 segments. The blood flow rate in ml/s is given for the C3 and C7 segments, measured from 2D and 4D images. Blood flow rate was averaged over the cardiac cycle. Rows correspond to individual volunteers. The %diff denotes the difference between C3 and C7, against the blood flow rate at the C3 level.

	2D			4D		
Volunteer	**C3**	**C7**	**%diff**	**C3**	**C7**	**%diff**
1	4.59	4.29	-6.5	3.30	3.05	-7.5
2	4.26	4.48	5.1	3.40	3.27	-3.7
3	5.77	5.56	-3.6	4.02	3.65	-9.1
4	3.99	4.28	7.2	2.92	3.11	6.7
5	4.12	3.85	-6.5	2.95	2.81	-4.8
6	3.22	3.01	-6.6	1.73	1.75	1.3
7	2.94	2.85	-3.2	2.08	2.23	7.6

In Figure 4 we show blood flow velocity pulsatility and lumen area pulsatility indices for a large part of the circle of Willis for one volunteer. A decrease in blood flow velocity pulsatility can be observed along both internal carotid arteries, whereas the lumen area pulsatility increases. Both the lumen area pulsatility and blood flow velocity pulsatility are high in the anterior cerebral arteries and in the posterior cerebral arteries. Left and right arteries show similar blood flow velocity pulsatility values, whereas there is more variation in lumen area pulsatility.

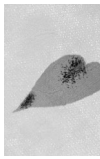

DISCUSSION

In this study, we introduced software for measuring the blood flow velocity pulsatility and lumen area pulsatility of the intracranial arteries from 4D PC-MRI images. We have shown that the blood flow velocity pulsatility measurements using our software on 4D PC-MRI images correspond well to measurements on 2D PC-MRI images. A significant decrease and increase in blood flow velocity pulsatility and lumen area pulsatility, respectively, were observed between the C3 and C7 segment of the internal carotid artery. On average, the lumen area pulsatility was 140% higher in the C7 segment compared to the C3 segment, and the blood flow velocity pulsatility was 13.3% lower in the C7 segment compared to the C3 segment. When combining blood flow velocity and luminal area measurements, the blood flow rate was mostly preserved.

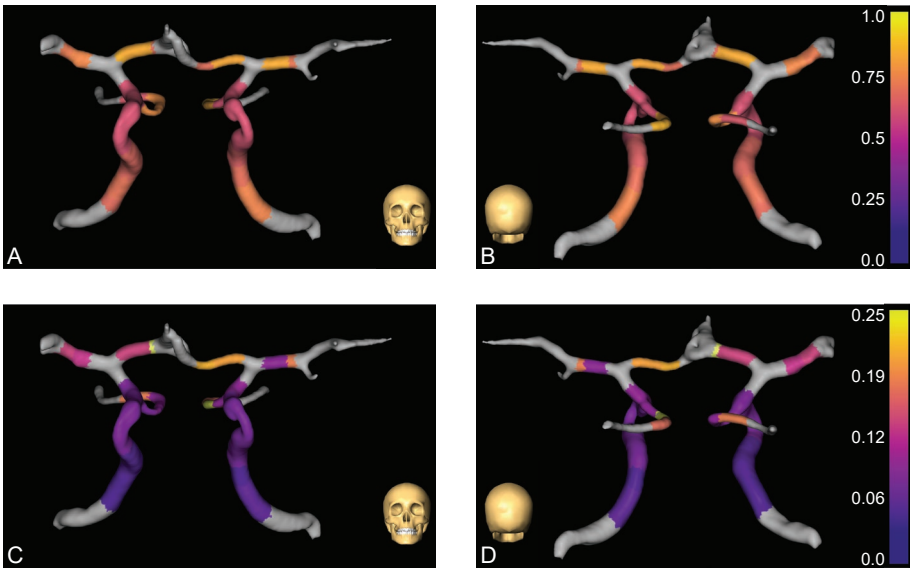

Figure 4. Blood flow velocity pulsatility and lumen area pulsatility indices over multiple arteries of the circle of Willis for one volunteer. (A) and (C) show a coronal view in dorsal direction, and (B) and (D) show a coronal view in ventral direction. In (A) and (B), the blood flow velocity pulsatility is given, and in (C) and (D), the lumen area pulsatility is given for part of the circle of Willis. The bottom most arteries are the internal carotids, that branch of into the posterior communicating arteries/posterior cerebral arteries. The basilar artery is not shown. The internal carotids branch outwards into the middle cerebral arteries, and inwards in the anterior cerebral arteries that join in the middle of the panels. A decrease in blood flow velocity pulsatility can be observed along both internal carotid arteries, whereas the lumen area pulsatility increases. Both the lumen area pulsatility and blood flow velocity pulsatility are high in the anterior cerebral arteries.

The change in blood flow velocity pulsatility between the C3 and C7 segments is comparable to the change in pulsatility observed by Schubert et al.[16] The absolute pulsatility values are however higher in the work by Schubert et al., which can potentially be explained by differences in the definition of the pulsatility index. Schubert et al. used volume flow rates (in ml/min) to calculate the pulsatility index, whereas we used the blood flow velocity. Van Tuijl et al.[31] report similar blood flow velocity pulsatility indices for the C3 and C7 segments.

Besides the pulsatility and blood flow velocity, the arterial stiffness is an important biomarker for vascular health. There are three commonly used non-invasive ways to derive the arterial stiffness.[25] The first one derives the arterial stiffness from the time delay in the arrival of the arterial pulse wave. This method has been properly validated, but is commonly used in the larger

arteries where the temporal resolution of PC-MRI sequences are sufficient for measuring this delay.[32] For the intracranial arteries the temporal resolution of used 4D PC-MRI sequences is too low to measure this. However, Peper et al.[33] have developed a 2D PC-MRI sequence with a temporal resolution that is high enough to measure the arrival time delay between sections of the (internal) carotid artery. Secondly, the arterial stiffness can be derived from analysis of specific components of the arterial pressure or flow waveform.[25] Thirdly, the arterial stiffness can be derived by measuring the change in luminal area/diameter given the increase in pulse pressure, i.e. the arterial distensibility. In the current study, we did not possess pulse pressure measurements. However, the observed changes in luminal area over the cardiac cycle for the C3 and C7 segments corresponded to values reported by van Tuijl et al.[31] Taking an average pulse pressure of 40 mmHg for healthy volunteers, the lumen area pulsatility at C7 (where the vessel is not hampered by the bony carotid canal, as is the case for C3) corresponds to an arterial distensibility of 0.50 %/mmHg, which corresponds well with values reported for the intracranial arteries.[31,34–36]

We observed that the measured blood flow rate between the C3 and C7 was largely preserved. This shows that our proposed software correctly captures the variation in arterial lumen area and blood flow velocity pulsatility that exists along the distal end of the carotid artery.[16,31] In most cases, the blood flow rate was slightly lower at the C7 level. This difference may be caused by the ophthalmic artery, that is connected to the internal carotid at the C6 level. Ambarki et al.[37] show that in healthy young volunteers the average flow rate through the ophthalmic artery is 0.17 ml/s, which might (partially) explain the lowered blood flow rate at the C7 level. The observed difference in flow rate between C3 and C7 are relatively comparable between 2D and 4D, strengthening the idea that this observed difference in flow rate is caused by the ophthalmic artery branch. However, in some cases we observe a (slight) increase in blood flow rate between the C3 and C7 level, which is very implausible in this group of healthy young volunteers (only in patients with severe carotid artery stenosis, this may indicate collateral flow via a reversed flow direction in the ophthalmic artery[38]). Between 2D and 4D measurements, the flow rate was 20% to 40% lower given the 4D PC-MRI images. This is potentially caused by the difference in spatial resolution between the 2D and 4D PC-MRI acquisitions (in-plane resolution, 2D: 0.19 mm. 4D: 0.78 mm).[39,40] The voxels at the edge of the lumen suffer from more severe partial volume effects in the 4D PC-MRI images. This lowers the image intensity for these voxels, subsequently leading to smaller delineated luminal areas.

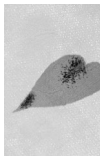

The difference in blood flow rate can also be caused by the image intensity threshold used to delineate the arterial lumen. Dunås et al.[41] show that delineating the arterial lumen at an intensity of 20% of the maximum intensity of the complex difference PC-MRI image yields the lowest difference with 2D PC-MRI blood flow rate measurements. We delineated the arterial lumen from the background at FWHM intensity value in the PC-MRI magnitude image. However, we used the same isocontours intensity threshold for both 4D and 2D images, whereas Dunås et al. used a commercial tool for the segmentation of the arterial lumen on 2D PC-MRI images. Additionally, the lower temporal resolution of the 4D PC-MRI acquisition compared with the temporal resolution of the 2D PC-MRI acquisition may partially explain the lower observed blood flow rate measured from 4D PC-MRI.[39]

(Commercial) software for measuring blood flow rate and pulsatility of the intracranial arteries are readily available for analysis of 4D PC-MRI images,[23,24] but commonly assume a static lumen over the cardiac cycle. Software that does allow for dynamic measurement of the arterial lumen is often times tailored to the large extracranial arteries such as the aorta. Our developed software allows for calculation of a dynamic luminal area over the cardiac cycle for the intracranial arteries. In the future, measuring local changes in the arterial stiffness of the intracranial arteries may provide more insight in cerebrovascular disease progression, and may be linked to damage to the brain parenchyma.[11,42–44]

Several limitations have potentially influenced the outcome of our study. First, the relatively low number of included volunteers could potentially influence the average observed effect of changes to blood flow velocity pulsatility and lumen area pulsatility. However, almost all of our volunteers showed a similar direction of change in blood flow velocity pulsatility and lumen area pulsatility between the C3 and C7 segments. Second, in some cases, flow voids were present in the 2D and 4D acquisitions, which challenged the automated contour drawing algorithm. In such cases, manual delineation around the flow void was required. These manual corrections could have influenced our measurements. However, flow voids—if present—were only visible on a few timepoints, for which manual editing was necessary. In most cases, the automated algorithm performed well. Third, the inflow effect of slow flowing blood near the edges of the lumen could have potentially increased the apparent luminal area in the 4D PC-MRI images. We minimized this effect by angulating the 4D PC-MRI acquisition such that the internal carotid below the C3 segment was outside of the field of view. Fourth, the challenging

angulation of the 2D PC-MRI on the C7 segment potentially influenced the measurements. However, potential errors in the angulation of our 2D PC-MRI sequence are likely minimal, because blood flow rate measurements at the C7 level were found comparable to those at the C3 level, and the results were comparable to the 4D flow analysis where the perpendicular cross-section was automatically derived from the detected center line of the vessel.

Our software allowed for measurement of the blood flow velocity pulsatility and lumen area pulsatility on 4D PC-MRI images. The measurements of our software were validated against measurements performed on 2D PC-MRI images. Given that the flow between both evaluated segments of the internal carotid artery were largely preserved shows that this software is capable of measuring the variation in arterial lumen area and blood flow velocity over the cardiac cycle. Our software may potentially aid in identifying changes in arterial stiffness of the intracranial arteries caused by pathological changes to the vessel wall.

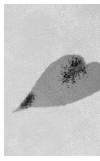

REFERENCES

1. Dalgleish T, Williams JMG., Golden A-MJ, et al. Atherosclerosis, Large Arteries and Cardiovascular Risk. In: Safar ME, Frohlich ED, eds. Journal of Experimental Psychology: General. Vol 44. Advances in Cardiology. Basel: S. Karger AG; 2006:234-244.

2. Zarrinkoob L, Ambarki K, Wåhlin A, et al. Aging alters the dampening of pulsatile blood flow in cerebral arteries. J Cereb Blood Flow Metab. 2016;36:1519-1527.

3. Boutouyrie P, Tropeano AI, Asmar R, et al. Aortic stiffness is an independent predictor of primary coronary events in hypertensive patients: A longitudinal study. Hypertension. 2002;39:10-15.

4. Muhammad IF, Borné Y, Östling G, et al. Arterial stiffness and incidence of diabetes: A population-based cohort study. Diabetes Care. 2017;40:1739-1745.

5. Blacher J, Pannier B, Guerin AP, Marchais SJ, Safar ME, London GM. Carotid arterial stiffness as a predictor of cardiovascular and all- cause mortality in end-stage renal disease. Hypertension. 1998;32:570-574.

6. Mitchell GF, van Buchem MA, Sigurdsson S, et al. Arterial stiffness, pressure and flow pulsatility and brain structure and function: the Age, Gene/Environment Susceptibility--Reykjavik study. Brain. 2011;134:3398-3407.

7. O'Rourke MF, Hashimoto J. Mechanical Factors in Arterial Aging: A Clinical Perspective. J Am Coll Cardiol. 2007;50:1-13.

8. Shirwany NA, Zou M. Arterial stiffness: a brief review. Acta Pharmacol Sin. 2010;31:1267-1276.

9. Webb AJS, Simoni M, Mazzucco S, Kuker W, Schulz U, Rothwell PM. Increased cerebral arterial pulsatility in patients with leukoaraiosis: Arterial stiffness enhances transmission of aortic pulsatility. Stroke. 2012;43:2631-2636.

10. Schnerr RS, Jansen JFAA, Uludag K, et al. Pulsatility of lenticulostriate arteries assessed by 7 Tesla flow MRI-Measurement, reproducibility, and applicability to aging effect. Front Physiol. 2017;8:1-10.

11. Zhai F-F, Ye Y-C, Chen S-Y, et al. Arterial Stiffness and Cerebral Small Vessel Disease. Front Neurol. 2018;9:723.

12. Chuang SY, Cheng HM, Bai CH, Yeh WT, Chen JR, Pan WH. Blood Pressure, Carotid Flow Pulsatility, and the Risk of Stroke: A Community-Based Study. Stroke. 2016;47:2262-2268.

13. Aribisala BS, Morris Z, Eadie E, et al. Blood Pressure, Internal Carotid Artery Flow Parameters, and Age-Related White Matter Hyperintensities. Hypertension. 2014;63:1011-1018.

14. Muhire G, Iulita MF, Vallerand D, et al. Arterial Stiffness Due to Carotid Calcification Disrupts Cerebral Blood Flow Regulation and Leads to Cognitive Deficits. J Am Heart Assoc. 2019;8.

15. Markus HS. Transcranial Doppler ultrasound. J Neurol Neurosurg Psychiatry. 1999;67:135-137.

16. Schubert T, Santini F, Stalder AF, et al. Dampening of Blood-Flow Pulsatility along the Carotid Siphon: Does Form Follow Function? Am J Neuroradiol. 2011;32:1107-1112.

17. Dunås T, Wåhlin A, Zarrinkoob L, Malm J, Eklund A. 4D flow MRI—Automatic assessment of blood flow in cerebral arteries. Biomed Phys Eng Express. 2018;5:015003.

18. Pruessmann KP, Weiger M, Scheidegger MB, Boesiger P. SENSE: Sensitivity encoding for fast MRI. Magn Reson Med. 1999;42:952-962.

19. Peper ES, Gottwald LM, Zhang Q, et al. Highly accelerated 4D flow cardiovascular magnetic resonance using a pseudo-spiral Cartesian acquisition and compressed sensing reconstruction for carotid flow and wall shear stress. J Cardiovasc Magn Reson. 2020;22:7.

20. Gottwald LM, Töger J, Markenroth Bloch K, et al. High Spatiotemporal Resolution 4D Flow MRI of Intracranial Aneurysms at 7T in 10 Minutes. Am J Neuroradiol. 2020;41:1201-1208.

21. Sinha V, Hautvast G, Sonnemans J, de Bliek H, Jalba A, Breeuwer M. Fast and easy visualization of blood flow patterns in 4D Qflow MRI. J Cardiovasc Magn Reson. 2012;14:W46.

22. Köhler B, Grothoff M, Gutberlet M, Preim B. Bloodline: A system for the guided analysis of cardiac 4D PC-MRI data. Comput Graph. 2019;82:32-43.

23. Schrauben E, Wåhlin A, Ambarki K, et al. Fast 4D flow MRI intracranial segmentation and quantification in tortuous arteries. J Magn Reson Imaging. 2015;42:1458-1464.

24. Vali A, Aristova M, Vakil P, et al. Semi-automated analysis of 4D flow MRI to assess the hemodynamic impact of intracranial atherosclerotic disease. Magn Reson Med. 2019;82:749-762.

25. Oliver JJ, Webb DJ. Noninvasive assessment of arterial stiffness and risk of atherosclerotic events. Arterioscler Thromb Vasc Biol. 2003;23:554-566.

26. Ritter F, Boskamp T, Homeyer A, et al. Medical Image Analysis. IEEE Pulse. 2011;2:60-70.

27. Lankhaar J-W, Hofman MBM, Marcus JT, Zwanenburg JJM, Faes TJC, Vonk-Noordegraaf A. Correction of phase offset errors in main pulmonary artery flow quantification. J Magn Reson Imaging. 2005;22:73-79.

28. Frangi AF, Niessen WJ, Vincken KL, Viergever MA. Multiscale vessel enhancement filtering. In: Wells WM, Colchester A, Delp S, eds. Medical Image Computing and Computer-Assisted Intervention --- MICCAI'98. Berlin, Heidelberg: Springer; 1998:130-137.

29. Otsu N. A Threshold Selection Method from Gray-Level Histograms. IEEE Trans Syst Man Cybern. 1979;9:62-66.

30. Bouthillier A, van Loveren HR, Keller JT. Segments of the Internal Carotid Artery: A New Classification. Neurosurgery. 1996;38:425-433.

31. van Tuijl RJ, Ruigrok YM, Velthuis BK, van der Schaaf IC, Rinkel GJE, Zwanenburg JJM. Velocity Pulsatility and Arterial Distensibility Along the Internal Carotid Artery. J Am Heart Assoc. 2020;9:e016883.

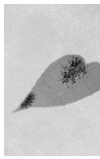

32. Wentland AL, Grist TM, Wieben O. Review of MRI-based measurements of pulse wave velocity: a biomarker of arterial stiffness. Cardiovasc Diagn Ther. 2014;4:193-206.

33. Peper ES, Strijkers GJ, Gazzola K, et al. Regional assessment of carotid artery pulse wave velocity using compressed sensing accelerated high temporal resolution 2D CINE phase contrast cardiovascular magnetic resonance. J Cardiovasc Magn Reson. 2018;20:86.

34. Warnert EAH, Murphy K, Hall JE, Wise RG. Noninvasive Assessment of Arterial Compliance of Human Cerebral Arteries with Short Inversion Time Arterial Spin Labeling. J Cereb Blood Flow Metab. 2015;35:461-468.

35. Studinger P, Lénárd Z, Kováts Z, Kocsis L, Kollai M. Static and dynamic changes in carotid artery diameter in humans during and after strenuous exercise. J Physiol. 2003;550:575-583.

36. Giannattasio C, Salvi P, Valbusa F, et al. Simultaneous Measurement of Beat-to-Beat Carotid Diameter and Pressure Changes to Assess Arterial Mechanical Properties. Hypertension. 2008;52:896-902.

37. Ambarki K, Hallberg P, Jóhannesson G, et al. Blood Flow of Ophthalmic Artery in Healthy Individuals Determined by Phase-Contrast Magnetic Resonance Imaging. Investig Opthalmology Vis Sci. 2013;54:2738.

38. Zarrinkoob L, Wåhlin A, Ambarki K, Birgander R, Eklund A, Malm J. Blood Flow Lateralization and Collateral Compensatory Mechanisms in Patients With Carotid Artery Stenosis. Stroke. 2019;50:1081-1088.

39. Bollache E, van Ooij P, Powell A, Carr J, Markl M, Barker AJ. Comparison of 4D flow and 2D velocity-encoded phase contrast MRI sequences for the evaluation of aortic hemodynamics. Int J Cardiovasc Imaging. 2016;32:1529-1541.

40. Stalder AF, Russe MF, Frydrychowicz A, Bock J, Hennig J, Markl M. Quantitative 2D and 3D phase contrast MRI: Optimized analysis of blood flow and vessel wall parameters. Magn Reson Med. 2008;60:1218-1231.

41. Dunås T, Holmgren M, Wåhlin A, Malm J, Eklund A. Accuracy of blood flow assessment in cerebral arteries with 4D flow MRI: Evaluation with three segmentation methods. J Magn Reson Imaging. 2019;50:511-518.

42. Lee W-J, Jung K-H, Ryu YJ, et al. Progression of Cerebral White Matter Hyperintensities and the Associated Sonographic Index. Radiology. 2017;284:824-833.

43. Saji N, Toba K, Sakurai T. Cerebral Small Vessel Disease and Arterial Stiffness: Tsunami Effect in the Brain? Pulse. 2016;3:182-189.

44. Birnefeld J, Wåhlin A, Eklund A, Malm J. Cerebral arterial pulsatility is associated with features of small vessel disease in patients with acute stroke and TIA: a 4D flow MRI study. J Neurol. 2020;267:721-730.

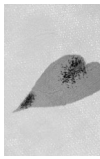

CHAPTER 6

The odd one out

AN ANOMALY DETECTION APPROACH TO IDENTIFY CHRONIC BRAIN INFARCTS ON MRI

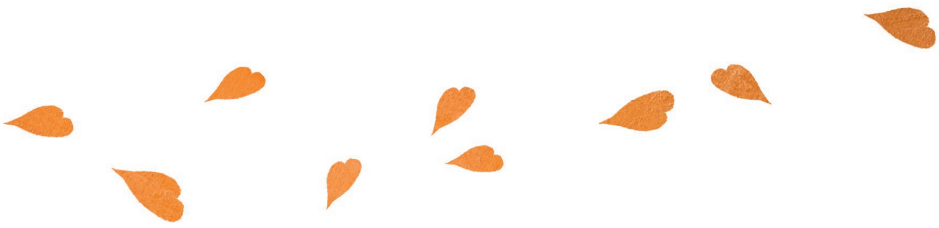

PUBLISHED AS:

SCIENTIFIC REPORTS. IN PRESS.

Kees M. van Hespen, Jaco J.M. Zwanenburg, Jan W. Dankbaar, Mirjam I. Geerlings, Jeroen Hendrikse, Hugo J. Kuijf.

An Anomaly Detection Approach to Identify Chronic Brain Infarcts on MRI.

ABSTRACT

PURPOSE

We propose an anomaly detection method using a neural network architecture for the detection of brain pathology on brain magnetic resonance (MR) images. A neural network was trained to capture the image features representing the healthy, asymptomatic brain. The performance of the network on the detection of brain pathology was tested on brain MR images of patients with chronic brain infarcts.

MATERIALS AND METHODS

The MR image data consisted of T1-weighted images and T2-weighted fluid-attenuated inversion recovery brain images, acquired as part of the SMART-MR study, of 1007 patients, including 274 patients with brain infarcts. A fully convolutional neural network was trained to encode the brain MR image features of 733 patients without brain infarcts in a latent space representation. For the test set, which consisted of brain MR image data of 225 patients with brain infarcts, an anomaly score was calculated as the modified Z-score from this latent space representation. Brain regions in these patients were marked as a suspected anomaly if the anomaly score of a region was larger than 3. We investigated how these suspected anomalies corresponded with previously annotated brain infarcts and other pathology.

RESULTS

Our proposed method detected 374 chronic brain infarcts (68% of the total amount of brain infarcts) which represented 97.5% of the total infarct volume. Additionally, 26 new brain infarcts were identified that were originally missed by the radiologist during radiological reading. Our proposed method also detected white matter hyperintensities, anomalous calcifications, and imaging artifacts.

CONCLUSION

In conclusion, this work shows that anomaly detection is a powerful approach for the detection of multiple brain abnormalities, and can potentially be used to improve the radiological workflow efficiency by guiding radiologists to brain anomalies which otherwise remain unnoticed.

INTRODUCTION

In clinical practice, radiologists acquire and assess magnetic resonance (MR) images of the brain for the diagnosis of various brain pathologies. Unfortunately, the process of reading brain MR images is laborious and observer dependent.[1–5] To reduce observer dependence, and to improve workflow efficiency and diagnostic accuracy, automated (machine learning/'artificial intelligence') methods have been proposed to assist the radiologist.[6–13] A common drawback of these methods is their 'point solution' design, in which they are focused on a specific type of brain pathology. Furthermore, the performance of supervised machine learning based solutions is dependent on the quantity and quality of available examples of pathology. In, for example, cerebral small vessel disease, the development of such solutions is challenging, because the parenchymal damage is heterogeneous in image contrast, morphology, and size.[14,15]

A solution that breaks with this conventional approach is anomaly detection: a machine learning approach that can identify all anomalies solely based on features that describe normal data. Because the features of possible anomalies were not learned, they stand out from the ordinary, and can subsequently be detected. Anomaly detection methods are particularly useful when there is an interest in the detection of anomalous events, but their manifestation is unknown a priori and their occurrence is limited.[16,17] Examples of applications include credit card fraud detection,[18] IT intrusion detection,[19] monitoring of aerospace engines during flight,[20] heart monitoring,[21] detection of illegal objects in airport luggage,[22] or the detection of faulty semiconductor wafers.[23]

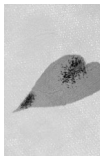

In medical imaging, variational autoencoders and generative adversarial networks have been proposed for anomaly detection tasks. Schlegl et al.[24,25] have developed a generative adversarial network architecture for the detection of abnormalities on optical coherence tomography images. For brain MRI, models have been developed for the detection of tumor tissue,[26–28] white matter hyperintensities,[29,30] multiple sclerosis lesions,[31,32] and acute brain infarcts.[28]

One of the manifestations of cerebral small vessel disease are chronic brain infarcts, including cortical, subcortical, and lacunar infarcts; each with a different appearance on MRI.[14,15] Identification of these infarcts is important, because their occurrence is associated with vascular dementia, Alzheimer's

disease, and overall cognitive decline.[33,34] Because of the heterogeneity in appearance of chronic brain infarcts, location and morphology on MRI, anomaly detection would be a possible solution for the identification of these infarcts.

In this study, we constructed an anomaly detection method using a neural network architecture for the detection of chronic brain infarcts from MRI.

MATERIALS AND METHODS

MR ACQUISITION

In this retrospective study, we used MR image data from the SMART-MR study[35], a prospective study on the determinants and course of brain changes on MRI, where all eligible patients that were newly referred to our hospital with manifestations of coronary artery disease, cerebrovascular disease, peripheral arterial disease or an abdominal aortic aneurysm were included after acquiring written informed consent. This study was conducted in accordance with national guidelines and regulations, and has been approved by the University Medical Center Utrecht Medical Ethics Review Committee (METC). In total 967 patients, including 270 patients with brain infarcts (see Table 1 for patient demographics), were included in the current study, see Figure 1 for exclusion criteria. The imaging data was acquired at 1.5T (Gyroscan ACS-NT, Philips, Best, the Netherlands), and consisted of a T1-weighted gradient echo sequence (repetition time (TR) = 235 ms; echo time (TE) = 2 ms), and a T2-weighted fluid-attenuated inversion recovery (T2-FLAIR) sequence (TR = 6000 ms; TE = 100 ms; inversion time: 2000 ms) (example given in Figure 2). Both MRI sequences had a reconstructed resolution of 0.9×0.9×4.0 mm^3, consisted of 38 contiguous transversal slices, and were coregistered.[35]

Table 1. Demographics of the patient groups with and without brain infarct, used for the training/training-validation, and validation/test sets, respectively. The age is given as: mean ± standard deviation

Characteristics	Patients without brain infarcts	Patients with brain infarcts
No. of patients	697	270
Age (years)	57 ± 10	62 ± 10
Male sex	550	213

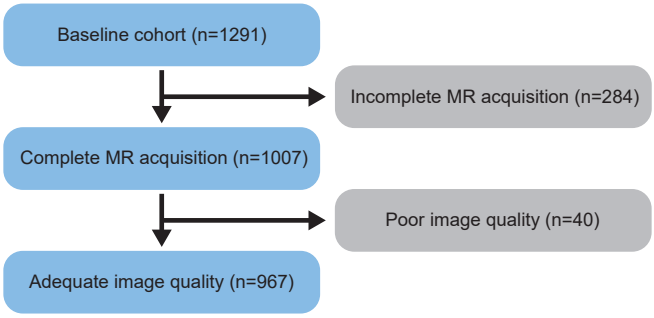

Figure 1. Flowchart showing exclusion of patients in the current study. In total 324 out of 1291 patients were excluded from the current study because of an incomplete MR acquisition (284), where one of two acquired MR images were missing, and because of poor image quality (40).

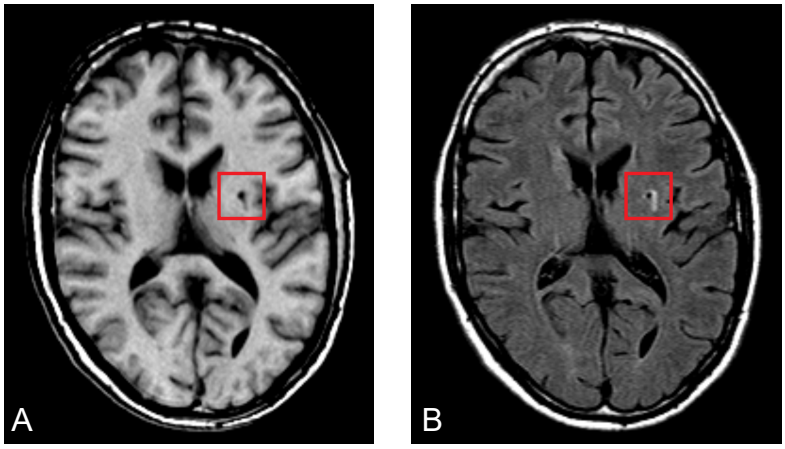

Figure 2. Example transversal image slice of the T1-weighted (A) and T2-FLAIR (B) acquisitions. A brain infarct can be observed in the right hemisphere next to the basal ganglia, in the red square, as the hypointense region in the T1-weighted image (A) and the hypointense region with hyperintense ring in the T2-FLAIR image (B).

All chronic brain infarcts—including cortical infarcts, lacunar infarcts, large subcortical infarct, and infratentorial infarcts—in these images, have been manually delineated by a neuroradiologist with more than 30 years of experience, as described by Geerlings et al.[35] in more detail.

IMAGE PREPROCESSING

The images of both acquisitions were preprocessed by applying N4 bias field correction.[36] Additionally, image intensities were normalized such that the 5th percentile of pixel values within an available brain mask was set to zero, and the 95th percentile was set to one.

Two dimensional image patches (smaller subimages of the original image) were sampled within an available brain mask[37] at corresponding locations on both acquisitions for 4 datasets; a training set, a training-validation set, a validation set, and a test set. For the training set, one million transversal image patches (15x15 voxels) were sampled from images of all but 10 patients without brain infarcts. The remaining 10 patients without brain infarcts were used for the training-validation set, which was used to assess potential overfitting of the network on the training set. For the training-validation set, 100.000 image patches were randomly sampled. The patches for the training and training-validation set were augmented at each training epoch, by performing random horizontal and vertical flips of the image patches.

The performance of our method on the detection of brain infarcts was evaluated on the validation and test set. The validation set, which was used to evaluate several model design choices consisted of 45 randomly selected patients with brain infarcts. The remainder (225) was included in the test set, on which the final network performance was evaluated. In the validation and test sets, 93, and 553 brain infarcts were present, with a median volume of 0.4 ml (range: 0.072–282 ml) and 0.44 ml (range: 0.036–156 ml), respectively. For these sets, the entire brain was sampled, using a stride of 4 voxels.

NETWORK ARCHITECTURE

We implemented a neural network architecture based on the GANomaly architecture in PyTorch v1.1.022,[38] which ran on the GPU of a standard workstation (Intel Xeon E-1650v3, 32gb RAM, Nvidia Titan Xp). The neural network (Figure 3) consisted of a generator (bottom half) and discriminator (top half). The input of the network features two input channels, for both the T1-weighted and the T2-FLAIR image patches. The generator and discriminator consisted of encoder and decoder parts, that each contained three sequential (transposed) convolutional layers, interleaved with (leaky) rectified linear unit (ReLU) activation and batch normalization. The generator was trained to encode the input image patches x into latent representations: z and $\hat{z}$. Additionally, the generator was trained to realistically reconstruct the input images from the latent vector z into the reconstructed image $\hat{x}$. The discriminator was used to help the generator create realistic reconstructions $\hat{x}$. The latent representations z and $\hat{z}$ were used to calculate an anomaly score per image patch.

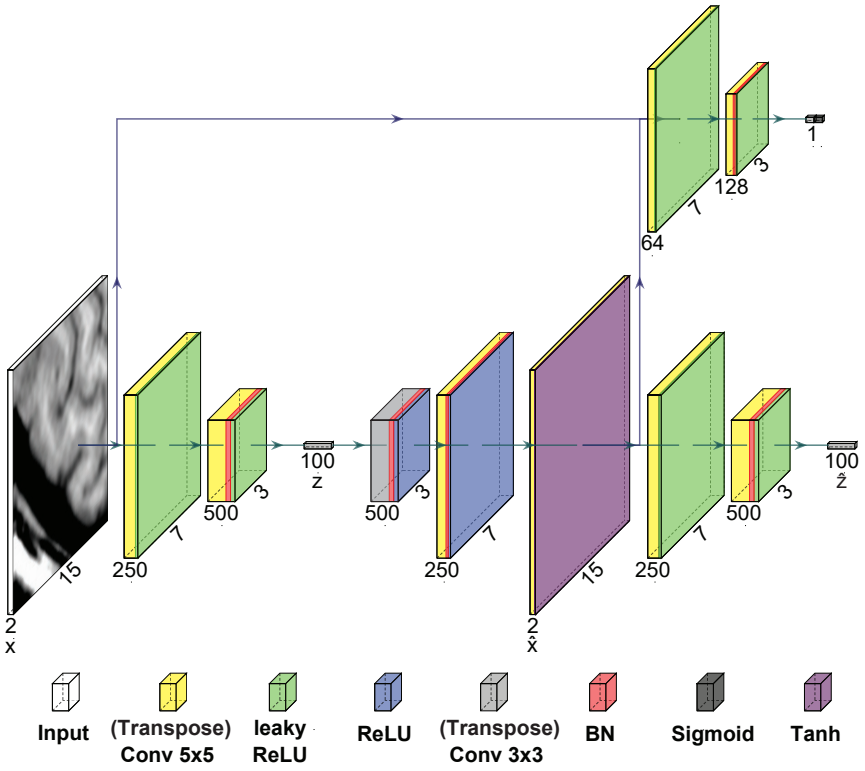

Figure 3. Neural network architecture, visualized using adapted software of PlotNeuralNet.[39] The tensor size after each operation is given by the numbers around each box. The input images are encoded into a latent space z. From the latent space a reconstruction $\hat{x}$ of the input x is created. A final encoding of $\hat{x}$ to $\hat{z}$ is computed. A discriminator, featured in the top of the image, is fed with images x and $\hat{x}$, where the output of the first to last layer is used for the calculation of the adversarial loss L_{adv}. Similarly, a reconstruction loss L_{con} is calculated as the mean difference between x and $\hat{x}$, and an encoding loss L_{enc} is calculated as the L2 loss between z and $\hat{z}$. The (transposed) conv 5x5 layers are applied with a stride of 2 and padding of 1, and are in almost all steps followed by batch normalization (BN). The conv 3x3 layer is applied with a stride of 1 and padding equal to 0. The leaky rectified linear unit (ReLU) activation has a negative slope equal to 0.2.

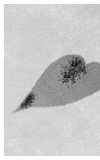

During training of the generator, three error terms were minimized. First, the reconstruction error was computed as the mean difference between the input image and reconstructed image ($L_{con} = ||x - \hat{x}||_1$). Second, the encoding error was given by the L2 loss between the latent space vectors z and $\hat{z}$ ($L_{enc} = ||z - \hat{z}||_2$). Last, the adversarial loss was computed as the L2 loss between the features from first to last layer of the discriminator, given the input image and reconstructed image ($L_{adv} = ||f(x) - f(\hat{x})||_2$). To balance the optimization

of the network, the generator loss was computed as a weighted combination of the aforementioned losses, with weights of 70, 10, and 1 for L_{con}, L_{enc}, and L_{adv}, respectively.

For the discriminator, two error terms were minimized during training.[40] The first term, is given by the binary cross entropy of the input images and the label of the reconstructed images, and the second term is given by the binary cross entropy of the reconstructed images and the label of the input images. To prevent vanishing gradients in the discriminator, a soft labeling method was chosen, where labels for the reconstructed and input images were uniformly chosen between 0 and 0.2, and between 0.8 and 1, respectively.

The network was trained using the training image patches, which were fed to the network in minibatches of size 64. A learning rate of 0.001 was used, with Adam as optimizer.[41] Training continued until the generator loss on the training-validation set did not decrease any further for 10 epochs. The network weights, for the epoch with the lowest generator loss were used for testing.

ANOMALY SCORING

An anomaly score was calculated per image patch as the modified Z-score, a measure of how many median absolute deviations a value lies away from a median value. During training, a median and median absolute deviation were calculated per element of the difference vector $z-\hat{z}$, over all training image patches. These values were used to calculate the modified Z-score for all of the difference vector elements of the validation/test image patches. The anomaly score for each image patch was calculated by taking the N^{th} percentile of modified Z-score values over all vector elements. The value of the percentile was determined in the first experiment.

The anomaly scores over all image patches were projected back onto the original brain image, where areas with an anomaly score larger than 3 were flagged as suspected anomalies. Spurious activation, where only a single isolated patch had an anomaly score larger than 3, were filtered out from the final result.

EXPERIMENTS

LATENT VECTOR SIZE AND ANOMALY SCORE CALCULATION

We investigated the effect of the size of the latent vectors z and $\hat{z}$ (Figure 3), and the effect of the anomaly score calculation on the detection of brain infarcts. We trained several neural network instances with a varying latent vector size, namely: 50, 75, 100, 150, 200, 300, and 400 vector elements. Additionally, we varied the used percentile N for the anomaly score calculation between 10 and 75, in steps of 5 percentage points. For both parameters, we computed the sensitivity and the average number of suspected anomalies per image, as well as the volume fraction of the detected brain infarcts compared to the total brain infarct volume.

SUSPECTED ANOMALY CLASSIFICATION

We used the optimal parameters to evaluate the performance of our proposed method on the test set. We computed the sensitivity and the average number of suspected anomalies per image. In addition, we analyzed the origin of the remaining suspected anomalies, where a neuroradiologist with more than 10 years of experience (J.W. Dankbaar), classified these suspected anomalies as one of 7 classes, namely: normal tissue, unannotated brain infarct, white matter hyperintensity, blood vessel, calcification, bone and image artifact.

MISSED BRAIN INFARCTS

We investigated why our proposed method missed some brain infarcts by evaluating the volume and location of these missed brain infarcts. Additionally, we performed a nearest neighbor analysis, in which we analyzed which training image patches were similar to the test image patches with missed brain infarcts.

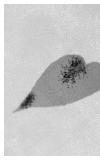

RESULTS

LATENT VECTOR SIZE AND ANOMALY SCORE CALCULATION

Based on the validation set, a latent vector size of 100 showed the highest sensitivity and detected brain infarct volume fraction for the same number of suspected anomalies over almost the entire range, compared to all other latent vector sizes (Figure 4). Similarly, using the 50th percentile yielded an optimal trade-off between sensitivity and fraction of detected brain infarct volume against the number of suspected anomalies. Given our validation dataset, the optimal parameters for the detection of brain infarcts include the use of the 50th percentile with a latent vector size of 100.

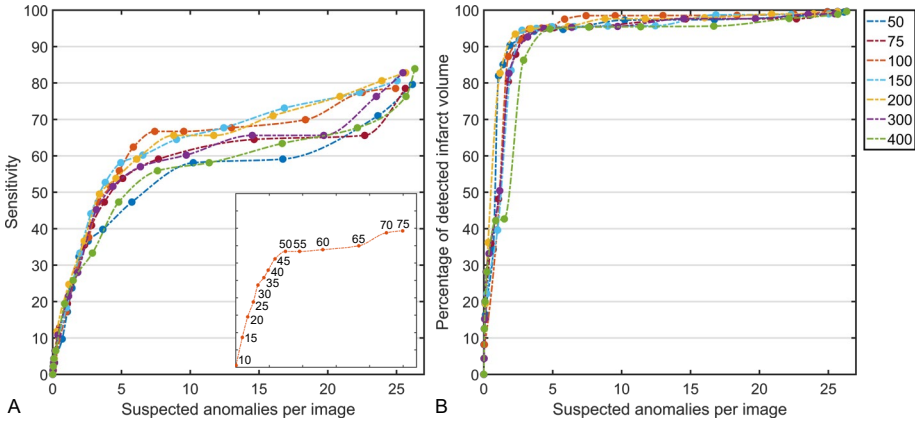

Figure 4. Brain infarct detection performance for various latent vector sizes and percentile values N, used in the anomaly score calculation. (A) Free Response Operator Curve for all latent vector sizes and (B) detected brain infarct volume to total brain infarct volume ratio (given in color). The used percentile ranged between 10 and 75, where for all lines the first datapoint on the left corresponds to 10th percentile, and the right corresponds to the 75th percentile. The inset in (A) shows the used percentiles for a latent vector size of 100. The highest sensitivity for the lowest number of suspected anomalies per image (68% and 6) is given by a latent vector size of 100 and a percentile of 50.

SUSPECTED ANOMALY CLASSIFICATION

We used the optimal parameters to evaluate the performance of our proposed method on the test set, on which our proposed method found on average 9 suspected anomalies per image (total: 1953, examples are given in Figure 5). In total, 374 out of 553 brain infarcts were detected by our model (sensitivity: 68%), representing 19.2% of all suspected anomalies (Table 2). These detected brain infarcts represented 97.5% of the total brain infarct volume. Eight hundred and sixty-five (44.3%) suspected anomalies were caused by white matter hyperintensities. Image artifacts, e.g. due to patient motion, attributed to 115 (5.9%) of all suspected anomalies. Normal healthy tissue was accountable for 563 (28.8%) of all suspected anomalies. In most cases, these normal tissue false positives were located at tissue–cerebrospinal fluid boundaries. Most interestingly, 26 (1.3%) of all suspected anomalies corresponded to unannotated brain infarcts, which were oftentimes located in the cerebellum and the most cranial image slices.

Table 2. Suspected anomaly categories in the 225 test subjects (Total: 1953. On average: 9 suspected anomalies per image). The suspected anomalies were categorized in 8 categories, where the categorization was performed manually by a trained radiologist, except for the 'annotated brain infarcts' (these annotations were already available from the used image dataset).

Suspected anomaly category	Count (Percentage)
White matter hyperintensity	864 (44.3)
Normal tissue	563 (28.8)
Annotated brain infarcts	374 (19.2)
Image artifact	115 (5.9)
Unannotated brain infarct	26 (1.3)
Blood vessel	6 (0.3)
Calcification	2 (0.1)
Bone	2 (0.1)

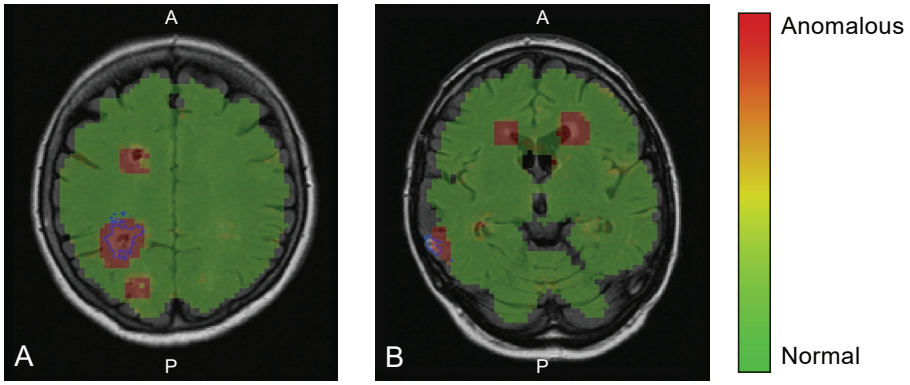

Figure 5. Anomaly score overlay maps on transversal image slices (T2-FLAIR images). A red color indicates an anomaly score ≥ 3, an anomalous location, where green and yellow an anomaly score < 3, normal tissue. The manually annotated brain infarcts are given by the blue outlines. An unannotated brain infarct located in a cranial slice can be observed in (A), anterior ('A') of the annotated brain infarct. The anomaly at the posterior ('P') side of the brain in (A) is only delineated as brain infarct in a subsequent image slice. (B) Detected cortical brain infarct, and two other suspected anomalous locations, caused by white matter hyperintensities at the horn of the ventricles.

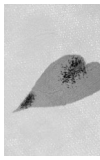

MISSED BRAIN INFARCTS

We performed an additional experiment to better understand why our proposed method missed 179 small brain infarcts (2.5% of the total brain infarct volume). Volume analysis revealed that the missed brain infarcts were in almost all cases smaller than 1 ml (median volume = 0.23 ml). Almost half of the missed brain infarcts (75) were located near the ventricles, at the level of the basal ganglia. Twenty-three missed brain infarcts were present in the

cerebellum and 26 in the brain stem. The remaining 55 brain infarcts were located in the cerebral cortex. Automated analysis, where we used a nearest neighbor algorithm to determine which training image patches were similar to the missed brain infarct image patches, revealed that missed brain infarct image patches were oftentimes closely related to training image patches that contained sulci or tissue–cerebrospinal fluid boundaries (see Figure 6). Furthermore, missed brain infarcts in the brainstem were mostly linked to training image patches in the cortical region, and image patches in the brainstem that border on the cerebrospinal fluid looked similar to cortical image patches with cerebrospinal fluid.

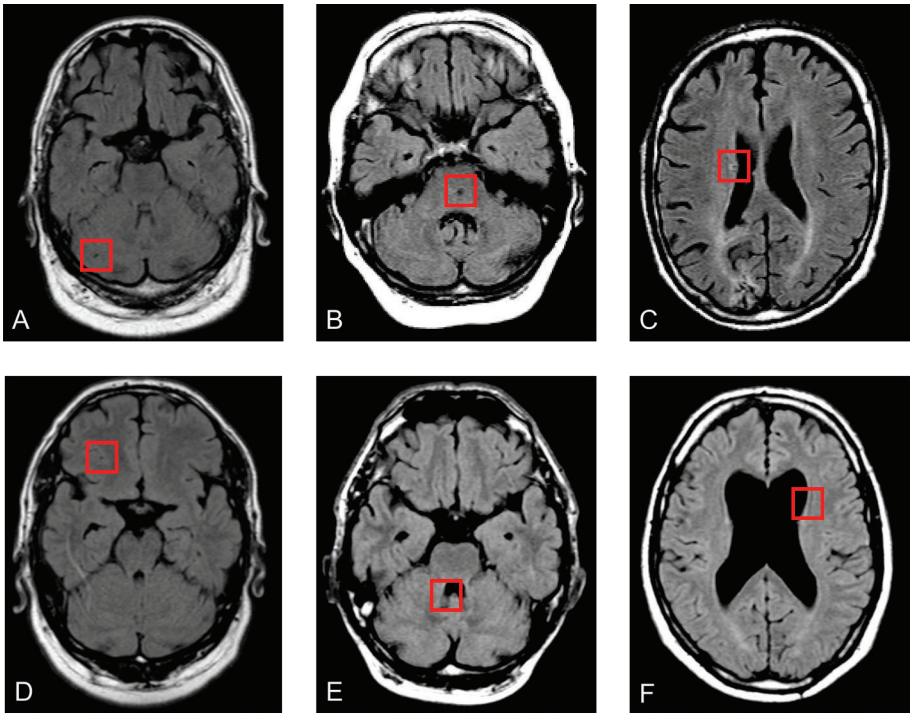

Figure 6. Comparison between missed brain infarcts and nearest neighbor locations in training images. (A, B, and C) Missed brain infarcts indicated by the red square in the cerebellum, brainstem and cerebrum, respectively, on transversal T2-FLAIR images. (D, E, and F) the corresponding nearest neighbor locations in training data matching (A, B, and C) respectively. The square in (D) contains a part of a normal sulcus that has a similar appearance as the missed brain infarct in the cerebellum in (B).

DISCUSSION

In this paper, we proposed an anomaly detection method for the detection of chronic brain infarcts on brain MR images. Our proposed method detected brain infarcts that accounted for 97.5% of the total brain infarct volume of 225 patients. The missed brain infarcts had in most cases a volume smaller than 1 ml, and were mostly located in the brain stem, and cerebellum, and next to the ventricles. White matter hyperintensities, anomalous calcifications, and imaging artifacts accounted for 44.3%, 0.1%, and 5.9% of suspected anomalies, respectively. Additionally, our proposed method identified additional brain infarcts, which were previously missed by the radiologist during radiological reading (1.3% of all suspected anomalies).

Our proposed method properly evaluated regions that are more easily overlooked by a trained radiologist, given the additional brain infarcts that our method found. The percentage of unannotated brain infarcts that our proposed method found (5% of all brain infarcts) is in accordance with literature, which suggest that reading errors occur in 3–5% of the cases in day-to-day radiological practice. These errors can occur because of an inattentional bias, where radiologists are focused on the center of an image, while overlooking findings at the edges of the acquired image.[3] As workload in radiology is ever increasing due to a larger load of radiological images to be assessed, it is even more easy to overlook brain pathologies.[42] Our presented automated analysis method can potentially alleviate part of this assessment by suggesting anomalous areas for the radiologist to look at, or guiding the radiologist to potentially overlooked brain areas.

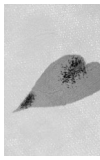

Besides suggesting anomalous areas during assessment of the scans by a radiologist, anomaly detection can also be used during image acquisition. In case of an important suspected pathology, this information can then instantly be used to make changes to the acquisition protocol by relocating the field of view or by adding an acquisition that is important for subsequent analysis of the suspected pathology.

Cerebral small vessel disease is a disease with multiple manifestations on MR images. Our proposed method has shown that it can detect at least two of these manifestations, namely chronic brain infarcts—including cortical infarcts, lacunar infarcts, large subcortical infarct, and infratentorial infarcts—and anomalous white matter hyperintensities. This is in contrast to other

methods,[6,43] that are only trained for the detection of a single homogeneous type of brain pathology. Similarly, other heterogeneous brain pathologies such as brain tumors, or other manifestations of cerebral small vessel disease can also likely be detected using anomaly detection.

Anomaly detection, which is already used for several years in various fields, such as banking, aerospace, IT, and the manufacturing industry, can also be further explored in the medical imaging field. Potential other applications of anomaly detection include the detection of lung nodules on chest CT images, anomalous regions in the retina, breast cancer in mammograms, calcifications in breast MRI, liver tumor metastasis, or for the detection of areas with low fiber tract integrity in diffusion tensor imaging.[25,44–47] Also for the detection of artifacts in MR spectroscopy or the detection of motion artifacts in MR images, anomaly detection can potentially be beneficial.[48,49] For example, by analyzing the acquired k-space data on motion artifacts during patient scanning, a decision can be made more quickly to redo (parts of) the acquisition.

In future work, the use of 2.5D or 3D contextual information can potentially mitigate problems related to the interpretation of small brain infarcts. This is preferably done with MR images with an isotropic voxel size. This approach would mimic the behavior of human readers who also use contextual information, by scrolling through images, when reading an image. Additional to the performance improvement on small brain infarcts, false positive detections of normal tissue can potentially be mitigated by adding contextual information.

Our method has several limitations. First, its performance on brain infarcts smaller than 1 ml is limited. The detection of small lesions is a common problem that is also present in other medical image analysis applications.[50–53] Performance of detection of small lesions is expected to improve with more up-to-date scanning protocols, which likely have a higher signal-to-noise ratio and/or higher spatial resolution. It has recently become possible to identify microinfarcts on 7T and 3T MRI.[54] Additionally, other network architectures might be investigated. Our current architecture seems to predominantly find large anomalies with a relatively large contrast difference compared to the surrounding brain tissue. Other approaches (e.g. a recurrent convolutional neural network[51]) might be able to put more emphasis on finding smaller anomalies with a lower contrast compared to the background.

Design choices on the neural network architecture were made based on its performance on the validation set that included some brain infarcts. This does not reflect complete anomaly detection, where anomalies should be completely unknown. However, such an approach is unfeasible in normal practice. Other anomaly detection methods have also used validation sets to tune hyperparameters.[55–57] The use of our validation dataset had no influence on the training of the network, because the network weights of the training epoch with the lowest training-validation loss were used, as opposed to using the network weights of the training epoch with the best brain infarct detection performance on the validation set.

Anomaly detection commonly does not involve classification of anomalies, but only their localization. In case classification is needed, automated methods or manual inspection should be performed after analysis by our proposed method. We envision a workflow in radiology routine where anomaly detection locates possible lesions, a secondary system classifies these lesions or labels them as 'unknown', and finally presents the results to a radiologist for inspection.

The method was developed and evaluated on data from a single cohort study. The performance on scans that are acquired on other scanners, from other vendors, and on different field strengths is therefore unknown and a topic of future work. The method could be made applicable to other scanners by partial or full retraining, or by applying transfer learning techniques. In the latter case, a relatively small new dataset might be needed.

Lastly, our training set potentially contains unannotated brain infarcts similar to the test set, in which, 5% additional brain infarcts were detected. The potential effect of abnormalities being present in the training data on the final detection performance is likely to be low. The training will be dominated by numerous image patches from normal appearing brain tissue and any abnormalities will therefore have a minimal impact on the anomaly score calculation.

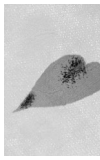

In conclusion, we developed an anomaly detection model for the purpose of detecting chronic brain infarcts on MR images, where our method recovered 97.5% of the total brain infarct volume. Additionally, we showed that our proposed method also finds additional brain abnormalities, some of which were missed by the radiologist. This supports the use of anomaly detection as automated tool for computer aided image analysis.

REFERENCES

1. Hagens MHJ, Burggraaff J, Kilsdonk ID, et al. Impact of 3 Tesla MRI on interobserver agreement in clinically isolated syndrome: A MAGNIMS multicentre study. Mult Scler J. 2019;25:352-360.

2. Geurts BHJ, Andriessen TMJC, Goraj BM, Vos PE. The reliability of magnetic resonance imaging in traumatic brain injury lesion detection. Brain Inj. 2012;26:1439-1450.

3. Busby LP, Courtier JL, Glastonbury CM. Bias in Radiology: The How and Why of Misses and Misinterpretations. RadioGraphics. 2018;38:236-247.

4. Brady AP. Error and discrepancy in radiology: inevitable or avoidable? Insights Imaging. 2017;8:171-182.

5. Lee CS, Nagy PG, Weaver SJ, Newman-Toker DE. Cognitive and system factors contributing to diagnostic errors in radiology. Am J Roentgenol. 2013;201:611-617.

6. Guerrero R, Qin C, Oktay O, et al. White matter hyperintensity and stroke lesion segmentation and differentiation using convolutional neural networks. NeuroImage Clin. 2018;17:918-934.

7. Atlason HE, Love A, Sigurdsson S, Gudnason V, Ellingsen LM. SegAE: Unsupervised white matter lesion segmentation from brain MRIs using a CNN autoencoder. NeuroImage Clin. 2019;24:102085.

8. Gabr RE, Coronado I, Robinson M, et al. Brain and lesion segmentation in multiple sclerosis using fully convolutional neural networks: A large-scale study. Mult Scler J. 2020;26:1217-1226.

9. Devine J, Sahgal A, Karam I, Martel AL. Automated metastatic brain lesion detection: a computer aided diagnostic and clinical research tool. In: Tourassi GD, Armato SG, eds. Medical Imaging 2016: Computer-Aided Diagnosis. Vol 9785. International Society for Optics and Photonics; 2016:97852K.

10. van Wijnen KMH, Dubost F, Yilmaz P, et al. Automated Lesion Detection by Regressing Intensity-Based Distance with a Neural Network. In: Shen D, Liu T, Peters TM, et al., eds. Medical Image Computing and Computer Assisted Intervention -- MICCAI 2019. Vol 11767. Cham: Springer Verlag; 2019:234-242.

11. Ain Q, Mehmood I, Naqi SM, Jaffar MA. Bayesian Classification Using DCT Features for Brain Tumor Detection. In: Setchi R, Jordanov I, Howlett RJ, Jain LC, eds. Knowledge-Based and Intelligent Information and Engineering Systems. KES 2010. Lecture Notes in Computer Science. Vol 6276. Berlin, Heidelberg: Springer; 2010:340-349.

12. Shen S, Szameitat AJ, Sterr A. Detection of infarct lesions from single MRI modality using inconsistency between voxel intensity and spatial location - A 3-D automatic approach. IEEE Trans Inf Technol Biomed. 2008;12:532-540.

13. Cabezas M, Oliver A, Roura E, et al. Automatic multiple sclerosis lesion detection in brain MRI by FLAIR thresholding. Comput Methods Programs Biomed. 2014;115:147-161.

14. Wardlaw JM, Smith EE, Biessels GJ, et al. Neuroimaging standards for research into small vessel disease and its contribution to ageing and neurodegeneration. Lancet Neurol. 2013;12:822-838.

15. Pantoni L. Cerebral small vessel disease: from pathogenesis and clinical characteristics to therapeutic challenges. Lancet Neurol. 2010;9:689-701.

16. Pimentel MAF, Clifton DA, Clifton L, Tarassenko L. A review of novelty detection. Signal Processing. 2014;99:215-249.

17. Chandola V, Banerjee A, Kumar V. Anomaly detection. ACM Comput Surv. 2009;41:1-58.

18. Phua C, Alahakoon D, Lee V. Minority report in fraud detection. ACM SIGKDD Explor Newsl. 2004;6:50-59.

19. Jyothsna V, Rama Prasad VV, Munivara Prasad K. A Review of Anomaly based Intrusion Detection Systems. Int J Comput Appl. 2011;28:26-35.

20. Clifton DA, Bannister PR, Tarassenko L. A Framework for Novelty Detection in Jet Engine Vibration Data. Key Eng Mater. 2007;347:305-310.

21. Lemos AP, Tierra-Criollo CJ, Caminhas WM. ECG Anomalies Identification Using a Time Series Novelty Detection Technique. In: Müller-Karger C, Wong S, La Cruz A, eds. IFMBE Proceedings. Vol 18. Berlin, Heidelberg: Springer Verlag; 2007:65-68.

22. Akcay S, Atapour-Abarghouei A, Breckon TP. GANomaly: Semi-Supervised Anomaly Detection via Adversarial Training. May 2018. Available at: http://arxiv.org/abs/1805.06725. Accessed January 14, 2020.

23. Kim D, Kang P, Cho S, Lee H, Doh S. Machine learning-based novelty detection for faulty wafer detection in semiconductor manufacturing. Expert Syst Appl. 2012;39:4075-4083.

24. Schlegl T, Seeböck P, Waldstein SM, Schmidt-Erfurth U, Langs G. Unsupervised anomaly detection with generative adversarial networks to guide marker discovery. In: Lecture Notes in Computer Science (Including Subseries Lecture Notes in Artificial Intelligence and Lecture Notes in Bioinformatics). Vol 10265 LNCS. Cham: Springer Verlag; 2017:146-147.

25. Schlegl T, Seeböck P, Waldstein SM, Langs G, Schmidt-Erfurth U. f-AnoGAN: Fast unsupervised anomaly detection with generative adversarial networks. Med Image Anal. 2019;54:30-44.

26. Chen X, Konukoglu E. Unsupervised Detection of Lesions in Brain MRI using constrained adversarial auto-encoders. June 2018. Available at: http://arxiv.org/abs/1806.04972. Accessed November 7, 2019.

27. Sun L, Wang J, Huang Y, Ding X, Greenspan H, Paisley J. An Adversarial Learning Approach to Medical Image Synthesis for Lesion Detection. IEEE J Biomed Heal Informatics. 2020;24:2303-2314.

28. Alex V, Safwan K. P. M, Chennamsetty SS, Krishnamurthi G. Generative adversarial networks for brain lesion detection. In: Styner MA, Angelini ED, eds. Medical Imaging 2017: Image Processing. Bellingham, WA: International Society for Optics and Photonics; 2017:101330G.

29. Bowles C, Qin C, Guerrero R, et al. Brain lesion segmentation through image synthesis and outlier detection. NeuroImage Clin. 2017;16:643-658.

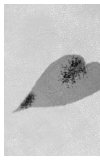

30. Kuijf HJ, Moeskops P, de Vos BD, et al. Supervised novelty detection in brain tissue classification with an application to white matter hyperintensities. In: Styner MA, Angelini ED, eds. Medical Imaging 2016: Image Processing. Vol 9784. Bellingham, WA: International Society for Optics and Photonics; 2016:978421.

31. Baur C, Wiestler B, Albarqouni S, Navab N. Deep Autoencoding Models for Unsupervised Anomaly Segmentation in Brain MR Images. In: Crimi A, Bakas S, Kuijf H, Keyvan F, Reyes M, van Walsum T, eds. Lecture Notes in Computer Science (Including Subseries Lecture Notes in Artificial Intelligence and Lecture Notes in Bioinformatics). Vol 11383 LNCS. Cham: Springer Verlag; 2019:161-169.

32. Baur C, Graf R, Wiestler B, Albarqouni S, Navab N. SteGANomaly: Inhibiting CycleGAN Steganography for Unsupervised Anomaly Detection in Brain MRI. In: Martel AL, Joskowicz PA, Stoyanov D, et al., eds. Lecture Notes in Computer Science (Including Subseries Lecture Notes in Artificial Intelligence and Lecture Notes in Bioinformatics). Vol 12262 LNCS. Cham: Springer Science and Business Media Deutschland GmbH; 2020:718-727.

33. van Veluw SJ, Shih AY, Smith EE, et al. Detection, risk factors, and functional consequences of cerebral microinfarcts. Lancet Neurol. 2017;16:730-740.

34. Saczynski JS, Sigurdsson S, Jonsdottir MK, et al. Cerebral Infarcts and Cognitive Performance. Stroke. 2009;40:677-682.

35. Geerlings MI, Appelman APA, Vincken KL, et al. Brain volumes and cerebrovascular lesions on MRI in patients with atherosclerotic disease. The SMART-MR study. Atherosclerosis. 2010;210:130-136.

36. Tustison NJ, Avants BB, Cook PA, et al. N4ITK: Improved N3 Bias Correction. IEEE Trans Med Imaging. 2010;29:1310-1320.

37. Anbeek P, Vincken KL, van Bochove GS, van Osch MJP, van der Grond J. Probabilistic segmentation of brain tissue in MR imaging. Neuroimage. 2005;27:795-804.

38. Paszke A, Gross S, Massa F, et al. PyTorch: An Imperative Style, High-Performance Deep Learning Library. In: Wallach H, Larochelle H, Beygelzimer A, D'Alché-Buc F, Fox E, Garnett R, eds. Advances in Neural Information Processing Systems 32. New York, New York: Curran Associates, Inc.; 2019:8024-8035.

39. Iqbal H. HarisIqbal88/PlotNeuralNet v1.0.0. Available at: http://doi.org/10.5281/zenodo.2526396. Accessed February 19, 2020.

40. Goodfellow IJ, Pouget-Abadie J, Mirza M, et al. GAN (Generative Adversarial Nets). J Japan Soc Fuzzy Theory Intell Informatics. 2017;29:177-177.

41. Kingma DP, Ba J. Adam: A Method for Stochastic Optimization. In: Lehman J, Stanley KO, eds. Proceedings of the 12th Annual Conference on Genetic and Evolutionary Computation. New York: ACM Press; 2014:103-110.

42. McDonald RJ, Schwartz KM, Eckel LJ, et al. The Effects of Changes in Utilization and Technological Advancements of Cross-Sectional Imaging on Radiologist Workload. Acad Radiol. 2015;22:1191-1198.

43. Guo D, Fridriksson J, Fillmore P, et al. Automated lesion detection on MRI scans using combined unsupervised and supervised methods. BMC Med Imaging. 2015;15:50.

44. Zhang X, Sun Y, Li W, et al. Characterization of white matter changes along fibers by automated fiber quantification in the early stages of Alzheimer's disease. NeuroImage Clin. 2019;22:101723.

45. Wang J, Ding H, Bidgoli FA, et al. Detecting Cardiovascular Disease from Mammograms with Deep Learning. IEEE Trans Med Imaging. 2017;36:1172-1181.

46. Ouardini K, Yang H, Unnikrishnan B, et al. Towards Practical Unsupervised Anomaly Detection on Retinal Images. In: Wang Q, Milletari F, Nguyen H V., et al., eds. Domain Adaptation and Representation Transfer and Medical Image Learning with Less Labels and Imperfect Data. Vol 11795. Cham: Springer Verlag; 2019:225-234.

47. Tarassenko L, Hayton P, Cerneaz N, Brady M. Novelty detection for the identification of masses in mammograms. In: 4th International Conference on Artificial Neural Networks. Vol 1995. IET; 1995:442-447.

48. Kyathanahally SP, Döring A, Kreis R. Deep learning approaches for detection and removal of ghosting artifacts in MR spectroscopy. Magn Reson Med. 2018;80:851-863.

49. Küstner T, Liebgott A, Mauch L, et al. Automated reference-free detection of motion artifacts in magnetic resonance images. Magn Reson Mater Physics, Biol Med. 2018;31:243-256.

50. Kuijf HJ, Casamitjana A, Collins DL, et al. Standardized Assessment of Automatic Segmentation of White Matter Hyperintensities and Results of the WMH Segmentation Challenge. IEEE Trans Med Imaging. 2019;38:2556-2568.

51. Sudre CH, Gomez Anson B, Lane CD, et al. 3D multirater RCNN for multimodal multiclass detection and characterisation of extremely small objects. In: Jorge Cardoso M, Feragen A, Glocker B, et al., eds. Proceedings of Machine Learning Research. Vol 102. London: PMLR; 2019:447-456.

52. Ngo D-K, Tran M-T, Kim S-H, Yang H-J, Lee G-S. Multi-Task Learning for Small Brain Tumor Segmentation from MRI. Appl Sci. 2020;10:7790.

53. Binczyk F, Stjelties B, Weber C, et al. MiMSeg - an algorithm for automated detection of tumor tissue on NMR apparent diffusion coefficient maps. Inf Sci (Ny). 2017;384:235-248.

54. van Veluw SJ, Biessels GJ, Luijten PR, Zwanenburg JJM. Assessing Cortical Cerebral Microinfarcts on High Resolution MR Images. J Vis Exp. 2015;2015.

55. Atlason HE, Love A, Sigurdsson S, Gudnason V, Ellingsen LM. Unsupervised brain lesion segmentation from MRI using a convolutional autoencoder. November 2018. Available at: http://arxiv.org/abs/1811.09655. Accessed May 23, 2019.

56. Vasilev A, Golkov V, Meissner M, et al. q-Space Novelty Detection with Variational Autoencoders. June 2018. Available at: http://arxiv.org/abs/1806.02997. Accessed March 3, 2020.

57. Alaverdyan Z, Jung J, Bouet R, Lartizien C. Regularized siamese neural network for unsupervised outlier detection on brain multiparametric magnetic resonance imaging: Application to epilepsy lesion screening. Med Image Anal. 2020;60:101618.

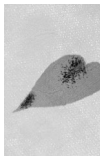

CHAPTER 7

Summary and general discussion

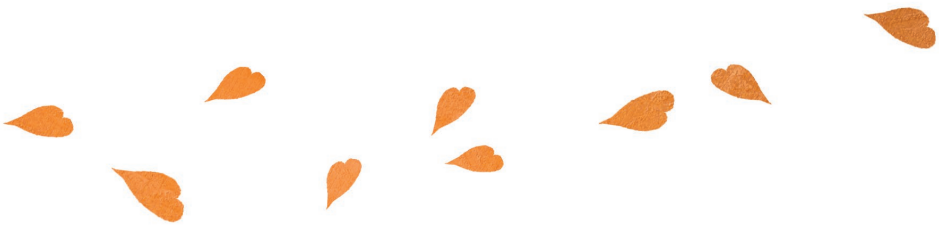

SUMMARY

Cerebrovascular disease results in morphological and functional alterations in the intracranial macro- and microvasculature. Early detection of such alterations is key for better understanding of cerebrovascular disease mechanisms, and in taking preventative measures against cerebrovascular disease development. In this thesis, we aimed to quantify alterations in the vessel walls, brain parenchyma, and blood flow using both high-resolution post-mortem 7T magnetic resonance imaging (MRI), histopathological analysis, and in vivo MRI in volunteers, and in patients with a history of cerebrovascular disease.

High-resolution post-mortem 7T MRI and histopathological analysis of circle of Willis specimens was performed in **Chapter 2**, where we investigated arterial remodeling caused by hypertension. We observed no significant differences in vessel wall area and thickness, between hypertensive patients and normotensive controls. Histological analysis showed early and advanced atherosclerotic plaques for almost all vessels of the circle of Willis for both groups. The collagen to smooth muscle ratio, as a measure for arterial stiffness, was significantly higher for the internal carotid artery in the hypertensive group.

In **Chapter 3**, we investigated the limitations of vessel wall MRI regarding the accuracy of vessel wall thickness measurements. Using high-field 7T MRI of post-mortem circle of Willis specimens, we have shown that accurate vessel wall thickness measurements, using the full-width-half-maximum measurement method, are possible for vessel walls with a thickness larger than 1.25 times the acquired voxel size. For thinner vessel walls, measurements were ambiguous and inaccurate. Because the vessel wall for all arteries of the circle of Willis is thinner than the acquired voxel size, early vessel wall thickening cannot be quantified from vessel wall images acquired with commonly used in vivo MR sequences.

Using the vessel wall image intensity allows for measurements for vessel walls thinner than the acquired voxel size (**Chapter 4**). However, such measurements are uncalibrated and qualitative, and are therefore only usable for visualizing relative differences in vessel wall thickness within a subject. We therefore proposed a neural network architecture, which was quantitative by design, for measuring the subvoxel vessel wall thickness. Hereto, we imaged

post-mortem circle of Willis specimens with a clinically-used sequence, and an ultra-high-resolution sequence. The neural network was trained to measure the vessel thickness from the clinically-used images. Thickness measurements on the ultra-high-resolution image, which were performed prior to training of the network, were used as reference for the network. Results showed that accurate subvoxel vessel wall thickness measurements are possible, and that the method is robust to changes to the input and to changes in the used algorithm. In addition, we showed its feasibility on three in vivo vessel wall MR images of intracranial aneurysms.

In **Chapter 5**, we introduced software that allows for the measurement of the arterial diameter pulsatility and blood flow velocity pulsatility over the cardiac cycle, as measure for the arterial stiffness, from 4D phase contrast (velocity) MR (PC-MRI) images. Measurements on the arterial diameter pulsatility and blood flow velocity pulsatility using our software were validated against measurements from 2D PC-MRI for two locations of the internal carotid artery in 7 volunteers. Our software may potentially aid in identifying changes in arterial stiffness of the intracranial arteries caused by pathological changes to the vessel wall.

Lastly, we investigated the use of anomaly detection for the automated detection of brain pathology (**Chapter 6**). We evaluated the performance of our anomaly detection method on the detection of chronic brain infarcts. Besides the detection of brain infarcts, our proposed method also detected white matter hyperintensities, and image infarcts. Most interestingly, it also detected brain infarcts that were initially missed by the radiologist during radiological reading of the MR images. Anomaly detection is a powerful tool for the detection of brain pathology, and may aid diagnostic radiology by highlighting locations in the image that likely contain pathology.

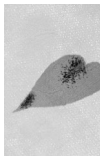

GENERAL DISCUSSION

In recent years, vessel wall imaging has emerged as diagnostic tool for cerebrovascular disease detection. Whereas old methods, such as CT angiography and MR angiography focus on visualizing the lumen of the arteries, vessel wall imaging focuses on visualizing the vessel walls itself. This is a logical development, because vascular pathologies induce changes in the vessel wall, whereas changes to the lumen are only a secondary effect of changes in the vessel wall. Vessel wall imaging has shown clear benefit in the detection of atherosclerosis, dissection and vasculitis.[1,2] When it comes to the quantification of early vessel wall thickening, we have shown that current vessel wall sequences lack resolving power (**Chapter 3**). Qualitative measurements, where the vessel wall intensity was used as measure for vessel wall thickness only allowed for the visualization of relative thickness differences within a single patient (**Chapter 4**).[3] Only in case of severe vessel wall thickening, such as in atherosclerosis, in vivo quantification of vessel wall thickening may be possible. Vessel wall thickness measurement tools based on deep learning algorithms may be usable in the quantification of early vessel wall thickening (**Chapter 4**).

In cases where the effect of disease on vessel wall changes is unknown or minimal, such as in hypertension and Moyamoya, ex vivo imaging may provide insight.[2,4,5] Ex vivo imaging allows for experimentation in a controlled environment, and is a helpful tool for validation of in vivo observations. In MRI, ex vivo imaging allows for longer scan times without motion artifacts. Ex vivo imaging has shown its usability in the visualization of cerebral microinfarcts,[6] the visualization of the cortical layers of the brain,[7] and for determining MR markers in brain diseases, such as vascular lesions and demyelination.[8–10] However, a serious downside of ex vivo imaging is the intrinsic decoupling with the in vivo environment. The formalin fixation of ex vivo specimens is known to alter T1 and T2 relaxation times,[11,12] and results in tissue shrinkage between 8 to 20%.[13] Although ex vivo imaging comes with some limitations, it offers a reference/gold standard for in vivo measurements. Such a reference is especially useful for research on the cerebral vasculature, where its difficult position does not allow for biopsies or reliable validation through other imaging modalities. Imaging modalities such as transcranial Doppler imaging are highly operator dependent, and only allow for visualization of the large basal arteries.[14]

In our case, ex vivo imaging was able to show that conventional vessel wall thickness measurements of the intracranial arteries, i.e. by measuring the inner to outer wall distance, are hugely inaccurate for currently used clinical resolutions (**Chapter 3**). Similar inaccuracy was observed by Antiga et al.[15] in a simulation study, where the effect of image resolution on the accuracy of measured vessel wall thickness was investigated. Clearly, current MRI sequences do not lend themselves for accurate quantification of the vessel wall thickness of the intracranial arteries, which commonly lies between 0.3 and 0.7 mm for the larger arteries.[16] Nonetheless, multiple studies have aimed to quantify vessel wall thickening in various populations, and aimed to use it as comparative measure between patient and control groups.[17–24] Conclusions drawn based on the vessel wall thickness measured with conventional measurement methods, specifically where vessel walls with a thickness around or below the acquired resolution are measured, should therefore be interpreted with caution. It is likely that the partial volume effect introduces more variation in the measurement outcome than potential vessel wall thickening owing to disease will. To conclude, for accurate vessel wall thickness measurements with conventional measurement methods, a high-resolution vessel wall image, where the vessel wall spans at least one and a half image voxels, is vital. If such voxel sizes are not achievable, the used measurement method should at least be validated against ground truth measurements.

In other medical imaging applications, accuracy in thickness measurements is also important. Thickness measurements of the cerebral cortex are performed to assess Alzheimer's disease and to find local atrophy of brain tissue. Even though, in this use case, the cortex spans multiple voxels, deep learning algorithms focused on super resolution can aid in accurately measuring the cortical thickness. Additionally, they can likely provide faster measurements than conventional segmentation based methods that can take 1.5–7 hours to segment a single brain.[25] Deep learning algorithms for automated thickness measurements can also likely be used in knee MRI, where accurate thickness measurements of cartilage are important to identify cartilage degeneration, in for example osteoarthritis, or to monitor therapeutic responses.[26–30] In MR imaging of atherosclerotic plaques of the common carotid arteries, such methods can also be deployed. An important indicator for plaque rupture risk is the thickness of the fibrous cap. Plaques are stable when the thickness of the fibrous cap lies between 0.7 to 2 mm.[31] A vessel wall thinner than 0.7 mm, combined with (a small degree of) luminal stenosis results in a plaque that is

prone to rupture. To properly evaluate this rupture risk, accurate thickness measurements are required.[32]

Besides using the vessel wall thickness as biomarker for early cerebrovascular disease development, other (functional) biomarkers are also useful. 4D phase contrast (velocity) MRI (PC-MRI) as we have shown in **Chapter 5** was used to measure properties of the blood flow. Besides measuring the mean flow, blood velocity and arterial distensibility/lumen area pulsatility, advanced hemodynamic biomarkers can also be measured using 4D PC-MRI. For example, hemodynamic biomarkers that are linked to cerebral aneurysm growth and rupture risk including vorticity, helicity, and wall shear stress can be measured from 4D PC-MRI images.[33,34] Similarly, quantification of wall shear stress can also provide insight in the progression of atherosclerosis.[35] Combined use of hemodynamic (functional) biomarkers and morphological biomarkers of the vessel wall might provide a clearer overview of status of cerebrovascular disease than one type of biomarker individually.

Deep learning algorithms have shown clear advantage over traditional machine learning algorithms, and for specific image processing tasks some well-established types of architectures have been developed.[36] For image segmentation, U-Nets have been developed, in which the image information is compressed into a smaller representation.[37] Similarly, for classification tasks and for image synthesis, convolutional neural networks and cycle-GANs are commonly employed.[36,38] In our case, we employed an architecture implementation by Akcay et al.[39] for anomaly detection, which was initially designed for airport luggage screening. Adopting an architecture that is designed for a similar image processing task will yield an idea of the final performance on the provided task. For a basic task such as segmentation, adaptation of existing architectures will likely be sufficient. For more exotic image processing tasks fine-tuning of hyperparameters and increasing the complexity of the architecture should be able to maximize the performance.

Besides the architecture itself, a few other important things need to be considered for the algorithm to work well. In the first place, data curation, where images are screened on overall quality is important. Supplying the algorithm with examples that are not representative of the general population can hamper its performance. We have seen such examples in **Chapter 3** and **Chapter 4**, where vessels were sometimes severely dissected or contained air, caused by post-mortem extraction. In an ultra-high-resolution image

such dissection is easily observable, but can be more difficult to pick up from images taken with an in vivo acquisition, which in our case resulted in an overestimation of the vessel wall thickness. Similarly, air pockets are not present in the in vivo vessel lumen. For this reason, we removed the arteries with severe dissection and air pockets. Additionally, even more than traditional machine learning algorithms, that use human crafted image features, deep learning algorithms are particularly susceptible to learning from hidden variables.[40] They can potentially learn the distribution of the background instead of looking at differences in the foreground, or learn from motion artifacts, which are more likely in ill patients than in more healthy controls.[41] When being aware of these missteps, deep learning is a versatile tool for detection, segmentation and quantification tasks. To conclude, the quality and representativeness of the image data, the ground truth values and the type of architecture used to train a deep learning algorithm are extremely important for its ultimate performance.

Software that performs automated analysis of medical images can provide an important contribution to diagnostic error reduction. Diagnostic errors occur in 3–5% of all diagnosis involving imaging.[42–44] It is assumed that cognitive biases are one of the main contributors to diagnostic errors.[45] However, oftentimes multiple factors contribute to the occurrence of diagnostic errors. For example, systematic causes of error are also a major contributor of diagnostic errors. Systematic causes of error include an increase in workload and understaffing, overburdening policies, software failure, lack of teamwork, or workplace distractions and interruptions. Additionally, the way radiologists are trained, in an apprentice-based training approach, also contribute to errors.[45]

Software for automated analysis of medical images does not suffer from cognitive bias and does not suffer from systematic causes of error. It can, however, be influenced by the way it was trained. Usually these analysis tools are trained on ground truth labels that were created by a radiologist. Biases in the radiologist could propagate to the way analysis tools look at images. This problem can be solved by training an analysis tool on datasets annotated by multiple radiologists, hereby averaging out potential bias. Bias can also be introduced by the way data is intentionally or unintentionally supplied to the algorithm. Besides an effect on general performance as described before, supplying biased data can yield unwanted results. Several commercially available gender classification systems have been shown to discriminate based

on race and gender.[46] These algorithms show poor performance on predictions on dark skinned people compared to light skinned people, and to a certain extent on female gender, because they have been predominantly trained on images of light skinned males. This can lead to serious consequences, when this prediction is used in other tasks, such as in the identification of someone accused of a crime. Similarly, in the classification of skin lesions, biased data can also lead to serious consequences. Using a deep learning algorithm lesion classification performance equaled that of 21 dermatologists.[47] However, the dataset consisted of lesions on mainly Caucasian patients. In non-Caucasian patients, a different group showed that classification performance was significantly lower.[48] Potential biases in data and their labels should be avoided at all costs. The research and radiology communities should set bounds on how we want artificial intelligence algorithms to be developed. We want these algorithms to adhere to certain ethical standards such as the promotion of wellbeing, and the minimization of harm in clinical care. In addition, we need to establish rules on responsibility and accountability. Because of the apparent black box nature of these algorithms, it can be difficult to understand which variables are taken into account for a given algorithm prediction. These predictions could well be based on biased variables. To retain transparency, the control of data versions and uses are critical. In the end, predictions of artificial intelligence algorithms should remain as a second opinion to the radiologist. Steering blind on the predictions of artificial intelligence algorithms is unwanted and will likely and hopefully not be done in the foreseeable future. The radiologist will ultimately remain responsible for patient care.

Besides developing algorithms and software that performs equally as good or better than clinicians, development of artificial intelligence algorithms should also focus on understanding the inner workings of these black box algorithms, to test for and prevent potential biases. There are two major approaches in neural network development that aim to understand the inner workings of these algorithms: feature visualization and saliency maps.[49] Feature visualization methods are focused on directly visualizing the image features that a specific neuron is looking for in an image. This can for example be done by activation maximization, which aims to construct the input of a neuron that maximizes the activation of that neuron. Saliency maps are used to find the parts of an input image that contribute the most to the activation of a given layer/neuron.

FUTURE PROSPECTS

VESSEL WALL IMAGING

For the clinical use of vessel wall thickness measurements in the early detection of cerebrovascular disease progression, several improvements are needed. First, an improvement in image resolution is required. Although measurements were possible using our neural network implementation in **Chapter 4**, an increase in image resolution will likely aid in more accurate vessel wall thickness measurements. There are however no free lunches in MR imaging. An increase in image resolution comes at the cost of an increase in scan time, or at the cost of considerably decreased signal-to-noise-ratio (SNR). Prolonged scan times strain the scan protocol to fit in clinical scan slots, and increases the chance of motion artifacts occurring in the acquired images. In other institutes, vessel wall MR sequences are used that have an acquired spatial resolution of up to 0.5 mm isotropic.[19] Validation studies have to show how feasible these sequences are when implemented in our institute, and whether the SNR of the vessel wall, compared to the surrounding liquids and gray matter, is adequate enough for vessel wall thickness measurements.

To achieve improved spatial resolutions in clinically feasible scan times, several acceleration techniques could be implemented for improved scan times, including SENSE or compressed sensing.[50,51] These methods work by undersampling k-space, and subsequent clever reconstruction of the vessel wall images. Next to the increase in image resolution, an important factor is the signal nulling of cerebrospinal fluid and (slow flowing) blood. When nulling of the signal of these fluids is not perfect, the apparent vessel wall thickness increases.[2,52] In addition, when the signal of the cerebrospinal fluid is not reduced, the vessel wall might visually touch the brain parenchyma. In this case, our neural network implementation (**Chapter 4**) would struggle with accurate measurements of the vessel wall thickness, because it assumes the vessel wall is detached from surrounding tissue. Suppression techniques, such as DANTE and antidriven-equilibrium, are currently developed with the aim to reduce the signal of cerebrospinal fluid and blood.[53,54] Recently, Jia et al.[55] have implemented both compressed sensing and DANTE, for vessel wall imaging at 0.55 mm isotropic resolution in only 5 minutes scan time. Next to changes to the scan protocol and acquisition scheme, hardware improvements in coil design may also contribute to a higher SNR in images, allowing for higher spatial resolutions.[56,57] Increasing the spatial resolution of vessel wall images reduces both SNR and contrast-to-noise ratio. Scanning at a higher field strength can compensate for this loss, because the SNR and

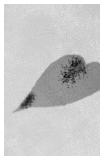

CNR increase intrinsically with an increase in main magnetic field strength. Additionally, scanning at higher field strengths increases the relaxation times of tissue.[58] At higher field strengths, the T2* relaxation time of gray matter becomes more dominant. This effect can potentially be used to increase the contrast between the vessel wall and surrounding brain tissue, aiding in improving the accuracy of vessel wall thickness measurements.

DEEP LEARNING IN THE RADIOLOGICAL WORKFLOW

Deep learning has shown its power and versatility as tool for problem solving in **Chapter 4** and **Chapter 6**, but is no all-in-one solution. Deep learning algorithms are not adept in understanding contextual information. Where radiologists can extrapolate their knowledge when, presented with an MR image with slightly different contrast or resolution, deep learning algorithms are not able to, and need to be retrained to perform well again. However, with the current flight of affordable GPU accelerated computing, such retraining can be performed fast and efficiently. In addition, by applying transfer learning, where an already trained network is reapplied to a different task, oftentimes only few layers of the network need to be retrained, whilst achieving similar performance as complete retraining.[59] Transfer learning requires less training data, and will in the future enable its use in studies where data is limited. This is especially useful in medical imaging where obtaining labeled data is difficult, even though over 900.000 MR images are acquired per year in the Netherlands.[60] For transfer learning to be widely adopted, well documented, well trained algorithms need to be made available.

Annotating and labeling the image data is a laborious and time-consuming effort. Other solutions that aim to circumvent the need for pixelwise annotations of medical images include unsupervised algorithms. These algorithms are fed with unlabeled data. In medical imaging, these algorithms are predominantly involved in the extraction and learning of feature representations of imaging data, which are then fed as a pretraining for a supervised algorithm.[61] Developing more unsupervised algorithms, can aid in the detection, classification and segmentation of more rare pathologies in the near future.

A major step that needs to be taken for deep learning is not necessarily its development, but more its integration in clinical workflow. For example, for anomaly detection it would be beneficial to implement it next to the imaging archive system, where images that are acquired and sent to this archive

are directly read and analyzed by the anomaly detection algorithm. The processed images are sent back to the image archive system, and function as complementary information for the radiologist. In this way we don't change what the radiologists look at, but we suggest areas to inspect. For automated vessel wall thickness measurements directly on acquired images several other steps would be required, including the segmentation of the vessel plus surrounding cerebrospinal fluid, and detection of the vessel wall center. Such measurements will probably require some form of user input, but can potentially be reduced to a minimum. In this way it will not be more complex than tools that are already available in MR image viewers, like calipers used to measure thicknesses of objects in the image. Because the radiological workload is ever increasing, the aid and integration of these automated analysis tools will become more and more important in the near future.

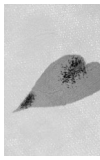

REFERENCES

1. Yu Y-N, Liu M-W, Villablanca JP, et al. Middle Cerebral Artery Plaque Hyperintensity on T2-Weighted Vessel Wall Imaging Is Associated with Ischemic Stroke. Am J Neuroradiol. 2019;40:1886-1892.

2. Mandell DM, Mossa-Basha M, Qiao Y, et al. Intracranial vessel wall MRI: Principles and expert consensus recommendations of the American society of neuroradiology. Am J Neuroradiol. 2017;38:218-229.

3. Kleinloog R, Korkmaz E, Zwanenburg JJM, et al. Visualization of the aneurysm wall: A 7.0-Tesla magnetic resonance imaging study. Neurosurgery. 2014;75:614-622.

4. Mossa-Basha M, de Havenon A, Becker KJ, et al. Added Value of Vessel Wall Magnetic Resonance Imaging in the Differentiation of Moyamoya Vasculopathies in a Non-Asian Cohort. Stroke. 2016;47:1782-1788.

5. Cogswell PM, Lants SK, Davis LT, Juttukonda MR, Fusco MR, Donahue MJ. Vessel Wall and Lumen Features in North American Moyamoya Patients. Clin Neuroradiol. 2020;30:545-552.

6. van Veluw SJ, Zwanenburg JJM, Engelen-Lee J, et al. In vivo detection of cerebral cortical microinfarcts with high-resolution 7T MRI. J Cereb Blood Flow Metab. 2013;33:322-329.

7. Edlow BL, Mareyam A, Horn A, et al. 7 Tesla MRI of the ex vivo human brain at 100 micron resolution. Sci data. 2019;6:244.

8. De Reuck J, Auger F, Cordonnier C, et al. Comparison of 7.0-T T2*-Magnetic Resonance Imaging of Cerebral Bleeds in Post-Mortem Brain Sections of Alzheimer Patients with Their Neuropathological Correlates. Cerebrovasc Dis. 2011;31:511-517.

9. Schmierer K, Parkes HG, So P-W, et al. High field (9.4 Tesla) magnetic resonance imaging of cortical grey matter lesions in multiple sclerosis. Brain. 2010;133:858-867.

10. Gouw AA, Seewann A, Vrenken H, et al. Heterogeneity of white matter hyperintensities in Alzheimer's disease: post-mortem quantitative MRI and neuropathology. Brain. 2008;131:3286-3298.

11. Shatil AS, Uddin MN, Matsuda KM, Figley CR. Quantitative Ex Vivo MRI changes due to progressive formalin fixation in whole human brain specimens: Longitudinal characterization of diffusion, relaxometry, and myelin water fraction measurements at 3T. Front Med. 2018;5:31.

12. Pfefferbaum A, Sullivan E V., Adalsteinsson E, Garrick T, Harper C. Postmortem MR imaging of formalin-fixed human brain. Neuroimage. 2004;21:1585-1595.

13. Tran T, Sundaram CP, Bahler CD, et al. Correcting the shrinkage effects of formalin fixation and tissue processing for renal tumors: Toward standardization of pathological reporting of tumor size. J Cancer. 2015;6:759-766.

14. Karatas A, Coban G, Cinar C, Oran I, Uz A. Assessment of the circle of Willis with cranial tomography angiography. Med Sci Monit. 2015;21:2647-2652.

15. Antiga L, Wasserman BA, Steinman DA. On the overestimation of early wall thickening at the carotid bulb by black blood MRI, with implications for coronary and vulnerable plaque imaging. Magn Reson Med. 2008;60:1020-1028.

16. Harteveld AA, Denswil NP, Van Hecke W, et al. Ex vivo vessel wall thickness measurements of the human circle of Willis using 7T MRI. Atherosclerosis. 2018;273:106-114.

17. Ryu CW, Jahng GH, Kim EJ, Choi WS, Yang DM. High resolution wall and lumen MRI of the middle cerebral arteries at 3 tesla. Cerebrovasc Dis. 2009;27:433-442.

18. Qiao Y, Guallar E, Suri FK, et al. MR Imaging Measures of Intracranial Atherosclerosis in a Population-based Study. Radiology. 2016;280:860-868.

19. Qiao Y, Steinman DA, Qin Q, et al. Intracranial arterial wall imaging using three-dimensional high isotropic resolution black blood MRI at 3.0 Tesla. J Magn Reson Imaging. 2011;34:22-30.

20. Sherif C, Kleinpeter G, Mach G, et al. Evaluation of cerebral aneurysm wall thickness in experimental aneurysms: Comparison of 3T-MR imaging with direct microscopic measurements. Acta Neurochir (Wien). 2014;156:27-34.

21. Underhill HR, Kerwin WS, Hatsukami TS, Yuan C. Automated measurement of mean wall thickness in the common carotid artery by MRI: A comparison to intima-media thickness by B-mode ultrasound. J Magn Reson Imaging. 2006;24:379-387.

22. Yuan M, Liu Z, Wang Z, Li B, Xu L, Xiao X. High-resolution MR imaging of the arterial wall in moyamoya disease. Neurosci Lett. 2015;584:77-82.

23. Park JK, Lee S, Sim KB, Huh JS, Park JC. Imaging of the walls of saccular cerebral aneurysms with double inversion recovery black-blood sequence. J Magn Reson Imaging. 2009;30:1179-1183.

24. Zhang N, Zhang F, Deng Z, et al. 3D whole-brain vessel wall cardiovascular magnetic resonance imaging : a study on the reliability in the quantification of intracranial vessel dimensions. J Cardiovasc Magn Reson. 2018;20:39.

25. Schwarz CG, Gunter JL, Wiste HJ, et al. A large-scale comparison of cortical thickness and volume methods for measuring Alzheimer's disease severity. NeuroImage Clin. 2016;11:802-812.

26. Koo S, Gold GE, Andriacchi TP. Considerations in measuring cartilage thickness using MRI: Factors influencing reproducibility and accuracy. Osteoarthr Cartil. 2005;13:782-789.

27. Wang Y, Wluka AE, Jones G, Ding C, Cicuttini FM. Use magnetic resonance imaging to assess articular cartilage. Ther Adv Musculoskelet Dis. 2012;4:77-97.

28. Fawcett T, Provost F. Activity monitoring. In: Chaudhuri S, Madigan D, eds. Proceedings of the Fifth ACM SIGKDD International Conference on Knowledge Discovery and Data Mining - KDD '99. New York, New York: ACM Press; 1999:53-62. Available at: http://portal.acm.org/citation.cfm?doid=312129.312195.

29. Chaudhari AS, Stevens KJ, Wood JP, et al. Utility of deep learning super-resolution in the context of osteoarthritis MRI biomarkers. J Magn Reson Imaging. 2020;51:768-779.

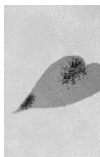

30. Ambellan F, Tack A, Ehlke M, Zachow S. Automated segmentation of knee bone and cartilage combining statistical shape knowledge and convolutional neural networks: Data from the Osteoarthritis Initiative. Med Image Anal. 2019;52:109-118.

31. Li Z-Y, Howarth SPS, Tang T, Gillard JH. How Critical Is Fibrous Cap Thickness to Carotid Plaque Stability? Stroke. 2006;37:1195-1199.

32. Nieuwstadt HA, Geraedts TR, Truijman MTB, et al. Numerical simulations of carotid MRI quantify the accuracy in measuring atherosclerotic plaque components in vivo. Magn Reson Med. 2014;72:188-201.

33. Stankovic Z, Allen BD, Garcia J, Jarvis KB, Markl M. 4D flow imaging with MRI. Cardiovasc Diagn Ther. 2014;4:173-192.

34. Gottwald LM, Töger J, Markenroth Bloch K, et al. High Spatiotemporal Resolution 4D Flow MRI of Intracranial Aneurysms at 7T in 10 Minutes. Am J Neuroradiol. 2020;41:1201-1208.

35. Schnell S, Wu C, Ansari SA. Four-dimensional MRI flow examinations in cerebral and extracerebral vessels – ready for clinical routine? Curr Opin Neurol. 2016;29:419-428.

36. Litjens G, Kooi T, Bejnordi BE, et al. A survey on deep learning in medical image analysis. Med Image Anal. 2017;42:60-88.

37. Ronneberger O, Fischer P, Brox T. U-Net: Convolutional Networks for Biomedical Image Segmentation. In: Lecture Notes in Computer Science (Including Subseries Lecture Notes in Artificial Intelligence and Lecture Notes in Bioinformatics). Vol 9351. Springer Verlag; 2015:234-241.

38. Zhu J-Y, Park T, Isola P, Efros AA. Unpaired Image-to-Image Translation using Cycle-Consistent Adversarial Networks. Proc IEEE Int Conf Comput Vis. 2017;2017-Octob:2242-2251. Available at: http://arxiv.org/abs/1703.10593. Accessed September 11, 2020.

39. Akcay S, Atapour-Abarghouei A, Breckon TP. GANomaly: Semi-Supervised Anomaly Detection via Adversarial Training. May 2018. Available at: http://arxiv.org/abs/1805.06725. Accessed January 14, 2020.

40. Riley P. Three pitfalls to avoid in machine learning. Nature. 2019;572:27-29.

41. Zeng L-L, Wang D, Fox MD, et al. Neurobiological basis of head motion in brain imaging. Proc Natl Acad Sci. 2014;111:6058-6062.

42. Itri JN, Tappouni RR, McEachern RO, Pesch AJ, Patel SH. Fundamentals of diagnostic error in imaging. Radiographics. 2018;38:1845-1865.

43. Singh H, Meyer AND, Thomas EJ. The frequency of diagnostic errors in outpatient care: Estimations from three large observational studies involving US adult populations. BMJ Qual Saf. 2014;23:727-731.

44. Graber ML. The incidence of diagnostic error in medicine. BMJ Qual Saf. 2013;22:ii21-ii27.

45. Lee CS, Nagy PG, Weaver SJ, Newman-Toker DE. Cognitive and system factors contributing to diagnostic errors in radiology. Am J Roentgenol. 2013;201:611-617.

46. Buolamwini J, Gebru T. Gender Shades: Intersectional Accuracy Disparities in Commercial Gender Classification. In: Friedler SA, Wilson C, eds. Proceedings of Machine Learning Research. Vol 81. Proceedings of Machine Learning Research. New York, NY, USA: PMLR; 2018:77-91. Available at: http://proceedings.mlr.press/v81/buolamwini18a.html. Accessed October 23, 2020.

47. Esteva A, Kuprel B, Novoa RA, et al. Dermatologist-level classification of skin cancer with deep neural networks. Nature. 2017;542:115-118.

48. Han SS, Kim MS, Lim W, Park GH, Park I, Chang SE. Classification of the Clinical Images for Benign and Malignant Cutaneous Tumors Using a Deep Learning Algorithm. J Invest Dermatol. 2018;138:1529-1538.

49. Olah C, Mordvintsev A, Schubert L. Feature Visualization. Distill. 2017;2.

50. Pruessmann KP, Weiger M, Scheidegger MB, Boesiger P. SENSE: Sensitivity encoding for fast MRI. Magn Reson Med. 1999;42:952-962.

51. Donoho DL. Compressed sensing. IEEE Trans Inf Theory. 2006;52:1289-1306.

52. Brown R, Nguyen TD, Spincemaille P, et al. Effect of blood flow on double inversion recovery vessel wall MRI of the peripheral arteries: Quantitation with T2 mapping and comparison with flow-insensitive T2-prepared inversion recovery imaging. Magn Reson Med. 2010;63:736-744.

53. Lindenholz A, van der Kolk AG, Zwanenburg JJM, Hendrikse J. The Use and Pitfalls of Intracranial Vessel Wall Imaging: How We Do It. Radiology. 2018;286:12-28.

54. Viessmann O, Li L, Benjamin P, Jezzard P. T2-Weighted intracranial vessel wall imaging at 7 Tesla using a DANTE-prepared variable flip angle turbo spin echo readout (DANTE-SPACE). Magn Reson Med. 2017;77:655-663.

55. Jia S, Zhang L, Ren L, et al. Joint intracranial and carotid vessel wall imaging in 5 minutes using compressed sensing accelerated DANTE-SPACE. Eur Radiol. 2020;30:119-127.

56. Hu X, Li Y, Zhang L, Zhang X, Liu X, Chung YC. A 32-channel coil system for MR vessel wall imaging of intracranial and extracranial arteries at 3T. Magn Reson Imaging. 2017;36:86-92.

57. Li Y, Chen Q, Wei Z, et al. One-Stop MR Neurovascular Vessel Wall Imaging with a 48-Channel Coil System at 3 T. IEEE Trans Biomed Eng. 2020;67:2317-2327.

58. Duyn JH. The future of ultra-high field MRI and fMRI for study of the human brain. Neuroimage. 2012;62:1241-1248.

59. Pan SJ, Yang Q. A Survey on Transfer Learning. IEEE Trans Knowl Data Eng. 2010;22:1345-1359.

60. Eurostat. Healthcare resource statistics - technical resources and medical technology - Statistics Explained. Available at: https://ec.europa.eu/eurostat/statistics-explained/index.php/Healthcare_resource_statistics_-_technical_resources_and_medical_technology. Accessed October 20, 2020.

61. Raza K, Singh NK. A Tour of Unsupervised Deep Learning for Medical Image Analysis. December 2018. Available at: http://arxiv.org/abs/1812.07715. Accessed October 26, 2020.

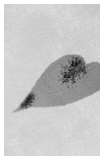

APPENDIX

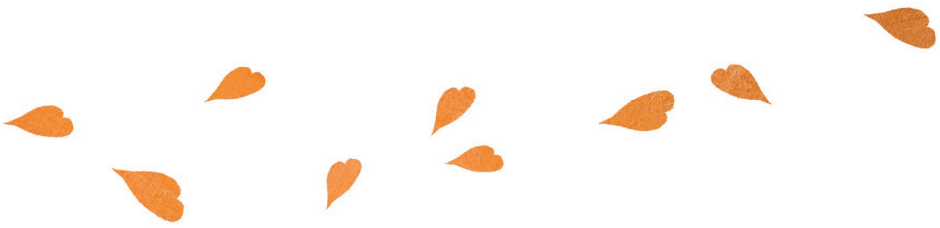

NEDERLANDSE SAMENVATTING

Een herseninfarct is de tweede belangrijkste doodsoorzaak, waar wereldwijd jaarlijks meer dan 5,5 miljoen mensen aan overlijden. Bij een herseninfarct krijgt een deel van de hersenen te weinig zuurstof, doordat een bloedvat in de hersenen is afgesloten door een bloedprop, of doordat een bloedvat in de hersenen is gescheurd. Patiënten die herstellen van een herseninfarct worden vaak geconfronteerd met (langdurige) invaliditeit en hebben daarnaast ook een grote kans op terugkerende herseninfarcten. Ook bij patiënten met cardiovasculaire (hart- en vaatziekten) aandoeningen is de kans op een herseninfarct groot. Om preventieve maatregelen te kunnen nemen, is vroegtijdige detectie van (terugkerende) herseninfarcten dus essentieel in deze patiëntengroepen.

Eén van de belangrijkste oorzaken van een herseninfarct is atherosclerose, ofwel aderverkalking. Bij aderverkalking resulteert een ontstekingsreactie in de vaatwand in een ophoping van materiaal (plaque), bestaande uit onder andere vet, collageen en ontstekingscellen. Door ophoping van materiaal verdikt de vaatwand, waardoor in sommige gevallen een vernauwing van het bloedvat ontstaat. Uiteindelijk kan deze plaque barsten, met een herseninfarct tot gevolg.

Buiten aderverkalking in de grote vaten, kunnen vaatziekten ook de kleine haarvaten treffen. In dit geval kan ziekte aan deze haarvaten resulteren in microinfarcten. Deze microinfarcten geven vaak geen directe klachten, maar kunnen uiteindelijk wel leiden tot cognitieve problemen.

In het laatste decennium is het onderzoeksveld dat zich focust op het afbeelden van de hersenen en de hersenvaten sterk gegroeid. Met behulp van MRI is het mogelijk om de bloedvaten in het hoofd, en schade aan de hersenen als gevolg van ziekte aan de vaten, af te beelden. In dit proefschrift focussen we ons op drie onderdelen die met MRI kunnen worden afgebeeld; de vaatwand, de bloedstroom en het hersenweefsel.

Voor de vroegtijdige detectie van herseninfarcten, dienen veranderingen in de vaatwand te worden geconstateerd. Omdat de hersenvaten relatief klein zijn, kunnen deze in vivo (in de levende mens) niet scherp in beeld worden gebracht middels MRI. Het gedetailleerd afbeelden van anatomische gebieden kost veel tijd. Hiervoor kan ex vivo (buiten de levende mens) onderzoek

uitkomst bieden. In ex vivo onderzoek kunnen langere MRI-sequenties worden gebruikt, die de vaten scherper kunnen afbeelden. In **Hoofdstuk 2** hebben wij met ultrahoog veld MRI onderzocht wat het effect van hypertensie (een verhoogde bloeddruk) is op de vaatwanddikte van de negen grote hersenvaten. Hiervoor hebben we gebruik gemaakt van hersenvaten van overleden patiënten die via de pathologie afdeling beschikbaar zijn gesteld. Hiernaast hebben we met histologische analyse (microscopisch onderzoek aan weefselmateriaal) onderzocht of de samenstelling van de vaatwanden anders is in patiënten met en zonder hypertensie. Ons onderzoek laat zien dat hypertensie, als risicofactor voor vaatwandverdikking en aderverkalking, in de onderzochte patiënten geen significant gevolg heeft voor de vaatwanddikte. Tussen de groepen met en zonder hypertensie is voor alle onderzochte vaten de vaatwanddikte ongeveer gelijk. Ook observeerden we middels histologisch onderzoek dat de ernst en hoeveelheid plaques vergelijkbaar is tussen deze groepen. We observeerden wel een verschil in de ratio collageen/gladde spiercel voor de interne halsslagader. Deze was in de groep patiënten met hypertensie hoger dan die in de groep zonder hypertensie. Een verhoogd ratio collageen/gladde spiercel toont aan dat dit vat verstijfd is, wat uiteindelijk kan lijden tot schade aan de vaatwand en het hersenweefsel.

Zoals eerder genoemd zijn de bloedvaten van de hersenen klein. In **Hoofdstuk 3** hebben we onderzocht of de vaatwanddikte accuraat kan worden gemeten op MRI-beelden die worden gemaakt met klinisch gebruikte MRI-sequenties. Ook hiervoor hebben we gebruik gemaakt van ex vivo hersenvaten. Deze zijn afgebeeld met een klinisch gebruikte MRI-sequentie en een heel hoog-resolute MRI-sequentie. Metingen aan het hoog resolute beeld golden als referentie voor de metingen aan het beeld dat is gemaakt met de klinisch gebruikte MRI-sequentie. Hier concludeerden wij dat alleen voor vaten dikker dan 1.25 keer de voxel grootte (3D pixel) een accurate meting mogelijk is. Voor vaten die dunner zijn is de resolutie van het MRI-beeld te laag om een accurate meting te kunnen uitvoeren. In de praktijk levert dit problemen op voor vaatwanddikte metingen voor alle hersenvaten. De resolutie van klinisch gebruikte scans (voxel grootte: 0.5 tot 0.8 mm in alle drie dimensies) is te laag om accurate metingen uit te voeren aan hersenvaten. De grootste vaten hebben een dikte die tussen de 0.3 en 0.7 mm ligt. Het meten van vroege vaatwandverdikking is in vivo dus niet mogelijk.

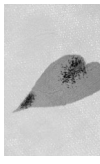

Een maat voor de vaatwanddikte die wel uitkomst biedt, is de signaalintensiteit van de vaatwand. Het is bekend dat de MRI-signaalintensiteit van de vaatwand gecorreleerd is met de vaatwanddikte, ook voor dunnere vaten. Het probleem van deze metingen is echter dat deze metingen niet kwantitatief zijn. Dit wil zeggen dat alleen relatieve verschillen in vaatwanddikte binnen één patiënt kunnen worden gevisualiseerd, er kan echter geen dikte in millimeters aan gekoppeld worden. Wij hebben in **Hoofdstuk 4** gekeken in hoeverre kunstmatige intelligentie hiervoor een oplossing kan bieden. Gebruikmakend van kunstmatige intelligentie, hebben wij een computermodel getraind dat accurate vaatwanddikte metingen kan uitvoeren, ook voor vaten dunner dan 1.25 keer de voxel grootte. In dit hoofdstuk laten we ook de potentie van dit computermodel zien aan de hand van in vivo vaatwand MRI-beelden van aneurysma's, waarvoor we de dikte hebben gemeten middels ons computermodel. Aan de hand van dit computermodel kunnen in de toekomst wel accurate vaatwanddikte metingen worden uitgevoerd, waarbij mogelijk vroegtijdige vaatwandverdikking ten gevolge van vaatziekte kan worden gedetecteerd en gemeten.

In **Hoofdstuk 5** hebben wij ons gefocust op de bloedstroom, waarbij we middels 4D fase contrast MRI (PC-MRI) de bloedstroom van de hersenvaten in kaart hebben gebracht. Het doel van dit hoofdstuk was om de distensibiliteit van de vaten te meten met 4D PC-MRI. Distensibiliteit is het uitzetten van de vaten ten gevolge en ter compensatie van pulsatiele veranderingen in de bloedstroom. Pulsatiele veranderingen zijn veranderingen in bloeddruk en bloedstroomsnelheden over de hartslag. Normaliter worden de pulsatiele veranderingen in de bloedstroom gedempt door het uitzetten van de grote vaten. Hierdoor is de bloedstroom in de kleine haarvaatjes die zich verderop bevinden, stabiel over de hartslag. In ouderen of in mensen met cerebrovasculaire ziekte (aandoeningen van de hersenvaten en de bloedvoorziening van de hersenen) kan er een verminderde distensibiliteit, of wel een verstijving, van de vaten optreden. Hierdoor kunnen de pulsatiele veranderingen in de bloedstroom niet worden gedempt door de grotere vaten, wat resulteert in pulsatiel bloed in de kleine haarvaatjes in de hersenen. Deze zijn niet berekend op sterke pulsdruk en raken hierdoor mogelijk beschadigd. Voor het doel van dit hoofdstuk hebben wij een computerprogramma geschreven waar de gebruiker kan aangeven in welk stroomgebied de distensibiliteit moet worden gemeten. De metingen aan de 4D PC-MRI beelden met ons programma zijn gevalideerd aan metingen aan 2D PC-MRI beelden en laten zien dat meten van de distensibiliteit mogelijk is. Dit kan in

de toekomst inzicht geven in de relatie tussen vaatwandstijfheid als gevolg van vaatziekte en schade aan het hersenweefsel.

Schade aan de haarvaatjes leidt ook tot schade in het hersenweefsel. De uiting van cerebrovasculaire ziekten in schade aan het hersenweefsel is heterogeen. Dit belemmert de implementatie van kunstmatige intelligentie modellen die automatisch deze schade kunnen detecteren. Deze kunstmatige intelligentie modellen hebben veel voorbeelden nodig, om de hele spreiding aan visuele uitingen van hersenschade als gevolg van cerebrovasculaire ziekte te leren herkennen. Deze hoeveelheid voorbeelden zijn vaak niet beschikbaar. In plaats van het trainen van een model om heterogene schade te detecteren, hebben wij in **Hoofdstuk 6** een model getraind, dat gezond hersenweefsel kan detecteren. Als iets niet als gezond weefsel wordt aangemerkt door het model, dan moet dit dus afwijkend/hersenschade zijn. We hebben de prestaties van dit model geëvalueerd op de detectie van chronische herseninfarcten, die heterogeen zijn in vorm, locatie in het brein en in signaalintensiteit. Met ons getraind model kan 67% van de chronische herseninfarcten worden gedetecteerd. Deze herseninfarcten samen representeren 97.5% van het totale herseninfarct volume over alle patiënten. Dit zijn dus veelal hele kleine herseninfarcten. Ons model was ook in staat om 26 extra herseninfarcten te detecteren in 225 patiënten. Deze waren door de radioloog over het hoofd gezien tijdens het verslaan van de beelden. Hiernaast detecteerde ons model ook witte stof laesies, calcificaties en beeld artefacten (als gevolg van beweging van de patiënt in de MRI-scanner).

In dit proefschrift hebben we ons gefocust op technieken waarmee een bijdrage kan worden geleverd aan de vroegtijdige detectie van herseninfarcten. Hiervoor hebben we onderzoek gedaan naar veranderingen in de vaatwand, de bloedstroom en het hersenweefsel als gevolg van cerebrovasculaire ziekten. De resultaten geven duidelijk weer dat kwantificatie van veranderingen in de cerebrale bloedsomloop, die uiteindelijk kunnen leiden tot een herseninfarct, mogelijk zijn door gebruik te maken van MRI en kunstmatige intelligentie modellen. In de toekomst van dit onderzoeksveld liggen de uitdagingen om vaatwandscans verder te ontwikkelen en om kunstmatige intelligentie modellen te implementeren en te valideren voor gebruik in de kliniek.

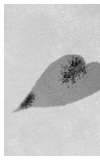

DANKWOORD

Nu het onderzoek is afgerond, resteert mij enkel het bedanken van heel veel mensen zonder wiens bijdrage dit proefschrift nooit tot stand was gekomen. In het bijzonder wil ik alle vrijwilligers en patiënten bedanken die voor mijn onderzoek in de scanner zijn geweest.

Prof. dr. Jeroen Hendrikse, beste Jeroen, ik ben ontzettend blij dat ik onder jouw supervisie mijn promotietraject mocht doorlopen. Je was altijd op de hoogte van alle lopende projecten en kwam vaak met nieuwe ideeën voor onderzoek en inzichten aanzetten, uit een ogenschijnlijk onuitputtelijke bron. Daarnaast kwam je, wanneer de tijd het toeliet, buurten op de kamer om te vragen hoe het ging. Ik wil je bedanken voor je vertrouwen in mij en voor de vrijheid die je me hebt gegeven om het onderzoek naar eigen inzicht te verrichten. Ook wil ik je bedanken voor alle middelen die je zo vrijelijk beschikbaar stelde om mij het beste uit mezelf en uit het onderzoek te laten halen.

Prof. dr. Peter Luijten, beste Peter, bedankt voor de mogelijkheden die je voor onderzoekers hebt gecreëerd binnen de 7T groep. Een verscheidenheid aan expertise op technisch en medisch vlak is vertegenwoordigd in deze groep en samenwerking tussen verschillende subgroepen wordt gestimuleerd. Ook de goede sfeer binnen de groep is een belangrijke eigenschap die het makkelijk maakt voor (nieuwe) onderzoekers om vrij laagdrempelig advies in te winnen bij collega's. Heel erg bedankt voor het creëren van deze omgeving.

Dr. ir. Hugo Kuijf, beste Hugo, ik weet nog goed dat jij op het moment dat ik gesolliciteerd had nog niet wist dat je mijn begeleider zou worden. Ik was immers zonder aankondiging in jouw kamer afgezet door Jeroen. Ook had jij hiervoor nog geen PhD'ers van begin tot eind begeleid. Dit mocht allemaal geen obstakel zijn, want je hebt mij als dagelijks begeleider altijd met veel kunde en passie bijgestaan. Het onderzoek ging, zoals bij velen, met pieken en dalen. Als ik in een dal zat, zag jij altijd wel een uitweg. Je positieve karakter, bevlogenheid en kennis van medische beeldverwerking was ontzettend aanstekelijk en stimulerend. Ook zal ik het congres in San Diego, met bijbehorende roadtrip door Californië, niet snel vergeten. Heel erg bedankt voor je betrokkenheid en begeleiding tijdens mijn promotieonderzoek.

Dr. ir. Jaco Zwanenburg, beste Jaco, ik bewonder je kennis van MRI, je nauwkeurige manier van werken en je kritische blik die je op het werk van anderen, maar vooral op je eigen werk, werpt. Ik heb hier heel veel van opgestoken en daardoor het beste uit mijn werk kunnen halen. Als dagelijks begeleider was jij altijd beschikbaar voor een praatje. Je wist me perfect te motiveren en op te beuren als het onderzoek weer eens tegenzat. Je wist altijd goed door te vragen om samen tot de kern van het probleem te komen en deze doelgericht te kunnen oplossen. Ik wil je onwijs bedanken voor je betrokkenheid, enthousiasme en de rust die je me gaf tijdens mijn promotieonderzoek.

Ik wil graag alle leden van de leescommissie, prof. dr. G.J. Biessels, prof. dr. M.H. Emmelot-Vonk, prof. dr. J.P.W. Pluim, prof. dr. W.J. Niessen en prof. dr. P.A. de Jong, bedanken voor de tijd en moeite die zij hebben gestoken in het beoordelen van mijn proefschrift.

Beste Dorien, heel erg bedankt voor de ontzettend soepele en gestructureerde samenwerking in de afgelopen vier jaar. Samen hebben we veel preparaten kunnen afbeelden en analyseren, met als resultaat een mooi gepubliceerd artikel. Ook wil ik alle andere collega's (Claire, Ingeborg, Marloes en prof. dr. Mat Daemen) uit het Amsterdam UMC bedanken voor hun bijdrage aan het onderzoek en voor het meedenken en kritisch lezen van het artikel beschreven in hoofdstuk 2.

Dr. Wim van Hecke, mijn connectie met de pathologie van het UMC Utrecht, ontzettend bedankt voor de hulp bij het uitzoeken van de preparaten. Je was altijd bereid om af te spreken en ik kon laagdrempelig terecht bij jou als ik met vragen zat over de preparaten. Dit heb ik erg gewaardeerd.

Jacob-Jan, Evita, Lieke, Anneloes, Tine, Zahra, Sarah, Edwin, Seb, Jeanine, Carlo, Ayhan, and Kyung-Min: (frequent) members of the daily coffee train. The daily coffee moment was always something to look forward to. A quick break to talk about non-work-related topics worked perfectly to clear my head from programming or paper writing issues. Thanks for all of these fun intermezzos!

Former and current roommates Lennart, Deji, Quincy, Edwin, Lieke, and Ayhan: our room must have been the most musical one in the entire hallway. Besides listening and humming songs together, we also frequently spontaneously sang—or at least made a halfhearted attempt to sing—acapella,

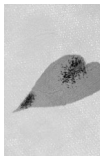

which was not always to everyone's delight. Nonetheless, this distraction was excellent to cope with PhD stress. And even though I could not convince any of you to use MeVisLab, I could always depend on everyone when facing programming difficulties or if I needed to vent about the speed of the peer review process.

I also want to thank all other members and students of the 7T group, the coillab, and the ISI group for their collaboration and the great atmosphere that they helped create in the last four years. Thanks for all the fun drinks, congresses, and sailing and ice-skating excursions.

Uiteraard kan de wetenschap nooit worden uitgevoerd zonder de orde en structuur die wordt aangebracht door het secretariaat. Marja en Maria, bedankt voor het regelen en plannen van alle afspraken tijdens mijn PhD. Sylvia, heel erg bedankt voor alles wat je betekent voor de 7T groep, die zonder jouw bijdrage nooit zou kunnen zijn wat het nu is. Ook bedankt voor alle kletspraatjes die we 's ochtends vroeg tussendoor hadden.

Ook had dit proefschrift niet tot stand kunnen komen zonder de bijdrage van alle andere coauteurs. Heel erg bedankt.

Medewerkers van het trial bureau: Ramona, Diana en Shanta, bedankt voor het inplannen van vele MRI-onderzoeken en het bijhouden van alle lopende patiëntenstudies.

Ook had ik nooit met de stress van de PhD kunnen omgaan zonder de afleiding en adviezen van de Bachelor boys (Tim, Mitchel, Vincent en Benoît). Jullie zijn altijd in voor een praatje of een potje gamen. Het is mooi dat we (minimaal) sinds de bachelor technische natuurkunde zo'n hechte en gezellige vriendengroep zijn.

Lieve John, Henriëtte en Peter, zonder jullie had ik nooit zo ver kunnen komen. De stabiele basis die jullie hebben gecreëerd tijdens mijn jeugd heeft het voor mij mogelijk gemaakt dit academische pad te bewandelen. Jullie hebben altijd in mijn kunnen geloofd en mij onvoorwaardelijk gesteund. Ik kan jullie hier niet genoeg voor bedanken.

Lieve Daphne, ik had dit nooit zonder jouw steun en liefde kunnen doen. Ondanks dat je het zelf soms ook zwaar had op je werk, was je er de afgelopen vier jaar altijd voor me. Als het even minder ging kon jij altijd de zaken

relativeren en me een luisterend oor aanbieden. Ik kijk onwijs uit naar een toekomst met jou.

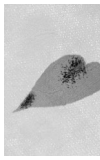

LIST OF PUBLICATIONS

PUBLICATIONS IN INTERNATIONAL JOURNALS

van Hespen KM, Zwanenburg JJM, Harteveld AA, Luijten PR, Hendrikse J, Kuijf HJ. Intracranial Vessel Wall Magnetic Resonance Imaging Does Not Allow for Accurate and Precise Wall Thickness Measurements. Stroke. 2019;50.

van Hespen KM, Zwanenburg JJM, Hendrikse J, Kuijf HJ. Subvoxel vessel wall thickness measurements of the intracranial arteries using a convolutional neural network. Med Image Anal. 2021;67:101818.

van Hespen KM, Mackaaij C, Waas ISE, de Bree MP, Zwanenburg JJM, Kuijf HJ, Daemen MJAP, Hendrikse J, Hermkens DMA. Arterial Remodeling of the Intracranial Arteries in Patients With Hypertension and Controls. Hypertension. 2021;77:135-146.

van Hespen KM, Zwanenburg JJM, Dankbaar JW, Geerlings MI, Hendrikse J, Kuijf HJ. An Anomaly Detection Approach to Identify Chronic Brain Infarcts on MRI. Sci Rep. *In press*.

van Hespen KM, Kuijf HJ, Hendrikse J, Luijten PR, Zwanenburg JJM. Blood flow velocity pulsatility and arterial diameter pulsatility measurements of the intracranial arteries. *Submitted for publication*.

CONFERENCE PROCEEDINGS

van Hespen KM, Zwanenburg JJM, Hendrikse J, Kuijf HJ. Subvoxel vessel wall thickness measurements from vessel wall MR images. In: Angelini ED, Landman BA, eds. Medical Imaging 2019: Image Processing. Vol 10949-69. SPIE; 2019:69.

van Hespen KM, Zwanenburg JJM, Harteveld AA, Luijten PR, Hendrikse J, Kuijf HJ. Investigating the estimated intracranial wall thickness on MRI vessel wall images: what voxel size do we need?

- In: Proceedings of the Joint Annual Meeting of the ISMRM-ESMRM 2018. 2018:Program no. 3461.
- In: Proceedings of the ISMRM Benelux Chapter 2018. 2018:P-022

van Hespen KM, Kuijf HJ, Luijten PR, Hendrikse J, Zwanenburg JJM. Intracranial vessel wall thickness measurements: A post-mortem comparison between hypertensive patients and controls.

- In: Proceedings of the Joint Annual Meeting of the ISMRM-ESMRM 2019. 2019:Program no. 740. **Magna Cum Laude ISMRM merit award**
- In: Proceedings of the ISMRM Benelux Chapter 2019. 2019:P-002. **Nomination Best Poster Award**

INVITED TALKS

van Hespen KM, Zwanenburg JJM, Harteveld AA, Luijten PR, Hendrikse J, Kuijf HJ. Estimated intracranial vessel wall thickness with MRI is strongly dependent on voxel size. Philips Healthcare international 7T user group meeting. Jean and Alexander Heard Library at Vanderbilt University, Nashville, USA, 2017.

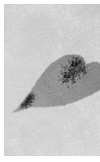

CURRICULUM VITAE

Kees van Hespen was born on February 2nd, 1992 in Spijkenisse, the Netherlands. After finishing secondary education in 2010 at De Ring van Putten in Spijkenisse, he obtained a bachelor's degree in Applied Physics in 2014 at the Technical University Delft. A minor in Medicine piqued his interest in the application of technology in medicine, which led him to continue with a master in Biomedical Engineering (Medical Physics track) at the Technical University Delft. During his master's studies he did an internship at Quantib, Rotterdam, where he worked on liver fat concentration quantification from Dixon MR images. During his master thesis, he focused on the quantification of carotid atherosclerotic plaque contents using quantitative MRI. He conducted this work at the Erasmus Medical Center in the Biomedical Imaging Group Rotterdam. Kees obtained his master's degree in 2016.

After his master's degree, he started as a PhD candidate in the department of Radiology at the University Medical Center Utrecht in 2017. Here, his research focused on the detection and quantification of cerebrovascular disease under the supervision of Jeroen Hendrikse, Peter Luijten, Jaco Zwanenburg, and Hugo Kuijf. The results of this research are presented in this thesis.

Kees is currently working as a scientific software engineer at Clinical Graphics.